UNIVERSITY OF COPENHAGEN
FACULTY OF SCIENCE

MSc. in Computational Physics

Dispersion engineering of atom-nanophotonic crystal waveguide interfaces

Numerical study of quantum emitters in photonic crystal structures for strong atom-light and atom-atom interactions

Beñat Martinez de Aguirre Jokisch

Supervised by Asst. Prof. Jean-Baptiste Béguin and Prof. Eugene S. Polzik

May 2022

Beñat Martinez de Aguirre Jokisch
Dispersion engineering of atom-nanophotonic crystal waveguide interfaces
MSc. in Computational Physics, May 2022
Supervisors: Asst. Prof. Jean-Baptiste Béguin and Prof. Eugene S. Polzik

University of Copenhagen
Niels Bohr Institute
Masters Degree in Computational Physics
Blegdamsvej 17
2100 Copenhagen

Defense date: 20th of June 2022

Acknowledgements

I would like to express my most sincere gratitude to all the people that made it possible to complete this thesis and have an incredible time in the process. En particular, doy gracias a Aita, Mama y Nahia por ayudarme a lo largo de mi aventura en Dinamarca. Sabéis que sin vuestra ayuda y confianza esto no hubiera sido posible, y siempre os estaré agradecido porque me queréis y creéis en mí.

Next, I have to thank my supervisors for teaching me so much in this very interdisciplinary field. Thank you J.B. for helping me bring forward a theoretical/numerical project in an experimental group, where experiments are the angular stone of scientific discovery. Although this is true in the end, I have to thank your ambition of finding exciting underlying physics through simulations. I must also thank Eugene for his exceptional ability to narrow down very complicated physics to very simple principles, which helped me understand many concepts in Quantum Optics. Even though I only had two official supervisors I must also thank Jörg, who acted as an effective third supervisor. Thank you very much for helping me out when I needed to discuss physics with someone and your relaxing guitar solos at coffee time.

I would also like to thank my colleagues at LAQS, who introduced me to the experimental intricacies of the fabrication and atom-trapping. Thank you Jacob for explaining the experimental setup, over and over again. Thank you Anders for helping navigate through the main references in the field and helping me out understand the basics of the fabrication process. And thank you Jonas for your discussions on simulation and for making me laugh from time to time. Thank you to my colleagues at QUANTOP too, especially to my office mates and good friends Isaac and Alan, with whom I share very

happy moments. Special thanks to Isaac who provided some figures to help me illustrate atomic physics concepts. Thank you also to Arnau and the rest of colleagues at the NBI.

While I was doing this thesis I was also working on the side, and I would not have been able to stay in Denmark if it was not for the economical stability that my job and the SU provided. That is why I send a special thank you to Lorenzo Baldari, for offering me my first job in Denmark and to Mark Nicholas Jones for opening me the door to Molecular Quantum Solutions and the world of chemical property prediction using quantum computing.

Needless to say, I would not be in Denmark if it was not for the very insightful conversations with Audric Artaud: merci, c'etait une idée magnifique. In this journey I have met many friends I would like to thank. Thank you for the moments we shared under the sun in the park, in the cold and dark winter days during the lockdown and on the many trips through Denmark and many other countries. I am sure there will be many more friends and adventures to come in the next years.

Finally, I would like to thank my closest friends that were there to support me and cheer me up along the way. En especial, vull donar-li les gràcies a l'Alba, a qui vaig conèixer a Dinamarca. Des del primer moment que la vaig conèixer vaig saber que seriem molt bons amics. Ara m'acompanyarà en les meves properes aventures i no podria estar més ben acompanyat. Moltes gràcies Alba. Eskerrik asko Euskal Herriko lagun guztiei, batez ere Gasteizko kuadrillari eta hurbileko lagun minei. Besarkada berezi bat Javiri azken urte zail honengatik, badakizu urrun egon arren beti alboan nauzula, hurbil somatu ez arren: "*...Every day I come by to pick you up. And we go out we have a few drinks and a few laughs, and it's great. But you know what the best part of my day is? It's for about ten seconds from when I pull up to the curb to when I get to your door. Because I think maybe I'll get up there and I'll knock on the door and you won't be there.*"

Abstract

The combination of atoms and nanophotonic devices presents novel paradigm in the field of quantum optics. Nanophotonic structures can be used to engineer the interaction medium, allowing to mediate strong atom-light interactions, a key component in the quest for quantum computation with neutral atoms. In this thesis we study a nanophotonic platform, known as photonic crystal waveguide, to harness strong atom-atom interactions mediated by photons. This system presents a novel framework with direct applications to quantum simulation, which will be used to solve conventionally hard computational problems with applications in the life sciences. We focus on providing a simulation toolbox to calculate the main Figures of Merit in atom-photon and atom-atom interactions for arbitrary photonic crystal structures, such as the coupling coefficients of quantum many-body Hamiltonians. With our method we also demonstrate a general numerical approach to benchmark the performance of different device designs, taking into account fabrication imperfections and tolerances. Lastly, we use this toolbox to suggest possible improved design parameters relative to state-of-the-art devices, which could lead to enhanced performance in our quantum simulation platform.

Contributions

Simonsen, A., Hansen, J.T., Martinez de Aguirre, B., Mathiassen, J.B., Müller, J.H., Polzik, E.S., & Béguin, J.-B. *Quantum Simulation Using Cold Atoms and Photonics.* Quantum Computing Applications in Chemical and Biochemical Engineering Workshop (2022).

All the work that was done alongside the MSc. thesis was a collective effort of the members of the LAQS experiment at QUANTOP. My responsibilities in the group during my project were focused on numerical simulations and device design. I also worked on accounting for fabrication defects, in collaboration with A. Simonsen and J.B. Mathiassen, who where in charge of the fabrication and characterization of the devices. J.H. Hansen was responsible for trapping the atoms close to the photonic crystal devices and setting up the optical systems in the laboratory, in collaboration with J.-B. Béguin. All these efforts were jointly supervised by J.-B. Béguin, J.H. Müller and E.S. Polzik.

Contents

Constants and Abbreviations

Constants

In this thesis we have followed the standard S.I. system, and have made use of several physical constants:

- $\varepsilon_0 = 8.8541878128(13) \cdot 10^{-12}$ F·m^{-1}: vacuum permittivity.
- $\mu_0 = 1.25663706212(19) \cdot 10^{-6}$ H/m: vacuum permeability.
- $c = 299792458$ m/s: velocity of light in vacuum
- $m_e = 9.1093837015(28) \cdot 10^{-31}$ kg: mass of the electron.
- $e = 1.602176634 \cdot 10^{-12}$ C: elementary charge of a proton.
- $\hbar = 1.054571817 \cdot 10^{-34}$ J·s: reduced Planck constant.
- $a_0 = 5.29177210903(80) \cdot 10^{-11}$ m: Bohr radius.
- $\mu_B = 9.2740100783(28) \cdot 10^{-22}$ J·T^{-1}: Bohr magneton

Abbreviations

The reader will also encounter several abbreviations that are defined the first time they are used but not thereafter. For reference we summarize them in the following list:

- QED: Quantum Electrodynamics.
- FOM(s): Figure(s) of Merit.

- LAQS: Light Atom Quantum Simulator.
- SEM: Scanning Electron Microscope.
- TMM: Transfer Matrix Method.
- TE: Transverse Electric.
- TM: Transverse Magnetic.
- NF: Near field.
- IF: Intermediate field.
- FF: Far field.
- DC: Direct current.
- PF: Purcell Factor.
- FDTD: Finite-Difference Time Domain.
- MPB: MIT Photonic Bands.
- RWA: Rotating Wave Approximation.
- FORT: Far-Off Resonance dipole-force Trap.
- H.C.: Hermitian Conjugate.
- FFT: Fast Fourier Transform.
- LDOS: Local Density of Optical States.

1 Introduction

" Mais à l'instant même où la gorgée mêlée des miettes du gâteau toucha mon palais, je tressaillis, attentif à ce qui se passait d'extraordinaire en moi. Un plaisir délicieux m'avait envahi, isolé, sans la notion de sa cause. Il m'avait aussitôt rendu les vicissitudes de la vie indifférentes, ses désastres inoffensifs, sa brièveté illusoire, de la même façon qu'opère l'amour, en me remplissant d'une essence précieuse: ou plutôt cette essence n'était pas en moi, elle était moi."

— Marcel Proust, *Du côté de chez Swann.*

In this MSc. thesis we will numerically study and simulate strong atom-atom interactions mediated by light propagation in novel nanodielectric structures. Coupling neutral atoms to nanophotonic crystal waveguides presents a new frontier in quantum optics with applications to quantum simulation and quantum many-body problems.

1.1 Atom-photon interaction frameworks

Among the most essential physical processes in quantum optics we have the interactions between light and matter. Light is famous for being a good carrier of information due to low losses and neutral atoms have been proven to be an exquisite form of information storage, in the form of qubits.

Achieving a strong coupling between photons and atoms is therefore central in order to combine the transmission and storage of information into a unified framework, which is key to several applications in quantum metrology and quantum information processing [1] [2].

Neutral atoms do not have a net electrical charge so, in the lowest order[1], they do not interact with electromagnetic fields. Thus, in general, atom-photon interactions are weak and are found in higher moments of the charge distribution in atoms. It is possible to describe the strength of this interaction through the interaction Hamiltonian $\hat{H}_{\text{int}} = \hat{\mathbf{E}} \cdot \hat{\mathbf{d}}$, where $\hat{\mathbf{E}}$ is the electric field of light and $\hat{\mathbf{d}}$ is the dipole moment of the atoms [3].

As illustrated in Figure 1.1 there are several ways to achieve strong atom-light coupling:

- **Increasing the electric field of light**: One can increase the electric field of the interaction by **tight focusing** [4], as shown in Figure 1.1a. This involves optimizing the way we focus light onto the atom; this is, to increase the overlap of the light field and the atom so that the strength of the field increases. Unfortunately, the smallest area the light can be focused down in free-space is set by the diffraction limit.

- **Multiplying the interaction**: It is possible to enhance the interaction of strength by summing the contributions of many individual interactions. For instance, in Figure 1.1b we have **cavity QED** [5][6] where both the atom and light field meet in a cavity formed by two mirrors, so that the round-trips that the photon makes across the atom due to the reflection off the mirrors result in interaction strength proportional to the number of round-trips.

  Another possibility shown in Figure 1.1c is to work with an **ensemble of atoms** [7]. When the light propagation phase is negligible compared to the atom ensemble dimension, the light decayed from atoms in the ensemble will sum up coherently, leading to **Dicke superradiance** [8], which leads to a collective interaction proportional to atom number N_a.

- **Increasing the dipole moment of the atom(s)**: It is possible to magnify the dipole moment of the atom by exciting it to the **Rydberg state** [9] [10] [11] with high principle quantum number n. Since the Rydberg state dipole moment scales with n^2 it is possible to achieve a very high dipole moment.

[1] Since the monopole contribution will be equal to zero.

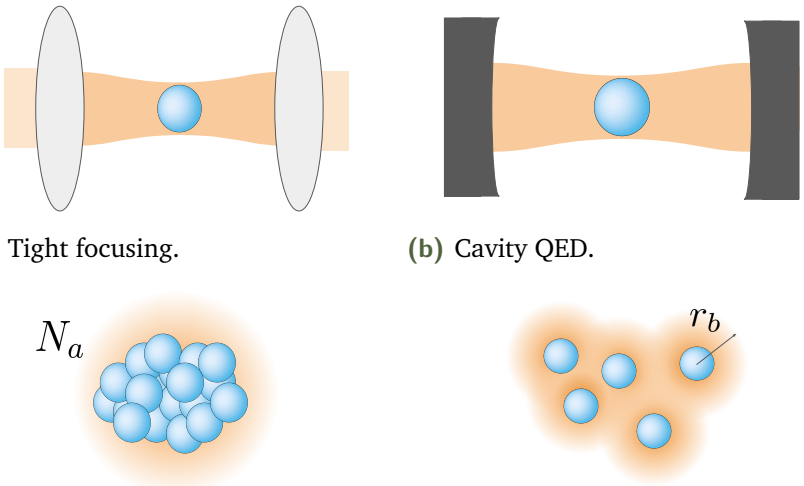

(a) Tight focusing. **(b)** Cavity QED.

(c) Atomic ensembles. **(d)** Rydberg ensemble.

Figure 1.1.: Set of conventional approaches in quantum optics to achieve strong atom-photon (atom in blue and photon in orange) interactions inspired by [1]. **(a)** Focusing of an optical beam onto a tightly trapped atom, **(b)** Strong interaction is achieved by a large number of photon round-trips **(c)** A large atom number N_a enhances the probability of interaction with a photon, and **(d)** atomic ensemble of Rydberg atoms, with Rydberg radius r_b.

All the previous approaches in Figure 1.1 have been realized in free-space settings, but making use of nanophotonic devices it is possible to combine all their strong suits onto a holistic platform. Nanophotonics allows to manipulate light in sub-wavelength regime and to engineer the photonic properties of the environment. This novel framework opens up many possibilities, and as we will describe in the next chapters, one may be able to enhance or suppress the atoms emission of light into the structures, trap atoms using the fields propagating through this devices [12], or even make atoms interact between themselves in a controlled way [13] [12] which can be used to experimentally carry out **quantum simulations**.

As we will see in this work, nanophotonic devices also show great promise as a platform for scaling up light atom-interactions. In the future one could imagine them as one of the building blocks of the **Quantum Internet** [2] where different quantum systems would unite in larger networks, where information would be transmitted through optical channels and quantum states could be teleported [14] back and forth between channels. These networks could then be remotely accessed by users which would have a profound scientific and

technological impact as we know it, making **quantum cryptography** [15] and **communication** [15] [16] accessible for users globally.

1.2 Experimental setup at QUANTOP

For my MSc. Thesis project I joined the experimental group at **QUANTOP**, led by Prof. Eugene S. Polzik and Prof. Jörg H. Müller, to collaborate in the **Light Atom Quantum Simulator** (LAQS) experiment, led by Asst. Prof. Jean-Baptiste Béguin. QUANTOP is an experimental group famous for manipulating ensembles of neutral atoms to achieve strong atom-light coupling and to harness quantum optical phenomena.

It took 3 decades to improve the coupling of a single atom and light by 9 orders of magnitude, in cavity QED [2]. Until 2013 it was not clear how this could be pushed even further, until Thompson, Lukin et al. achieved an extra 2 orders of magnitude in the atom-photon interaction strength, by coupling a single trapped atom to a nanoscale optical cavity [17]. In the past, researchers at QUANTOP took a step towards this direction by trapping [18] [19] ensembles of Caesium (Cs) atoms[2] within the evanescent light field of on optical fiber [20] thinner than a light wavelength, to achieve strong interactions between the light guided by the fiber and the atoms. This system can be used to develop quantum measurement strategies and to create quantum states [21] [22] for quantum information and metrology purposes [23] [24].

Following the pioneering efforts by Prof. Jeff Kimble et al. (i.e. Jean-Baptiste Béguin) at Caltech to combine cold atom physics and nanophotonics [25] [26] [27] [28] [13] [12] QUANTOP is developing a new research direction with the goal of trapping atoms near two-dimensional photonic crystal waveguides. This research is highly multidisciplinary, spanning from condensed matter physics, nanofabrication, cold atom physics, quantum optics, computational and numerical physics, etc.

In the near future this platform will be used to build a **quantum simulator using neutral atoms and photonic crystals**. As shown in Figure 1.2, atoms will be brought and trapped close to the photonic crystal structures using

[2] More on Cs atoms and why they are used at QUANTOP in Appendix A.

special lasers known as optical tweezers [29] so that the atoms can interact with each other through the guided field of the structure. This simulator will be then used to address hard computational challenges in the life sciences as a part of the Quantum For Life (QFL) initiative [30].

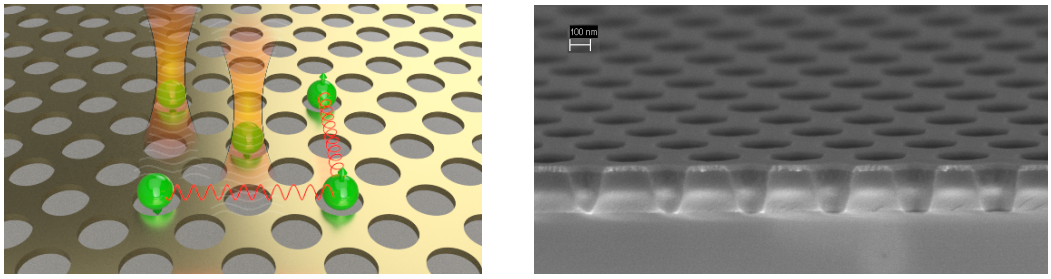

(a) Atom-atom interactions in the chip. **(b)** SEM image of photonic crystal.

Figure 1.2.: Experimental platform in the LAQS group. **(a)** Atoms (green balls) are inserted in the holes of a perforated membrane using laser beams. The atoms interact with each other by exchanging photons (red lines) that travel along the structure. **(b)** Scanning-Electron-Microscope (SEM) image of a nanophotonic array made by etching holes into silicon nitride. The membrane are used as a mean to enhance the atom-light coupling. Figures courtesy of Anders Simonsen and Jonas Mathiassen [30].

In my MSc. in Computational Physics I mainly learnt about numerical methods and simulation. Therefore, I decided to join LAQS to **help understand and forecast physical phenomena by numerically solving Maxwell's equations**, in an effort to **improve on the current design of their photonic crystal chips**. With my contributions my colleagues should be able to extract the main Figures of Merit (FOMs) of their physical system to understand the interactions between light and atoms in arbitrary photonic crystal systems.

Since this will be the first written material in the LAQS group, I wanted my colleagues and those who will follow, to have a comprehensive theoretical review of the main underlying physics of the platform. Therefore, I worked hard on writing an extensive MSc. thesis that builds up from simple principles up to the main results that may be obtained in the experiment. In addition, I also created a comprehensive compilation of the code in this thesis' `Github` [31] so that in the future they can reproduce and expand my work.

Thesis outline

With all this in mind, throughout this thesis we will try to figure out how to obtain strong atom-atom interactions mediated by photons, so that we can enhance the current nanophotonic design of photonic chips that are fabricated in the cleanroom.

We will do this in different chapters:

- In Chapter 2 we will explain what photonic crystals are and how they can mold the flow of light [32] to allow for strong atom-photon and atom-atom interactions.

- In Chapter 3 we will understand how atoms emit close to photonic crystals giving rise to novel physical phenomena, such as atom-atom interactions mediated by light.

- In Chapter 4 we will use numerical techniques to understand the dispersion propertiers of photonic crystals, the emission of atoms close to these structures and how to improve on the current design of nanophotonic devices.

- Finally, in Chapter 5 we will summarize the main learnings and results of the previous chapters.

2 Dispersion properties of photonic crystals

" A la realidad le gustan las simetrías y los leves anacronismos."

— Jose Luis Borges*, Ficciones.*

Photonic crystals are a promising environment with many potential applications that can be engineered to control light propagation to achieve strong light-atom coupling while also offering a physical platform to mediate atom-atom interactions with photons. Accordingly, we will illustrate and understand several of the useful dispersion properties of photonic crystals:

- Photonic crystals can be used to obtain **slow-light**, which results in a enhancement of the atom-photon coupling.
- Photonic crystals can have a **band-gap**, where for certain frequencies light cannot propagate through the structures. Although the structures will become almost perfect reflectors, the field in the structure will be non-zero. It will then be possible to use this field to make atoms interact with each other.
- Finite photonic crystals will have **cavity resonances** and as we will see in Chapter 3 they can be used to increase the atom-light coupling.
- Photonic crystal slabs will have **unwanted losses** due to the finite thickness of the slab, that we will later try to minimize in Chapter 4.

In this chapter we mainly follow references [32] and [33] to understand these special dielectric structures from two complementary perspectives. The latter reference introduces the Transfer Matrix Method, a toy model to understand the main dispersion properties of the photonic crystals, which will be used in Chapter 3 to understand how atoms couple with them.

2.1 Electromagnetism in dielectric media

The propagation of light is described by the four macroscopic **Maxwell equations**[1] [32] [34] :

$$\nabla \cdot \mathbf{B} = 0\,, \quad \nabla \times \mathbf{E} + \frac{\partial \mathbf{B}}{\partial t} = 0\,, \tag{2.1}$$

$$\nabla \cdot \mathbf{D} = \rho\,, \quad \nabla \times \mathbf{H} - \frac{\partial \mathbf{D}}{\partial t} = \mathbf{J}\,, \tag{2.2}$$

where $\mathbf{E}$ and $\mathbf{H}$ are the macroscopic electric and magnetic fields, $\mathbf{D}$ and $\mathbf{B}$ are the electric displacement and magnetic induction, and ρ and $\mathbf{J}$ are the free-charge and current densities.

In our analysis we will suppose that we have regions of homogeneous dielectric material which is not time dependent and there are no currents or charges. Furthermore, we assume that we are in the **linear regime** and that our materials are **macroscopic**, **isotropic** and **transparent**. This means that our materials can be characterized by a real and positive valued dielectric function $\varepsilon(\mathbf{r}, \omega)$ that obeys: $\mathbf{D} = \varepsilon_0 \varepsilon(\mathbf{r})\mathbf{E}(\mathbf{r})$. Similarly, we will also have $\mathbf{B} = \mu_0 \mu(\mathbf{r})\mathbf{H}(\mathbf{r})$. This allows us to rewrite Equation 2.1 and Equation 2.2:

$$\nabla \cdot \mathbf{H}(\mathbf{r}, t) = 0 \qquad \nabla \times \mathbf{E}(\mathbf{r}, t) + \mu_0 \frac{\partial \mathbf{H}(\mathbf{r}, t)}{\partial t} = 0 \tag{2.3}$$

$$\nabla \cdot [\varepsilon(\mathbf{r})\mathbf{E}(\mathbf{r}, t)] = 0 \qquad \nabla \times \mathbf{H}(\mathbf{r}, t) - \varepsilon_0 \varepsilon(\mathbf{r}) \frac{\partial \mathbf{E}(\mathbf{r}, t)}{\partial t} = 0\,. \tag{2.4}$$

Since the Maxwell equations in Equation 2.3 and Equation 2.4 are linear one can separate the time and spatial dependence by means of a **harmonic expansion**, where: $\mathbf{H}(\mathbf{r}, t) = \mathbf{H}(\mathbf{r})e^{-i\omega t}$ and $\mathbf{E}(\mathbf{r}, t) = \mathbf{E}(\mathbf{r})e^{-i\omega t}$. Inserting these fields into Equation 2.3 and Equation 2.4 we obtain:

$$\nabla \cdot \mathbf{H}(\mathbf{r}) = 0, \quad \nabla \cdot [\varepsilon(\mathbf{r})\mathbf{E}(\mathbf{r})] = 0\,. \tag{2.5}$$

[1] in SI units.

This means that there are no point sources in the medium and that the field configurations are based on **transverse electromagnetic waves**. Taking Equation 2.3 and Equation 2.4:

$$\begin{aligned} \nabla \times \mathbf{E}(\mathbf{r}) - i\omega\mu_0 \mathbf{H}(\mathbf{r}) &= 0 \\ \nabla \times \mathbf{H}(\mathbf{r}) + i\omega\varepsilon_0\varepsilon(\mathbf{r})\mathbf{E}(\mathbf{r}) &= 0\,, \end{aligned} \tag{2.6}$$

and combining them yields the **master equation** [32]:

$$\nabla \times \left(\frac{1}{\varepsilon(\mathbf{r})} \nabla \times \mathbf{H}(\mathbf{r}) \right) = \left(\frac{\omega}{c} \right)^2 \mathbf{H}(\mathbf{r}) \tag{2.7}$$

where $c = 1/\varepsilon_0\mu_0$ is the speed of light. Interestingly, the master equation is **scale invariant**[2], which means that the solution at one length scale can be applied to all length scales. The master equation can be understood as an **eigenvalue problem** for $\mathbf{H}(\mathbf{r})$ for a given structure $\varepsilon(\mathbf{r})$. To calculate the electric field $\mathbf{E}(\mathbf{r})$ one may then use Equation 2.6. The eigenvalue problem can be rewritten by means of an operator $\hat{\Theta}$:

$$\hat{\Theta}\mathbf{H}(\mathbf{r}) = \left(\frac{\omega}{c} \right)^2 \mathbf{H}(\mathbf{r})\,, \tag{2.8}$$

where the differential operator is:

$$\hat{\Theta}\mathbf{H}(\mathbf{r}) = \nabla \times \left(\frac{1}{\varepsilon(\mathbf{r})} \nabla \times \mathbf{H}(\mathbf{r}) \right)\,, \tag{2.9}$$

the eigenvalues are ω^2/c^2 and the eigenmodes $\mathbf{H}(\mathbf{r})$. Since the operator in this eigenvalue problem is hermitian and we consider harmonic modes, the eigenvalues are **real** and the eigenmodes are **orthogonal** if there is no degeneracy[3]. It is equally possible to define the eigenvalue problem in terms of the electric field instead of the magnetic field as [32]:

$$\nabla \times \nabla \times \mathbf{E}(\mathbf{r}) = \left(\frac{\omega}{c} \right)^2 \varepsilon(\mathbf{r})\mathbf{E}(\mathbf{r})\,, \tag{2.10}$$

which is a generalized eigenproblem, since there are operators at both sides of the equation. The eigenproblems in Equation 2.8 and Equation 2.10 may

[2] For example, if we rescale $\varepsilon'(\mathbf{r}) = \varepsilon(\mathbf{r}/s)$ with the scaling parameter s, we get $\mathbf{r}' = \mathbf{r}s$ and $\nabla' = \nabla/s$. This leads to a frequency $\omega' = \omega/s$ and a mode profile $\mathbf{H}'(\mathbf{r}') = \mathbf{H}(\mathbf{r}'/s)$.

[3] For photonic crystals a mode tends to concentrate its electric-field energy in regions of high dielectric constant, while remaining orthogonal to the modes below it in frequency [32].

be solved numerically for a given configuration of the dielectric function, for more information please check Appendix C.

2.2 Solid-state electromagnetism

We have seen that the master Equation 2.7 can be solved for an arbitrary dielectric media. However, we will restrict ourselves to a particular media known as **photonic crystals**, which have **discrete translational symmetry**. The basic step length of the discrete symmetry in a photonic crystal is known as **lattice constant** a and the basic step vector is known as **primitive lattice vector** $\mathbf{a}$, yielding: $\varepsilon(\mathbf{r}) = \varepsilon(\mathbf{r} + \mathbf{a})$. This means that we will have a periodic repetition of dielectric, where the repeated region is called **unit cell**.

Let us consider the simplest example: the **one-dimensional photonic crystal**. As we can see in Figure 2.1, the system has a primitive lattice vector $\mathbf{a} = a\hat{\mathbf{x}}$. It can be shown that the differential operator $\hat{\Theta}$ defined in Equation 2.9 commutes with the translation operator in the X direction, which means that the eigenmodes of the system may be written as [32]:

$$\mathbf{H}_{k_x}(\mathbf{r}) = \sum_N \mathbf{c}_{k_x,m}(y,z)\mathrm{e}^{\mathrm{i}(k_x+mb)x} = \mathrm{e}^{\mathrm{i}k_x x} \cdot \mathbf{u}_{k_x}(x,y,z)\,, \tag{2.11}$$

where $\mathbf{b} = 2\pi/a\hat{\mathbf{x}}$ is the **reciprocal lattice vector**, $\mathbf{k} = k_x\hat{\mathbf{x}}$ is the **Bloch wave vector**, m is an integer number, $\mathbf{c}$ are the coefficients obtained by solving Maxwell's equation and $\mathbf{u}_{k_x}(x,y,z)$ is a periodic vector function. This vector is also known as **Bloch state** and acts as a periodic function that modulates the plane waves.

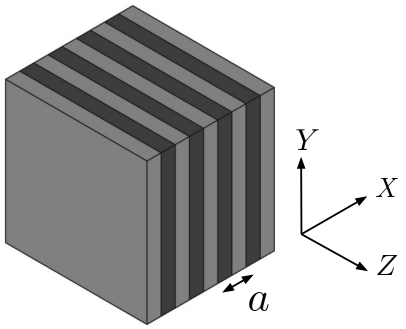

Figure 2.1.: Example of a one-dimensional photonic crystal structure, where the dielectric constant changes periodically in the X direction with lattice constant a and is infinite in the YZ plane.

As a matter of fact, the problem we are solving may be directly mapped to solid-state physics, where we have an electron propagating through a periodic potential. Here the potential is replaced by the dielectric function and the wave-function of the electron is now the mode profile of the light propagating in the photonic crystal. That is, alike in solid-state physics, Equation 2.12 shows **Bloch's theorem** [35]. This means that for a general 3D photonic crystal, we may write the mode profiles as:

$$\mathbf{H}_{\mathbf{k}}(\mathbf{r}) = e^{i\mathbf{k}\cdot\mathbf{r}}\mathbf{u}_{\mathbf{k}}(\mathbf{r})\,, \tag{2.12}$$

where $\mathbf{u}_{\mathbf{k}}(\mathbf{r}) = \mathbf{u}_{\mathbf{k}}(\mathbf{r}+\mathbf{R})$ is a periodic function for all lattice vectors $\mathbf{R}$. As a consequence of the periodicity of the Bloch state mode frequencies will also be periodic. Returning to the one-dimensional photonic crystal in Figure 2.1, frequencies will be periodic in k_x: $\omega(k_x) = \omega(k_x + mb)$. Therefore, in this case we only need to consider k_x lying in the **Brillouin zone**, where there is only one period of the solution, in this case, the interval $(-\pi/a, \pi/a)$. For a more in-depth introduction of solid-state physics concepts please check Appendix D.

We may return from our simple one-dimensional example to the general case, where using the information about Bloch states $\mathbf{u}_{\mathbf{k}}(\mathbf{r})$ we can describe our system together with the master Equation 2.7:

$$\nabla \times \frac{1}{\varepsilon(\mathbf{r})}\nabla \times e^{i\mathbf{k}\cdot\mathbf{r}}\mathbf{u}_{\mathbf{k}}(\mathbf{r}) = \left(\frac{\omega(\mathbf{k})}{c}\right)^2 e^{i\mathbf{k}\cdot\mathbf{r}}\mathbf{u}_{\mathbf{k}}(\mathbf{r})\,. \tag{2.13}$$

If we develop the expression further we obtain the **Bloch master equation**:

$$(i\mathbf{k}+\nabla) \times \frac{1}{\varepsilon(\mathbf{r})}(i\mathbf{k}+\nabla) \times \mathbf{u}_{\mathbf{k}}(\mathbf{r}) = \left(\frac{\omega(\mathbf{k})}{c}\right)^2 \mathbf{u}_{\mathbf{k}}(\mathbf{r})\,, \tag{2.14}$$

which can be written as $\hat{\Theta}_{\mathbf{k}}\mathbf{u}_{\mathbf{k}}(\mathbf{r}) = (\omega(\mathbf{k})/c)^2\mathbf{u}_{\mathbf{k}}(\mathbf{r})$, where $\hat{\Theta}_{\mathbf{k}}$ is the Hermitian operator:

$$\hat{\Theta}_{\mathbf{k}} = (\mathbf{ik}+\nabla) \times \frac{1}{\varepsilon(\mathbf{r})}(\mathbf{ik}+\nabla) \times\ . \tag{2.15}$$

Since the mode profiles are determined by Equation 2.12 they will be periodic. Therefore, we can restrict the solution of the problem to a single unit cell. Furthermore, since we restrict ourselves to a solution in a finite volume we know that there will be a **discrete spectrum** of eigenvalues [32]. We expect an infinite set of modes, which can be given a band number n, at discretely

separated frequencies for each $\mathbf{k}$. Therefore varying $\mathbf{k}$ continuously we can find a family of continuous functions $\omega_n(\mathbf{k})$, which is also known as the **band structure** of the photonic crystal. In very few analytical cases[4] we may be able to solve for the band structure analytically. In general, however, we will calculate it numerically by solving the eigenvalue problem in Equation 2.14, as explained in Appendix C.

2.3 One dimensional photonic crystals

One-dimensional photonic crystals were first studied by Lord Rayleigh when he studied the physical properties of multilayer films [36]. In Figure 2.1 we showed the example of a **multilayer film** which is a one-dimensional photonic crystal composed of alternating layers of different dielectric constant. This means that material is homogeneous in a plane and has discrete translational symmetry, with lattice constant a, in the directional perpendicular to that plane. We can generalize Equation 2.12, to account for in-plane propagation and write the modes in the Bloch form in three dimensions [32]:

$$\mathbf{H}_{n,k_x,\mathbf{k}_\parallel} = \mathrm{e}^{\mathrm{i}\mathbf{k}_\parallel\cdot\rho}\mathrm{e}^{\mathrm{i}k_x x}\mathbf{u}_{n,k_x,\mathbf{k}_\parallel}(x,y,z)\,, \tag{2.16}$$

where ρ is the in-plane coordinate, $\mathbf{k}_\parallel$ is the in-plane wave-vector, x is the out of plane coordinate, k_x is the out-of-plane wave-vector and n is the band number. One can then solve Equation 2.14 and find the mode profiles of the fields in the Brillouin zone $-\pi/a < k_x \leq \pi/a$.

2.3.1 Transfer Matrix Method

We have previously studied infinite one-dimensional systems with continuous or discrete translational symmetry along a given direction. It is possible to gain intuition and understanding on these systems by using the **Transfer Matrix Method (TMM)**, a one-dimensional toy model which is based on Lord Rayleigh's pioneering work where he studied multilayer films based on the reflections and refraction at the different interfaces.

[4] One of this cases is the Transfer Matrix Method, which we cover in Section 2.3.1.

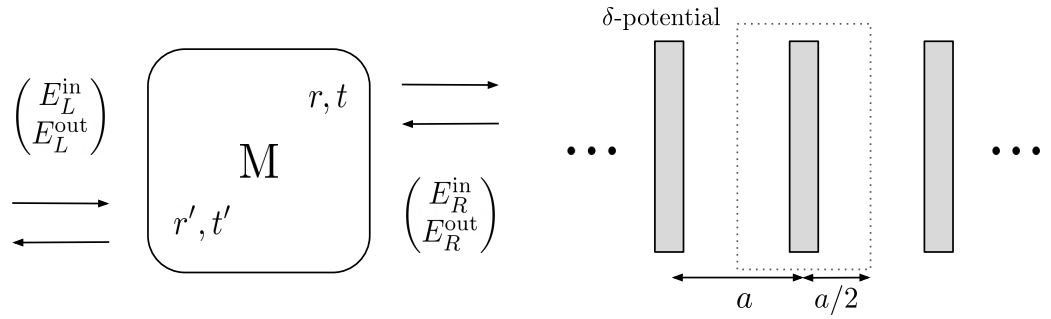

(a) Transfer matrix and fields. **(b)** Unit cell of the model of a multilayer film.

Figure 2.2.: Conventions in the TMM formalism. **(a)** Relation of the input and output fields at both sides of the transfer-matrix M. **(b)** Unit-cell of a one-dimensional photonic crystal δ-function barrier model.

This formalism works by modelling our system with concatenated optical elements, where the system can then be expressed as the matrix product of the different elements. A general **transfer matrix M** relates the field on the right of the optical elements to the field on the left, by taking into account reflection and transmission amplitudes [33]:

$$\mathbf{E_l} = \mathbf{M}\mathbf{E_r} \quad \Longleftrightarrow \quad \begin{pmatrix} E_L^{\text{out}} \\ E_L^{\text{in}} \end{pmatrix} = \frac{1}{t} \begin{pmatrix} tt' - rr' & r' \\ -r & 1 \end{pmatrix} \begin{pmatrix} E_R^{\text{out}} \\ E_R^{\text{in}} \end{pmatrix} \tag{2.17}$$

where r and t are the reflection and transmission amplitudes from the right respectively and r' and t' are the reflection and transmission amplitudes from the left. One can relate these to the matrix elements in **M** using Equation 2.17:

$$r = -\frac{M_{21}}{M_{22}}, \qquad t = \frac{1}{M_{22}}, \qquad r' = \frac{M_{12}}{M_{22}}, \qquad t' = \frac{\det \mathbf{M}}{M_{22}}. \tag{2.18}$$

In our case we will try to **model one-dimensional photonic crystals by using a set of scatterers in vacuum**. To describe this system we just need to describe the matrices corresponding to two optical elements. The first is the matrix that describes **isotropic propagation in free space** [33]:

$$\mathbf{P}(x) = \begin{pmatrix} e^{ikx} & 0 \\ 0 & e^{-ikx} \end{pmatrix}, \tag{2.19}$$

$k = \omega/c$ is the wave-vector and x is distance travelled by the plane wave. The other element that we will be using is the **δ-function barrier**. The fields at

both sides of the barriers can be related as in Equation 2.17, but in this case having $t = t'$ and $r = r'$ [33]:

$$\mathbf{I}(\chi) = \frac{1}{t}\begin{pmatrix} t^2 - r^2 & r \\ -r & 1 \end{pmatrix} = \begin{pmatrix} 1 + i\chi & i\chi \\ -i\chi & 1 - i\chi \end{pmatrix}, \tag{2.20}$$

where $\chi = -ir/t$[5]. Using these elements we can build the transfer-matrix for the unit cell in Figure 2.2a of a one-dimensional photonic crystal with lattice constant a:

$$\mathbf{U}_{\text{cell}}(\chi, a) = \mathbf{P}\left(\frac{a}{2}\right)\mathbf{I}(\chi)\mathbf{P}\left(\frac{a}{2}\right) = \begin{pmatrix} (1 + i\chi)e^{ika} & i\chi \\ -i\chi & (1 - i\chi)e^{-ika}. \end{pmatrix}, \tag{2.21}$$

where we model the unit cell of a photonic crystal as an infinite periodic system where there are δ-potential barriers separated by a lattice constant distance a, similar to the **Kronig-Penney model** in [33]. One may calculate the dispersion relation of the system by taking the trace of the unit-cell transfer matrix[6] [33]:

$$2\cos(\beta a) = \text{Tr}(\mathbf{U}_{\text{cell}}) \quad \longrightarrow \quad \cos(\beta a) = \cos(ka) - \chi\sin(ka). \tag{2.22}$$

This equation relates the propagation constant β to the frequency $\omega = ck$, which allows us to reconstruct the band diagram in Figure 2.3. Since the left hand side in Equation 2.22 will be bounded in the range $(-1, 1)$ for $\beta \in \mathbb{R}$ it means that for certain values of the the frequency the propagation constant has no real value; in other words, in that range of frequencies, known as **band-gap**, waves cannot propagate inside the crystal.

One can calculate the band-edge frequencies by setting $\beta = \pi/a$ and solving for $\omega = ck$. Solving for the two roots of the equation in the Brillouin zone yields:

$$\omega_+ = \frac{\pi c}{a} \tag{2.23}$$

$$\omega_- = \frac{c}{a}\cosh^{-1}\left(\frac{\chi^2 - 1}{\chi^2 + 1}\right). \tag{2.24}$$

[5] Although in general the TMM only requires continuity ($r + t = 1$), in this work we only will work with lossless scatterers, so $|r|^2 + |t|^2 = 1$.

[6] Since the unit-cell matrix fulfills $\det(\mathbf{U}_{\text{cell}}) = 1$ it will have the eigenvalues: $\lambda_\pm = e^{\pm i\beta a}$ [33].

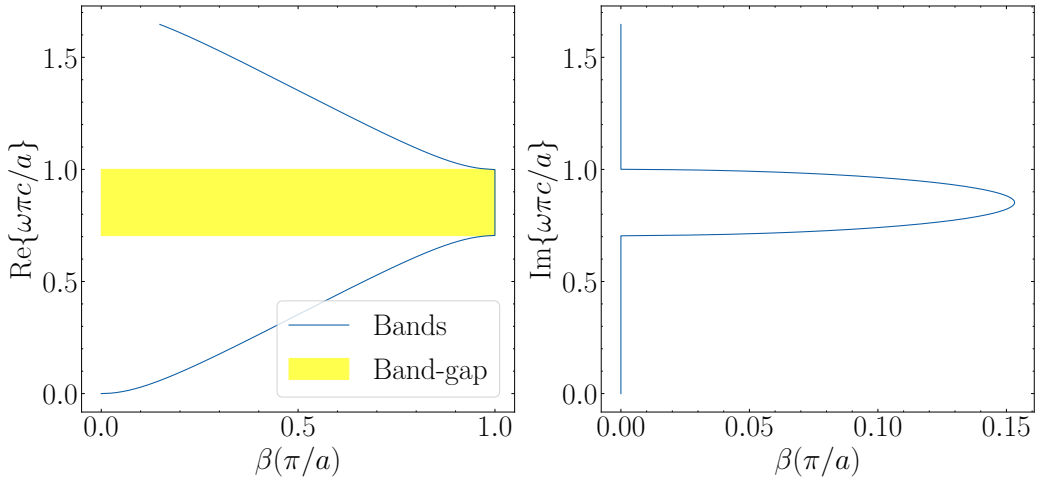

Figure 2.3.: Band structure for a one-dimensional photonic crystal with $\chi = 0.4$ in the Brillouin zone. We plot the real and imaginary parts of the frequency $\omega = ck$ as a function of the propagation constant β, both in their corresponding adimensional units.

One can prove that for small $\chi \ll 1$ the size of the band-gap can be approximated as:

$$\Delta\omega = \omega_+ - \omega_- \simeq \frac{2\chi c}{a}\,. \tag{2.25}$$

This result is telling us that we can change the size of the band gap by changing the reflectivity of the scatterer. In the case of an interface between media we know that from **Fresnel equations** at normal incidence [33]:

$$r = \frac{n_a - n_b}{n_a + n_b} \tag{2.26}$$

$$t = \frac{2n_a}{n_a + n_b}\,, \tag{2.27}$$

so that $|\chi| \propto |r/t| \propto |n_a - n_b|$. This means that **increasing the index contrast between two materials, or the reflectivity of the scatterers, will result in a larger band-gap**. We can also better understand what happens in the band-gap of a photonic crystal by rewriting the propagation constant in Equation 2.22 using a complex propagation constant $\beta_{\text{gap}} = \pi/a + i\kappa$, since the real part is constant inside the gap. Substituting these values gives:

$$\cosh(\kappa) = -\cos(ka) + \chi \sin(ka)\,. \tag{2.28}$$

The maximum propagation constant is achieved at the center of the gap where:

$$\kappa_{\text{max}} = \frac{\arccos\left(\sqrt{1+\chi^2}\right)}{a}\,. \tag{2.29}$$

This is important, because in the band-gap light cannot propagate. Therefore, the field in the band-gap becomes **evanescent**: $\mathbf{E}(\mathbf{r}) \propto e^{ikx}\mathbf{u}(x)e^{-\kappa x}$. This means that it will decay exponentially with a **decay-length** scale of $1/\kappa$. In our case in Figure 2.3, at the center of the gap $\kappa\, a \simeq 0.5$, which means that the decay-length is $l \simeq 2a$.

As we will see in the following sections the **group velocity** of the light field plays a central role in enhancing atom-light interactions. It is possible to calculate the group velocity from the dispersion-relation in Equation 2.22:

$$v_g = \frac{d\omega}{d\beta} = \frac{c \sin(\beta a)}{\sin(ka) + \chi \cos(ka)}\,. \tag{2.30}$$

As we can see in Figure 2.3 bands tend to be flatter close to the band-edges, which results in small group velocity. One may expand the dispersion relation Equation 2.22 for $\delta\beta = \pi/a - \beta$ and then calculate the group-velocity:

$$\omega \simeq \omega_{\pm} \pm \frac{ca}{2\chi}\delta\beta^2 \quad \longrightarrow \quad v_g \simeq \mp\frac{ca}{\chi}\delta\beta\,. \tag{2.31}$$

As expected, we see that near the band-edge the group velocity approaches zero and therefore, the **group-index** $n_g = c/v_g$ diverges.

The TMM formalism also allows us to calculate the field distributions by using the eigenvectors of the unit-cell matrix Equation 2.21 [33]:

$$\mathbf{u}_{\beta} = \frac{1}{\sqrt{1+f^2}}\begin{pmatrix}1\\ f\end{pmatrix}, \qquad \mathbf{u}_{-\beta} = \frac{1}{\sqrt{1+f^2}}\begin{pmatrix}f\\ 1\end{pmatrix}. \tag{2.32}$$

where f is defined as:

$$f = -\frac{\sqrt{n_g^2 - 1}}{n_g + 1} = -\mathrm{sgn}(n_g)\sqrt{r_g}\,, \tag{2.33}$$

where $r_g = (n_g - 1)/(n_g + 1)$ is the Fresnel coefficient between two interfaces $n_1 = 1$, $n_2 = n_g$ as in Equation 2.27. Using previously obtained results we expect reflection to approach unity at the band-edge, since the group-index will diverge. This means that for the lower band-edge we obtain $f = 1$ and

for the lower band-edge we obtain $f = -1$. Using these expressions we can calculate the electric field and intensity for a field with positive wavevector:

$$E_\beta(x) = \frac{1}{\sqrt{1+f^2}}(e^{ikx} + f e^{-ikx}) \longrightarrow |E_\beta(x)|^2 = \frac{1}{1+f^2}(1+f^2+2f\cos(2kx))\,. \tag{2.34}$$

For the band edges we get electric field profile that are **standing waves**:

$$E_{BE,+}(x) = \sqrt{2}\cos k_+ x = \sqrt{2}\cos\left(\frac{\pi}{a}x\right) \tag{2.35}$$

$$E_{BE,-}(x) = -i\sqrt{2}\sin k_- x \simeq -i\sqrt{2}\sin\left(\frac{\pi - 2\chi}{a}x\right) \tag{2.36}$$

As we can see from these expressions as well as from Figure 2.4, the field intensity for the upper band maximizes at the scatterer position, whereas the field intensity for the upper band maximizes between scatterers. This is why the lower band is known as **dielectric band** whereas the upper band is known as **air band**. In Figure 2.4 we consider very weak scatterers $\chi \ll 1$, so that we may apply perturbation theory to Maxwell's equations to understand why there is a frequency difference between both modes [32]:

$$\Delta\omega = -\frac{\omega}{2}\frac{\int d^3\mathbf{r}\Delta\chi(\mathbf{r})|\mathbf{E}(\mathbf{r})|^2}{\int d^3\mathbf{r}\chi(\mathbf{r})|\mathbf{E}(\mathbf{r})|^2} + \mathcal{O}(\Delta\chi^2)\,, \tag{2.37}$$

taking into account that in our model $\chi(\mathbf{r}) \propto \varepsilon(\mathbf{r})$. We can also understand why the band-gap appears: **the mode under the band-gap will have a lower frequency because it is more concentrated in low-dielectric constant regions**, whereas the contrary is true for the upper band.

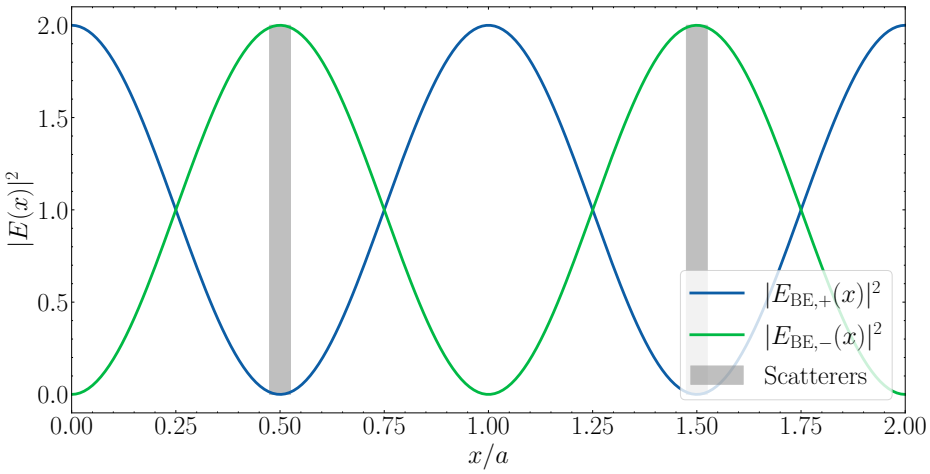

Figure 2.4.: Intensity of the Bloch modes at the upper and lower side of the band edge for $\chi \ll 1$.

In our experimental framework, we will work with non-infinite photonic crystals that will fabricated and characterized in the laboratory. We can extend our formalism to finite structures by writing the transfer-matrix for a N unit-cell photonic crystal as:

$$\mathbf{U}_N = \prod_{i=0}^{N} \mathbf{U}_{\text{cell}} = \mathbf{U}_{\text{cell}}^N \,. \tag{2.38}$$

Using the transformation that diagonalizes the unit-cell matrix [33]:

$$\mathcal{O} = \frac{1}{1-f^2} \begin{pmatrix} 1 & f \\ f & 1 \end{pmatrix} . \tag{2.39}$$

We can rewrite Equation 2.38:

$$\begin{aligned} \mathbf{U}_N &= \mathcal{O}\mathcal{O}^{-1}\mathbf{U}_{\text{cell}}\mathcal{O}\mathcal{O}^{-1}\mathbf{U}_{\text{cell}} \ldots \mathcal{O}^{-1}\mathbf{U}_{\text{cell}}\mathcal{O}\mathcal{O}^{-1} \\ &= \mathcal{O}\mathbf{D}^N\mathcal{O}^{-1} = \mathcal{O} \begin{pmatrix} e^{iN\beta a} & 0 \\ 0 & e^{-iN\beta a} \end{pmatrix} \mathcal{O}^{-1} \\ &= \frac{1}{1-f^2} \begin{pmatrix} e^{iN\beta a} - f^2 e^{-iN\beta a} & -2if\sin(N\beta a) \\ 2if\sin(N\beta a) & e^{-iN\beta a} - f^2 e^{iN\beta a} \end{pmatrix} \end{aligned} \tag{2.40}$$

where we have used the diagonalized unit-cell matrix:

$$\mathcal{O}\mathbf{U}_{\text{cell}}\mathcal{O}^{-1} = \mathbf{D} = \begin{pmatrix} e^{i\beta a} & 0 \\ 0 & e^{-i\beta a} \end{pmatrix} . \tag{2.41}$$

We can also calculate the transmission and reflection coefficients of the structure following Equation 2.18:

$$t_N = \frac{1}{\mathbf{U}_N^{22}} = \frac{1-f^2}{e^{-iN\beta a} - f^2 e^{iN\beta a}} \qquad r_N = \frac{\mathbf{U}_N^{12}}{\mathbf{U}_N^{22}} = -\frac{2if\sin(N\beta a)}{e^{-iN\beta a} - f^2 e^{iN\beta a}} \,. \tag{2.42}$$

In Figure 2.5 we have plotted the power transmission $T_N = |t_N|^2$ and power reflection $R_N = |r_N|^2$ for $\chi = 0.2$. We see that the curves are modulated by

resonances[7], that become narrower close to the band-edge. They are thus called **band-edge resonances**. From Figure 2.5 we can conclude that as one increases the number of unit-cells the resonances also become narrower. As a matter of fact, it is possible to determine the frequency of these resonances. In Figure 2.5 we see that at these resonances r_N is zero, which means $\sin(N\beta a) = 0$. This means that we have resonances when:

$$\beta_n = \left(1 - \frac{n}{N}\right)\frac{\pi}{a}, \tag{2.43}$$

for the resonance index n. One then may solve the dispersion relation in Equation 2.22 to calculate the frequency of the resonance. Close to the band-edge one can expand this as:

$$\omega_{\pm,n} = \omega_{\pm} \pm \frac{n^2 c\pi^2}{2\chi a N^2}. \tag{2.44}$$

Similarly for the group velocity one may also calculate its value near the band-edge:

$$v_{g,n} = \pm\frac{n\pi c}{N\chi}. \tag{2.45}$$

This means that similar to the resonances in the transmittance and reflectance shown in Figure 2.5 we will also have them for the group-velocity and the group-index, since: $n_{g,n} = c/v_{g,n}$. Using the group-index it is also possible to calculate the expect transmission and reflection amplitudes using the definition of f in Equation 2.33 and Equation 2.42.

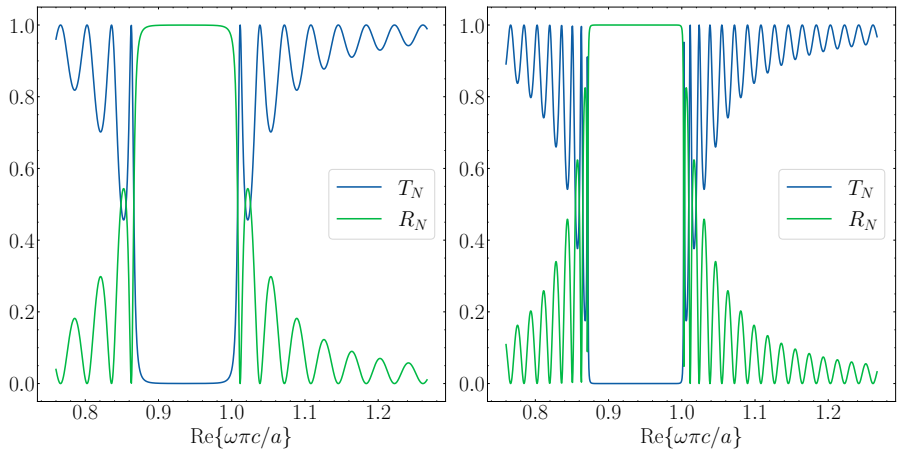

Figure 2.5.: Transmission and reflection spectrum for $\chi = 0.2$. On the left, for $N = 25$ unit-cells and on the right for $N = 50$ unit-cells.

[7] These resonances will also be found in the electric fields that propagate through the photonic crystals, so that we will have an effective envelope function, known as **supermode modulation**.

2.4 Beyond one dimension

In the previous sections we have studied the physical properties of one-dimensional photonic crystals. We have done so, because their properties are just reproduced in higher dimensional photonic crystals. As we see in Figure 2.6, in the case of two-dimensional photonic crystals one has discrete translational periodicity in one plane, and this just adds some extra layers of complexity. For two-dimensional photonic crystals the Bloch states are:

$$\mathbf{H}_{(n,\mathbf{k}_\parallel,k_z)}(\mathbf{r}) = \mathrm{e}^{\mathrm{i}\mathbf{k}_\parallel\cdot\rho}\mathrm{e}^{\mathrm{i}k_z z}\mathbf{u}_{(n,k_z,\mathbf{k}_\parallel)}(\mathbf{x},\mathbf{y})\,. \tag{2.46}$$

Remember that $\rho = \mathbf{x} + \mathbf{y}$ is the in plane vector, s that the Bloch mode is periodic as $\mathbf{u}(\mathbf{r}) = \mathbf{u}(\mathbf{r} + \mathbf{R})$ for all lattice vectors $\mathbf{R}$.

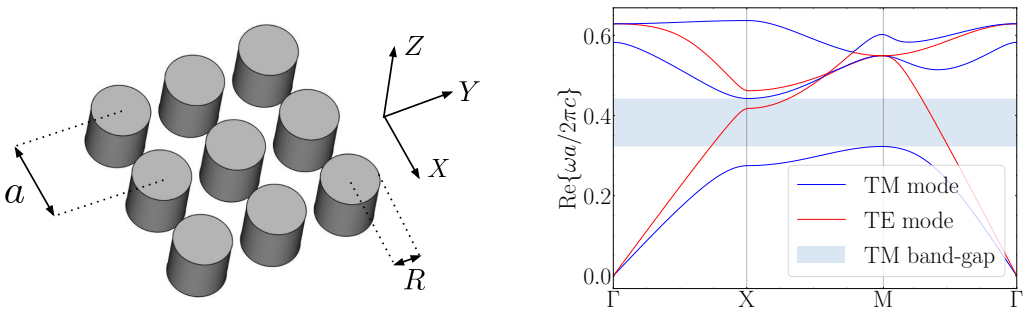

(a) Square lattice of dielectric rods. **(b)** Photonic band-structure.

Figure 2.6.: Example of a two-dimensional photonic crystal and its band structure. **(a)** Square lattice with lattice constant a, of dielectric rods with radius R. Note that the rods should be infinite in height. **(b)** The associated band-diagram where we have fixed the parameters $\varepsilon = 8.9\varepsilon_0$ and $R = 0.2a$. For a review on the (Γ, X, M) k point-notation refer to Appendix D.

In this particular geometry we have a mirror symmetry around the XY plane so it is possible to separate the modes into two distinct polarizations [32]: the **Transverse-Electric** (TE) modes, where the electric field is in the plane and the magnetic field is perpendicular to the plane and the **Transverse-Magnetic** (TM) modes, where the electric field is perpendicular to the plane and the magnetic field is in the plane. In Figure 2.6b we show that the mode dispersion relations differ for the two polarizations. For instance, we see that for the TM modes we have a band-gap, whereas this is not true for TE modes. One can prove as in [32] that **TM band-gaps are favored in a lattice of isolated high-ε regions**, like in Figure 2.6a, and **TE band-gaps are favored in a connected lattice**. By designing a photonic crystal that has both traits one can make the

two band-gaps overlap and obtain a **complete band-gap** that is independent of polarization. For more information on two- and three-dimensional photonic crystal please refer to [32].

2.4.1 Finite cross sections: waveguides and slabs

In real-life it is not possible to fabricate structures that are infinite in any of their dimensions. In our work, we will mainly be concerned with **periodic dielectric waveguides**, which have a structure with discrete translational symmetry in one dimension but finite thickess, and **photonic crystal slabs**, which have discrete translational symmetry in one plane but finite thickness. For instance, in Figure 2.7a we show an example of a photonic crystal slab.

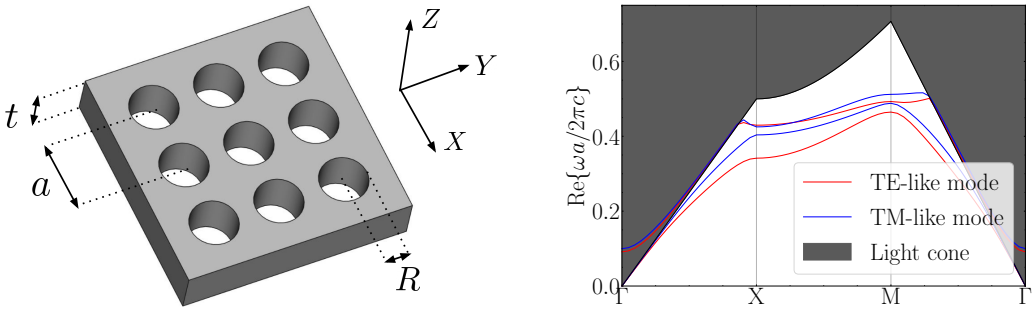

(a) Square lattice of circular hole slab. **(b)** Photonic band-structure.

Figure 2.7.: Example of a two-dimensional photonic crystal slab and its band-structure. **(a)** Slab of thickness t, with square lattice of circular holes with lattice constant a and of radius R. **(b)** The associated band-diagram where we have plotted the dielectric and air TE- and TM-like bands for the design parameters $(a, t, R) = (290, 180, 103)$ nm as in [12]. For a review on the (Γ, X, M) k point-notation refer to Appendix D.

The finite thickness of the structures makes it possible to guide light through them, by **index guiding**. Similar to total internal reflection, as described by Snell's law, there will be a set of modes that will be confined to the dielectric, whereas others will extend into infinity. Those that extend into infinity will go towards free-space, which means that they must be a superposition of plane waves with $\omega = c|\mathbf{k}| = c\sqrt{k_\parallel^2 + k_\perp^2}$. For a certain value of $k_\parallel$ there will be modes with every possible frequency greater than $ck_\parallel$, since $k_\perp$ can take any value. This means that the spectrum is continuous for frequencies above the **light line** $\omega = ck_\parallel$. As we see in Figure 2.7b[8], the photonic crystal structure

[8] Compared to their two- and three-dimensional counterparts modes in the band-diagram cannot be separated into two distinct polarizations; instead, for thin structures fields have

introduces new modes that lie below the light line. The region of the band structure above the light line is known as **light cone**. Below the light line we have modes that have lower frequencies relative to the corresponding values in free space according to Equation 2.37, since ε is higher in the dielectric than air. These **index guided modes** have to be localized in the dielectric, since in air they have imaginary $k_\perp = i \pm \sqrt{k_\parallel - \omega^2/c^2}$, corresponding to **evanescent fields**.

Additionally, a light cone results in **incomplete band-gaps**, where only the index guided modes will be suppressed in the gap but there will still be **radiating modes** for any ω, at both sides of the light cone. In our particular application this is very important, because we want to couple as much light as we can from the quantum emitters into the evanescent or propagating modes of the photonic crystal, without coupling to the radiation modes.

TE- or TM-like polarizations. This happens, because in the long distance limit, or when the thickness is smaller than the wavelength, the fields only see the dielectric shortly.

Atom-light interactions

3

" Bainan oraingoan, isil isilikan eta arrangurarik gabe, nahita ondoratuko naiz zure adio mugagabearen sakonean."

— Benito Lertxundi, *Isil isilik.*

Now that we understand how we can control the properties of light using photonic crystals we will learn how these nanophotonic structures interact with atoms and modify their way of emitting light, using the TMM and the Green's function formalisms, inspired by the theoretical work developed in [37].

Specially relevant for the experimental platform is to understand the key concepts that will be introduced in this chapter:

- Atoms can accurately be modeled as **narrow band scatterers** or either as **dipoles** in the classical limit.
- **The coupling rate** of an atom and the guided mode in a photonic crystal environment can be **enhanced** by positioning the atom in a location of high Bloch mode intensity and cavity enhancement while achieving low-group velocity and small mode area.
- It is possible to couple the atoms to the guided mode of a photonic crystal and achieve different types of **interactions** between atoms:
  - Collective **superradiant** and **subradiant** states, which result in enhanced and suppressed decay rates, respectively.
  - **Dissipative interactions** between atoms, mediated by the guided modes of the photonic crystal.
  - **Dispersive interactions** between atoms, mediated by the evanescent fields in the band-gap of the photonic crystal.

3.1 Atoms in the Transfer Matrix Method

To better understand how atoms behave in the presence of nanophotonic structures we may return to the TMM formalism introduced in Section 2.3.1, which we used as a one-dimensional toy model used to get hold of the main physics. Now we will approximate atoms as narrow band scatterers and forget about their inherent quantum nature, which means that all results in this section only hold for the **low saturation limit**[1].

As depicted in Figure 3.1 in our model the atomic scatterers will emit light with a frequency ω_A into the nanophotonic waveguides[2] with a rate $\gamma_{1D} = \frac{\sigma_0}{2A_{\text{eff}}}\Gamma_0$ with the free-space decay rate is Γ_0, the effective mode are A_{eff}, the atom's radiative cross-section $\sigma_0 = \frac{6\pi c^2}{\omega_A^2}$, and the loss into radiation modes Γ' [39]. We will come back to some of these concepts in more detail later in this chapter.

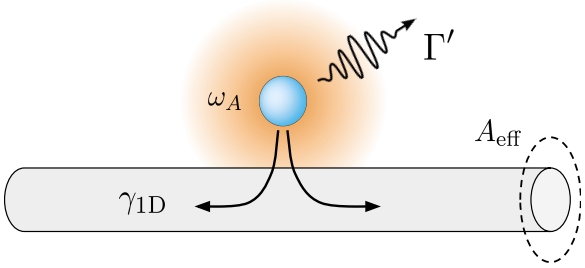

Figure 3.1.: Atoms can be modelled as narrow band scatterers emitting with a frequency ω_A. Atoms close to an unstructured waveguide will decay into the guided modes of the structure with effective mode area A_{eff} at a rate γ_{1D}. On the flip side, some of their energy will be lost at a the rate Γ' into free space. Figure adapted from [39].

We may understand the reflection of an atom as a saturable mirror, given in [39] and [40] by the expression:

$$r = -\frac{\gamma_{1D}}{\gamma_{1D} + \Gamma'} \frac{1}{1 - i2\Delta_A/(\gamma_{1D} + \Gamma')}, \tag{3.1}$$

[1] Which means that atoms will mostly be in the ground state and the atomic excited state population can be neglected [38]. In this limit atoms effectively behave as classical dipoles.
[2] The waveguiudes can be modelled using the TMM formalism as introduced in Chapter 2.

where $\Delta_A = \omega - \omega_A$ is the detuning from the transition frequency ω_A. In this context we may express the transfer matrix of an atom as [37]:

$$\mathbf{A}(\chi_0) = \begin{pmatrix} 1 + i\chi_0 & i\chi_0 \\ -i\chi_0 & 1 - i\chi_0 \end{pmatrix}, \tag{3.2}$$

where $\chi_0 = -ir/t$. Using the continuity ($r + t = 1$), we get that:

$$\chi_0 = i\frac{\gamma_{1D}}{\Gamma'}\frac{1}{1 - i2\Delta_A/\Gamma'}. \tag{3.3}$$

Let's place this atom in a one-dimensional photonic crystal structure as in Figure 3.2. One may then write the total transfer-matrix similar to Equation 2.40 as in [37]:

$$\begin{aligned} \mathbf{U}_{\infty,\,\text{atom}} &= \ldots \mathbf{U}_{\text{cell}}\, \mathbf{P}(-x)\mathbf{A}(\chi_0)\mathbf{P}(x)\mathbf{U}_{\text{cell}} \ldots \\ &= \mathcal{O}\mathbf{D}^{\infty}\mathcal{O}^{-1}\mathbf{P}(-x)\mathbf{A}(\chi_0)\mathbf{P}(x)\mathcal{O}\mathbf{D}^{\infty}\mathcal{O}^{-1}. \end{aligned} \tag{3.4}$$

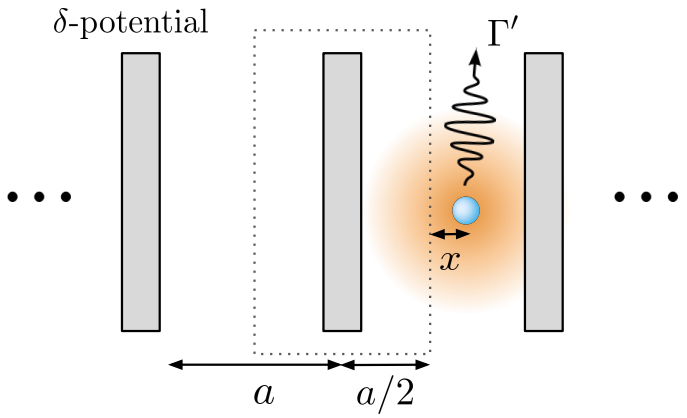

Figure 3.2.: Infinite photonic crystal with a single in one unit-cell at a distance x of the next unit-cell to the left. The atom (blue) acts as a system with losses Γ', which are linked to the emission into radiation modes. Figure adapted from [37].

We may rewrite this expression as the effective transfer matrix of a **dressed atom** as suggested in [37]:

$$\begin{aligned} \mathbf{A}_{\text{eff}}(x) &= \mathcal{O}^{-1}\mathbf{P}(-x)\mathbf{A}(\chi_0)\mathbf{P}(x)\mathcal{O} \\ &= \mathbf{P}(-l_{\text{eff}})\mathbf{A}(\chi_{\text{eff}})\mathbf{P}(l_{\text{eff}}) \end{aligned} \tag{3.5}$$

with

$$\chi_{\text{eff}}(x) = \chi_0 \frac{1 + 2f\cos(2kx) + f^2}{|1 - f^2|}\,, \tag{3.6}$$

$$l_{\text{eff}}(x) = x - \frac{1}{2k}\arg\left(\frac{1 + fe^{2ikx}}{1 + fe^{-2ikx}}\right)\,. \tag{3.7}$$

Interestingly, one can understand the physics of this equivalence better by using Equation 2.33 and Equation 2.34 to apply them in Equation 3.5. This tells us that $\chi_{\text{eff}} = \chi_0 |n_g||E_\beta(x)|^2$. Since in Equation 3.3 we saw that that χ_0 is proportional to the decay into the unstructured waveguide $\gamma_{1\text{D}}$, we can define a **spatial enhanced decay rate**:

$$\Gamma_{1\text{D}} = \gamma_{1\text{D}} |n_g||E_\beta(x)|^2\,. \tag{3.8}$$

This means that the enhancement in the coupling rate of an atom with a waveguide is determined by the group index and is modulated by the Bloch-mode intensity at that point. Therefore, for high atom-light interaction we want to increase the intensity of light at the position of the atom while we have a low group-velocity.

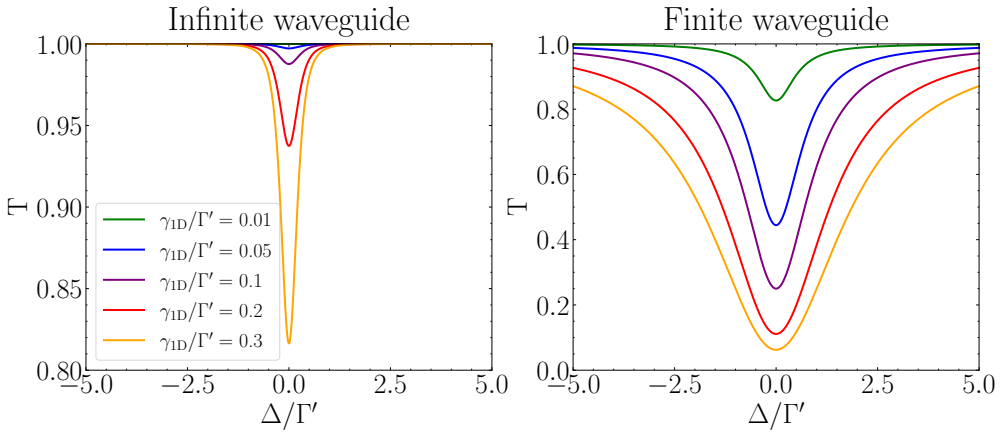

Figure 3.3.: Transmission for an atom in a waveguide. On the left, transmission for a single atom for different decay rates $\gamma_{1\text{D}}$ into the infinite waveguide as a function of the detuning. On the right, transmission and of an atom in a finite waveguide for different overall decay rates $\Gamma_{1\text{D}}$, where we have accounted for cavity enhancement of $|E_\beta|^2 = 2$ and group-index $n_g = 5$.

Using the parameter χ_{eff} one can also calculate the transmission for the effective atom:

$$T(\Delta) = \left|\frac{1}{1 - i\chi_{\text{eff}}}\right|^2 = \frac{\Gamma'^2 + \Delta^2}{\Gamma_{\text{tot}}(x)^2 + 4\Delta^2} \tag{3.9}$$

where the total decay rate is $\Gamma_{\text{tot}} = \Gamma_{1\text{D}}(x) + \Gamma'$. In Figure 3.3 we plot the how the transmission of an atom is modified when one accounts for Bloch mode intensity and slow group-velocity. In fact, with the same unstructured waveguide decay-rate $\gamma_{1\text{D}}$, the Bloch mode intensity and low group velocity drastically enhance the total reflectance of the effective scatterer. In the strong coupling regimes **atoms can then behave as perfect mirrors** [39]. Additionally, the more the decay rate is enhanced with respect to radiation losses, or when $\Gamma_{1\text{D}} \gg \Gamma'$, the bandwidth of the reflector increases.

Let's now consider what happens when we have a single atom inside a finite waveguide of scatterers. Given that we have N_1 unit-cells to the left of the atom and N_2 to the right ($N = N_1 + N_2$):

$$\begin{aligned} \mathbf{U}_{N,\,\text{atom}} &= \mathbf{U}_{\text{cell}}^{N_1}\mathbf{P}(-x)\mathbf{A}(\chi_0)\mathbf{P}(x)\mathbf{U}_{\text{cell}}^{N_2} \\ &= \mathcal{O}\Lambda^{N_1}\mathbf{P}(-l_{\text{eff}})\mathbf{A}(\chi_{\text{eff}})\mathbf{P}(l_{\text{eff}})\Lambda^{N_2}\mathcal{O}^{-1}\,, \end{aligned} \tag{3.10}$$

where we have used the same logic as in Equation 3.5. It is possible to calculate the transmission coefficient from the total transfer matrix, and if normalized to the transmission of the finite structure without atom:

$$\frac{t_{N,a}}{t_N} = \frac{1}{1 - i\chi_{\text{eff}}F(N_1, N_2, x)} \tag{3.11}$$

where:

$$F(N_1, N_2, x) = \frac{(1 + fe^{2i\phi_1})(1 + fe^{2i\phi_2})}{1 - f^2e^{2iN\beta a}} \tag{3.12}$$

with $\phi_1 = N_1\beta a + kl_{\text{eff}}(x)$ and $\phi_2 = N_2\beta a + kl_{\text{eff}}(x)$. The term $F(N_1, N_2, x)$ has the physical meaning of the intensity profile of a cavity mode, as shown in [37]. As we did previously, in this case we can also account for the term $F(N_1, N_2, x)$ in the definition of the **overall decay rate to the finite structure** Γ_{1D}:

$$\Gamma_{1\text{D},N}(N_1, N_2, x) = \gamma_{1D}|n_g||E_\beta(x)|^2 I(N_1, N_2, x)\,. \tag{3.13}$$

This means that in the case of a finite size waveguide the coupling strength is a function of the group-index, the Bloch mode intensity and the cavity enhancement. This means, that it is possible to achieve an even better reflector than the one found in Figure 3.3. To put this into perspective, in the nanofiber experiment at QUANTOP, decay rates of around $0.05 < \gamma_{1\text{D}}/\Gamma' < 0.1$ where found. This showcases the great potential of the photonic crystal waveguide platform to enhance the decay rate.

3.2 Strong atom-light interactions: Green's function formalism

Now that we can understand the atom-light coupling in a first order approximation using the TMM formalism, we will go to a more complete framework using the **Green's function formalism**. Let us return to Section 2.1 where we derived the harmonic expansion of Maxwell's equations, in Equation 2.5 and Equation 2.6. In this case, we will have an atom, or an oscillating dipole[3] in the classical approximation, which means that we will have a null ρ charge-density[4] and a nonzero $\mathbf{J}$ current-density. Taking this into account we can derive the wave equation for the electric field:

$$\nabla \times \nabla \times \mathbf{E}(\mathbf{r},\omega) - \frac{\omega^2}{c^2}\varepsilon(\mathbf{r},\omega)\mathbf{E}(\mathbf{r},\omega) = i\mu_0\omega\mathbf{J}(\mathbf{r},\omega)\,. \tag{3.14}$$

An oscillating polarization density also results in a current given by $\mathbf{J} = \frac{d\mathbf{P}}{dt}$ which in the frequency domain is $\mathbf{J} = -i\omega\mathbf{P}$. This yields:

$$\nabla \times \nabla \times \mathbf{E}(\mathbf{r},\omega) - \frac{\omega^2}{c^2}\varepsilon(\mathbf{r},\omega)\mathbf{E}(\mathbf{r},\omega) = \mu_0\omega^2\mathbf{P}(\mathbf{r},\omega)\,. \tag{3.15}$$

In our case, our atom is an oscillating dipole source $\mathbf{p}_0$ at position $\mathbf{r}_0$, which we can consider as a point source: $\mathbf{P}(\mathbf{r},\omega) = \mathbf{p}_0(\mathbf{r},\omega)\delta(\mathbf{r}-\mathbf{r}_0)$. The solution to the wave equation with this point source is known as the **Green's function** [41] [42]:

$$\nabla \times \nabla \times \mathbf{G}(\mathbf{r},\mathbf{r}';\omega) - \frac{\omega^2}{c^2}\varepsilon(\mathbf{r},\omega)\mathbf{G}(\mathbf{r},\mathbf{r}';\omega) = \overleftrightarrow{I}\delta(\mathbf{r}-\mathbf{r}')\,, \tag{3.16}$$

where $\overleftrightarrow{I}$ is the identity tensor. As we can see the Green's function is inherently dependent on the dielectric environment $\varepsilon(\mathbf{r},\omega)$, which means that it can be engineered by modifying the environment. The Green's function is useful for calculating the electric field from an arbitrary polarization source. The resulting electric field is obtained by integrating the Green's function over the polarization density, as shown by **Dyson's equation** [41] [42]:

$$\mathbf{E}(\mathbf{r},\omega) = \mathbf{E}_0(\mathbf{r},\omega) + \mu_0\omega^2 \int d^3\mathbf{r}'\mathbf{G}(\mathbf{r},\mathbf{r}';\omega)\mathbf{P}(\mathbf{r}',\omega) \tag{3.17}$$

[3] This is a sensible approximation in our system since in general we have $\lambda \gg r_{\text{atom}}$. This is not always the case with other quantum emitters; for instance, quantum dots.
[4] We assume this because our systems are composed of neutral atoms.

where $\mathbf{E}_0$ is the homogeneous solution, or the solution without sources. In the case of the oscillating dipole this simplifies to:

$$\mathbf{E}(\mathbf{r},\omega) = \mathbf{E}_0(\mathbf{r},\omega) + \mu_0\omega^2\mathbf{G}(\mathbf{r},\mathbf{r}_0;\omega)\cdot\mathbf{p}_0\,. \tag{3.18}$$

In general, for arbitrary systems we shall solve for the Green's function numerically. Fortunately, it is possible to calculate an analytical solution in free-space for an oscillating dipole [41]:

$$E_\theta = \mu_0\omega^2|\mathbf{p}|\sin\theta\frac{\omega}{4\pi c}\left[e^{ikr}\left(\overbrace{\frac{1}{k^3r^3}}^{\text{NF}} - \overbrace{\frac{i}{k^2r^2}}^{\text{IF}} - \overbrace{\frac{1}{kr}}^{\text{FF}}\right)\right] \tag{3.19}$$

$$E_r = \mu_0\omega^2|\mathbf{p}|\cos\theta\frac{\omega}{4\pi c}\left[e^{ikr}\left(\frac{2}{k^3r^3} - \frac{2i}{k^2r^2}\right)\right]. \tag{3.20}$$

and the wave vector is $k = \omega/c$. As marked in the equation and depending on the field dependence, we have a near-field (NF), a intermediate-field (IF) and a far-field (FF). In Figure 3.4 we have plotted the near- and far-field of the oscillating dipole. We see that the far field only contains a transverse field which forms the typical **dipole antenna radiation pattern**. In the electrostatic limit $kr \to 0$, the electric near-field simplifies to the DC dipole solution: $\mathbf{E}_{\text{NF}} = \frac{1}{4\pi\epsilon_0}\frac{1}{r^3}[3(\mathbf{p}\cdot\hat{\mathbf{r}}) - \mathbf{p}]$.

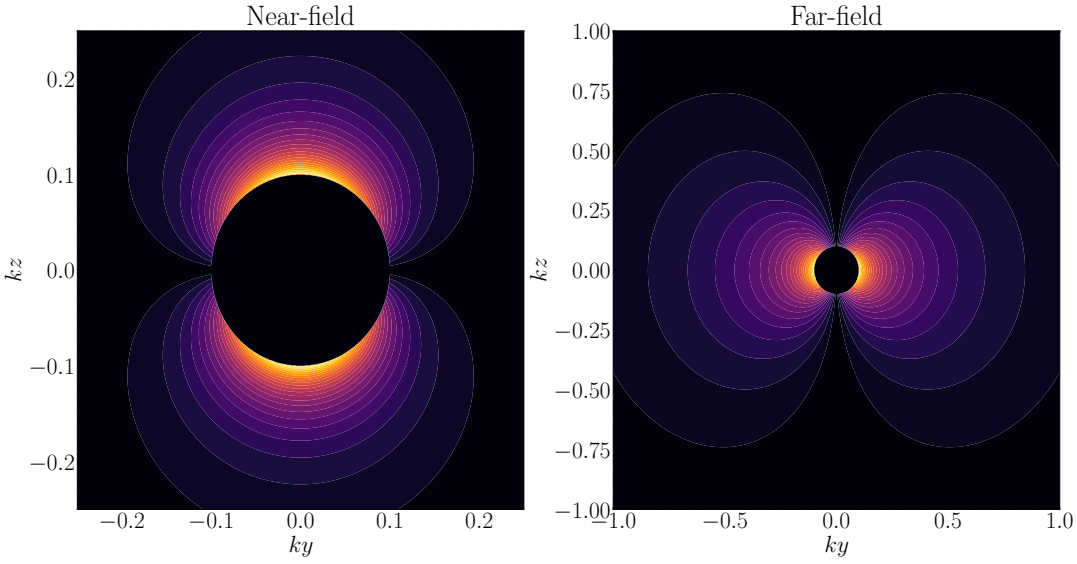

Figure 3.4.: Electric field intensities for an oscillating dipole-moment in arbitrary units. On the left, intensity of the electric near-field and on the right intensity of the electric far-field. We include the black circle to avoid divergences and compare the scale of both plots.

The atoms in our system will be oscillating dipoles and will thus radiate energy into the environment. The time averaged power radiated out of a system P_{rad} can be calculated using [41]:

$$P_{\text{rad}} = -\frac{1}{2}\int d^3\mathbf{r}\text{Re}[\mathbf{J}(\mathbf{r})\cdot\mathbf{E}(\mathbf{r},\omega)]\,, \tag{3.21}$$

where $\mathbf{J}(\mathbf{r}) = -i\omega\mathbf{p}\delta(\mathbf{r}-\mathbf{r}_0)$ is the current generated by the oscillating dipole. Therefore:

$$P_{\text{rad}} = \frac{\omega}{2}\text{Im}[\mathbf{p}^*\cdot\mathbf{E}(\mathbf{r}_0,\omega)]\,. \tag{3.22}$$

Using Equation 3.18 we replace the electric field with the **self-Green's function**:

$$P_{\text{rad}} = \frac{\omega^3|\mathbf{p}|^2}{2\varepsilon_0 c^2}\hat{\mathbf{n}}_p\cdot\text{Im}[\mathbf{G}(\mathbf{r}_0,\mathbf{r}_0;\omega)]\cdot\hat{\mathbf{n}}_p \tag{3.23}$$

where $\hat{\mathbf{n}}_p$ is the unit vector of the dipole. To calculate the decay rate from this radiated power we consider the average energy of the dipole as a spring-mass like oscillator:

$$W = \left\langle m\frac{\dot{x}}{2} + k\frac{x^2}{2}\right\rangle = \left\langle \frac{m}{2q^2}(\omega_0^2 p^2(t) + \dot{p}^2(t))\right\rangle = \frac{m\omega_0^2}{2q^2}|p_0|^2\,, \tag{3.24}$$

where m is the mass and q is the charge of the oscillator. Assuming that the energy decays exponentially with decay rate Γ as $W(t) = W(0)\text{e}^{-\Gamma t}$, the power is related to the energy rate as $P_{rad}(0) = \frac{dW(t)}{dt}|_{t=0} = -\Gamma W(t=0)$. This gives the decay rate:

$$\Gamma = \frac{q^2\mu_0\omega}{2m}\hat{\mathbf{n}}_p\cdot\text{Im}[\mathbf{G}(\mathbf{r}_0,\mathbf{r}_0;\omega)]\cdot\hat{\mathbf{n}}_p\,. \tag{3.25}$$

This means that the decay rate of an oscillating dipole is proportional to the imaginary part of the self-Green's function, and thus, the decay rate of a dipole can be engineered by modifying the environment. Usually, we will want to calculate the ratio of decay rate in a system relative to the decay in free-space. This ratio is known as **Purcell Factor** (PF) and will tell us if the environment enhances or suppresses the emission rate of the dipole. To calculate the free-space decay rate, we perform a Taylor series expansion of the electric fields in Equation 3.19 and Equation 3.20 for small kr. This yields:

$$\lim_{kr\to 0}\mathbf{E}(\mathbf{r},\omega) = \mu_0\omega^2|\mathbf{p}|\frac{\omega}{4\pi c}\left[\frac{2}{(kr)^3} - i\frac{2}{3}\right]\hat{\mathbf{n}}_p\,. \tag{3.26}$$

The electric field is parallel too the dipole orientation and it diverges at zero because we consider a point-like source. In contrast, the imaginary part is

finite and out-of-phase with the oscillating dipole. Using Equation 3.18, the self-Green function is:

$$\mathrm{Im}[\mathbf{G}_0(\mathbf{r}_0, \mathbf{r}_0; \omega)] = \frac{\omega}{6\pi c} \overleftrightarrow{I} \,. \tag{3.27}$$

Replacing this in the decay rate expression in Equation 3.25 we get the free-space decay rate:

$$\Gamma_0 = \frac{\mu_0 \omega^2 q^2}{6mc} \,. \tag{3.28}$$

Now, we can calculate the PF replacing this value:

$$\mathrm{PF} = \frac{\Gamma}{\Gamma_0} = \frac{6c}{\omega} \hat{\mathbf{n}}_p \cdot \mathrm{Im}[\mathbf{G}(\mathbf{r}_0, \mathbf{r}_0; \omega)] \cdot \hat{\mathbf{n}}_p \,. \tag{3.29}$$

As we said previously, the Green's function is dependent on the dielectric configuration of the environment, so it is possible to use the photonic crystals we introduced in Chapter 2 to enhance or suppress the spontaneous emission of the atom. In Figure 3.5 we show the example of an atom embedded in a one- and two-dimensional photonic crystal environment. As we saw in the TMM formalism in Chapter 3.1, we can identify that the electromagnetic field radiated by the atom may couple with the guided modes of these structures $\Gamma_{1D/2D}$, or else couple to the radiation modes Γ' outside of the light cone. It is convenient then to decompose the decay rate in these two components, $\Gamma_{tot} = \Gamma_{1D/2D} + \Gamma'$, as is shown in Figure 3.5. Next, we will see how to better understand the emission into the guided modes by means of the eigenmode expansion.

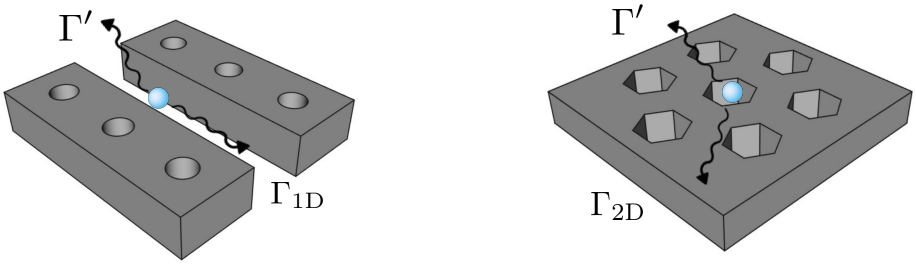

(a) Double nanobeam waveguide. **(b)** Hexagonal photonic crystal slab.

Figure 3.5.: Atom (blue) emitting in a photonic crystal environment. The total emission rate is decomposed in the **(a)** one-dimensional guided mode Γ_{1D} or **(b)** two-dimensional guided mode Γ_{2D} and the emission into radiation modes Γ'.

3.2.1 Eigenmode formalism

To study the coupling to guided modes, we will expand the Green function in terms of the eigenmodes of the photonic crystal. As we have studied previously in Equation 2.10, the electromagnetic wave equation may be written as a generalized eigenvalue problem:

$$\hat{\Theta}\mathbf{E}(\mathbf{r}) = \frac{\omega^2}{c^2}\mathbf{E}(\mathbf{r})\,, \quad \text{where} \quad \hat{\Theta} = \frac{1}{\varepsilon(\mathbf{r})}\nabla\times\nabla\,. \tag{3.30}$$

The eigenmodes will then be dependent of the dielectric function as well as the boundary conditions of the system. For instance, as stated in Equation 2.12, in the case of photonic crystal structures the eigenmodes will have Bloch boundary conditions and will form a complete set. Moreover, the eigenmodes are orthogonal to each other, which means that it is possible expand the Green's function in terms of the eigenmodes [38] [43]:

$$\mathbf{G}(\mathbf{r},\mathbf{r}',\omega) = \frac{c^2}{\omega^2}\sum_{kn}\left(\frac{\omega_{kn}^2}{\omega_{kn}^2-\omega^2}\right)\mathbf{E}_{kn}(\mathbf{r})\otimes\mathbf{E}_{kn}^*(\mathbf{r}')\,. \tag{3.31}$$

This implies that the Green's function may be decomposed into the guided modes of the system and all other modes[5]: $\mathbf{G} = \mathbf{G}_{\text{1D/2D}} + \mathbf{G}'$ where $\mathbf{G}_{\text{1D/2D}}$ is the Green's function of the guided modes and $\mathbf{G}'$ is the Green function over the rest of the modes.

Let us consider the example of an **unstructured waveguide**. Expanding the Green's function in terms of the guided modes of the waveguide, one can prove that the Green's function is [38] [44] [45]:

$$G_{\text{wg,1D}}(x,x') = i\frac{c}{2\omega}e^{ik|x-x'|}\,. \tag{3.32}$$

To model a quasi-one-dimensional system in three dimensions we have to take into account the transverse size of the mode. To account for periodic boundary conditions in the eigenmode formalism we integrate the wave-vector over the Brillouin zone [38] [43]:

$$\mathbf{G}_{\text{wg}}(\mathbf{r},\mathbf{r}',\omega) = \frac{ac^2}{2\pi\omega^2}\sum_{n}\int_{-\pi/a}^{\pi/a}\left(\frac{\omega_n^2(k)}{\omega_n^2(k)-\omega^2}\right)\mathbf{E}_{kn}(\mathbf{r})\otimes\mathbf{E}_{kn}^*(\mathbf{r}')\,. \tag{3.33}$$

[5] Usually the rest of the modes correspond to the radiation modes depicted in Figure 3.4.

It can be proved [38] that developing the previous equation and taking our particular case of a one-dimensional waveguide one obtains:

$$G_{\text{wg,1D}}(\mathbf{r},\mathbf{r}',\omega) = i\frac{c^2}{2\omega v_g A_k}e^{ik|x-x'|}\,, \tag{3.34}$$

where A_k is the mode area A_k is defined as:

$$A_k = \frac{\int_{\text{area}} \mathrm{d}^2\mathbf{r}\varepsilon(\mathbf{r})|\mathbf{E}_k(\mathbf{r})|^2}{\max\{\varepsilon(\mathbf{r})|\mathbf{E}_k(\mathbf{r})|^2|\}}\,. \tag{3.35}$$

From the expression of the Green's function we can calculate the emission into the guided modes. For instance, for the self-Green's function, when $x = x'$, we have a purely imaginary Green's function. This leads to a purely **dissipative** interaction of the atom with itself [6]. Additionally, we also confirm the conclusions that we obtained in the TMM formalism: **to enhance the atom-light interaction we have to decrease the mode area while achieving low group velocity**.

It is possible to solve the Green's function in other analytical cases; such as in the case of a **one-dimensional Fabry-Perot cavity**. For a high finesse[7] symmetry cavity it has been proven [38] [37] that the Green's function can be written as:

$$G_{\text{1D, cav}}(x,x',\omega) = \frac{ic}{m\pi(\kappa/2 + i\Delta_c)}\cos(kx)\cos(kx')\,, \tag{3.36}$$

where $\Delta_c = \omega - \omega_c$ is the detuning from the cavity resonance, m is the resonance index of the cavity mode and $\kappa \simeq \frac{2c(1+r)}{L|r|}$ is the cavity linewidth for a cavity of length L.

We can also solve for the example of a **photonic crystal waveguide** using Equation 3.33 and the Bloch mode calculate in the TMM formalism [37]:

$$G_{\text{pcw,1D}}(x,x',\omega) = \int_0^{\pi/a} d\beta \frac{2c^2}{\omega_\beta^2 - \omega^2}E_\beta(x)E_\beta^*(x')\,. \tag{3.37}$$

Close to the band-edge, this may be approximated by:

$$G_{\text{pcw,1D,+}}(x,x',\omega) \simeq \frac{ic}{kv_g}e^{i\left(k-\frac{\pi}{a}\right)|x-x'|}\cos\left(\frac{\pi}{a}x\right)\cos\left(\frac{\pi}{a}x'\right)\,, \tag{3.38}$$

[6] As we shall see later this also implies that the Lamb-shift will be zero in this system.
[7] In a high finesse cavity we can approximate $|r| \simeq 1$.

close to the upper-band-edge[8] for frequency ω_+ and $k \simeq \pi/a$. We can also approximate the Green's function **close to the upper band-edge in the band-gap**:

$$G_{\text{pcw,1D,gap}}(x, x', \omega) \simeq \frac{c}{kv_g} e^{-\kappa|x-x'|} \cos\left(\frac{\pi}{a}x\right) \cos\left(\frac{\pi}{a}x'\right), \tag{3.39}$$

where we have used the decay constant κ defined in the TMM formalism to describe the evanescent fields in the gap. Similarly to the one-dimensional waveguide case, if we want to generalize the one-dimensional Fabry-Perot cavity to a three-dimensional system we have to account for the transverse size of the mode, as is done in [37]. In our work we have focused our attention to two-dimensional photonic crystal slab, where there is a lack of analytical expressions for the Green's function. This is why, in a general case where analytical results are not available, one has to numerically calculate the Green's function, and resort to some techniques to separate it into its eigenmode components. We will come back to this in Chapter 4. For more in depth information refer to Appendix C.

3.2.2 Dipoles coupled to a mode

Now that we have an idea on how the guided modes of the photonic crystals relate to the Green's function, we analyze set of N dipoles coupled to each other through an electric field, as shown in Figure 3.6. The equation of motions for a dipole $\mathbf{p}_i$ at the $\mathbf{r}_i$ position are given by:

$$m\frac{d^2\mathbf{r}_i}{dt^2} + \Gamma' m\frac{d\mathbf{r}_i}{dt} + m\omega_0^2\mathbf{r}_i = q\mathbf{E}(\mathbf{r}, t), \tag{3.40}$$

where m is the mass of the dipole, Γ' is the damping coefficient[9], ω_0 is the resonance frequency and $\mathbf{E}(\mathbf{r}, t)$ is the electric field at the dipole. For simplicity, and in our best interest, we will assume that is electric field corresponds to the guided mode of a photonic crystal[10]. To solve for the case of N dipoles,

[8] The lower band-edge limit can be obtained in a similar fashion by replacing the $\cos(k_+x)$ by $\cos(k_-x)$ as was done in the TMM formalism (see Equation 2.35).

[9] This arises due to the emission into the radiation modes.

[10] If instead we took $\mathbf{E}(\mathbf{r}, t)$ to be the total electric field at the dipole position, we ought not to include the radiation damping Γ' on the left hand side in Equation 3.40 since the damping would naturally arise from the total electric field. Additionally, taking the total electric field would diverge, due to the contribution of the real-part of the Green's function.

we assume a harmonic time evolution and Fourier transform to the frequency domain:

$$(\omega_0^2 - \omega^2 - i\omega\Gamma')\mathbf{p}_i = \frac{q^2}{m}\mathbf{E}(\mathbf{r}_i, \omega)\,, \tag{3.41}$$

where we have taken $\mathbf{p}_i = q\mathbf{r}_i$. Taking into account that $\mathbf{p}_i = \alpha \cdot \mathbf{E}(\mathbf{r}_i, \omega)$ This equation gives the polarizability:

$$\alpha(\omega) = \frac{q^2/m}{(-\omega^2 + \omega_0^2 - i\omega\Gamma')} \simeq \frac{q^2/2\omega m}{(\Delta - i\Gamma'/2)}\,, \tag{3.42}$$

where $\Delta = \omega - \omega_0$ is the detuning. The performed approximation is the classical equivalent of the **Rotating Wave Approximation** (RWA), where we assume a small detuning so that $\omega^2 - \omega_0^2 = (\omega + \omega_0)(\omega - \omega_0) \simeq 2\omega(\omega - \omega_0)$.

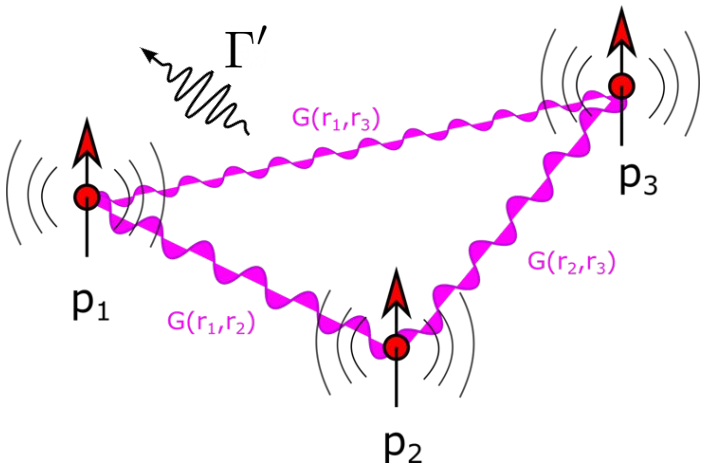

Figure 3.6.: Example of three dipoles $\mathbf{p}_i$ coupled to the electric field, where $i = 1, 2, 3$. These dipoles couple through the Green's function $\mathbf{G}(\mathbf{r}_i, \mathbf{r}_j)$, where $\mathbf{r}_i$ and $\mathbf{r}_j$ correspond the positions of the dipoles and have radiation losses Γ'. Figure courtesy of Jean-Baptiste Béguin [30].

The electric field has contribution of the source field $\mathbf{E}_0(\mathbf{r}, \omega)$ and the field of N dipoles. From Equation 3.18 we know that for N dipoles:

$$\mathbf{E}(\mathbf{r}, \omega) = \mathbf{E}_0(\mathbf{r}, \omega) + \mu_0\omega^2 \sum_{j=1}^{N} \mathbf{G}(\mathbf{r}, \mathbf{r}_j, \omega) \cdot \mathbf{p}_j\,. \tag{3.43}$$

If we substitute this into $\mathbf{p}_i = \alpha\mathbf{E}(\mathbf{r}_i, \omega)$ and assuming all dipoles are orientated in the same direction:

$$\frac{1}{\alpha}p_i - \mu_0\omega^2 \sum_{j=1}^{N} \hat{\mathbf{n}}_p \cdot \mathbf{G}(\mathbf{r}_i, \mathbf{r}_j, \omega) \cdot \hat{\mathbf{n}}_p\, p_j = E_0(\mathbf{r}_i, \omega) \tag{3.44}$$

where $\hat{\mathbf{n}}_p$ is the dipole unit vector, so that $\mathbf{p}_i = p_i \hat{\mathbf{n}}_p$ and $\mathbf{E}_0(\mathbf{r}_i) \cdot \hat{\mathbf{n}}_p = E_0(\mathbf{r}_i)$. Now, we substitute this in Equation 3.42 and multiply by a factor $-q^2/2m\omega$, which yields:

$$(\Delta + i\Gamma'/2)p_i + \mu_0\omega^2 \sum_{j=1}^{N} \hat{\mathbf{n}}_p \cdot \mathbf{G}(\mathbf{r}_i, \mathbf{r}_j, \omega) \cdot \hat{\mathbf{n}}_p \, p_j = -E_0(\mathbf{r}_i, \omega)\frac{q^2}{2m\omega} \,. \tag{3.45}$$

Using the previous expression we can define the **complex coupling rate**:

$$g_{ij} = \frac{\mu_0 q^2 \omega}{2m} \hat{\mathbf{n}}_p \cdot \mathbf{G}(\mathbf{r}_i, \mathbf{r}_j, \omega) \cdot \hat{\mathbf{n}}_p \equiv J_{ij} + i\frac{\Gamma_{ij}}{2} \,. \tag{3.46}$$

It is common practice to separate the real and imaginary part of the coupling rate. The real part corresponds to the **spin-exchange rate** J_{ij}[11] and the imaginary part corresponds to **dissipation rate** Γ_{ij}:

$$J_{ij} = \frac{\mu_0 \omega q^2}{2m} \hat{\mathbf{n}}_p \cdot \mathrm{Re}\{\mathbf{G}(\mathbf{r}_i, \mathbf{r}_j, \omega)\} \cdot \hat{\mathbf{n}}_p \tag{3.47}$$

$$\Gamma_{ij} = \frac{\mu_0 \omega q^2}{m} \hat{\mathbf{n}}_p \cdot \mathrm{Im}\{\mathbf{G}(\mathbf{r}_i, \mathbf{r}_j, \omega)\} \cdot \hat{\mathbf{n}}_p \tag{3.48}$$

Therefore, the system of coupled equations describing N oscillating dipoles can be described in terms of the rates:

$$\left(\Delta + i\frac{\Gamma'}{2}\right) p_i + \sum_{j=1}^{N} \left(J_{ij} + i\frac{\Gamma_{ij}}{2}\right) p_j = -E_0(\mathbf{r}_i, \omega)\frac{q^2}{2m\omega} \,. \tag{3.49}$$

To get a better understanding, let's see what happens in the case when there is **a single dipole** p_1 . The system becomes a single equation:

$$\left(\Delta + i\frac{\Gamma'}{2}\right) p_1 + \left(J_1 + i\frac{\Gamma_{11}}{2}\right) p_1 = -E_0(\mathbf{r}_1, \omega)\frac{q^2}{2m\omega} \,. \tag{3.50}$$

We can understand the equation as a polarizability equation, where the interaction of the dipole with the mode changes its polarizabiliy. This implies that the decay rate is $\Gamma' + \Gamma_{11}$, because of the work done on the dipole by its on field. This is known as **radiative back-action**. The frequency shift J_{11}, also known as **Lamb shift**, is proportional to the electric field parallel to the dipole moment.

[11] The spin-exchange rate is called **Lamb Shift** for $i = j$.

Let's now examine the case of two dipoles that interact through their fields:

$$\begin{pmatrix} \Delta + i\Gamma'/2 + g_{11} & g_{12} \\ g_{21} & \Delta + i\Gamma'/2 + g_{22} \end{pmatrix} \begin{pmatrix} p_1 \\ p_2 \end{pmatrix} = -\frac{q^2}{2m\omega} \begin{pmatrix} E_0(\mathbf{r}_1, \omega) \\ E_0(\mathbf{r}_2, \omega) \end{pmatrix}. \tag{3.51}$$

Due to the reciprocity condition of the Green's function [38] we have the symmetries $g_{12} = g_{21}$, $J_{21} = J_{12}$ and $\Gamma_{12} = \Gamma_{21}$. To solve this system of equations we just need to solve for the eigenvalues and eigenvectors. Assuming that self interactions are the same[12], the eigenvectors and eigenvalues are:

$$\mathbf{p}_\pm = \begin{pmatrix} 1 \\ \pm 1 \end{pmatrix}, \quad \lambda_\pm = \Delta + \mathrm{i}\Gamma'/2 + g_{11} \pm g_{12} \tag{3.52}$$

respectively, which correspond to dipoles in phase and out of phase, as depicted 3.7. Assuming $\Gamma_{12} > 0$, one of the modes has enhanced decay $\Gamma^+ = \Gamma' + \Gamma_{11} + \Gamma_{12}$. Therefore, we call $\mathbf{p}_+$ the **bright mode**. In contrast, the other mode has suppressed decay $\Gamma^+ = \Gamma' + \Gamma_{11} - \Gamma_{12}$ and corresponds to the **dark mode**. In the time domain the eigenmodes are:

$$\mathbf{p}_\pm(t) = p_0 \begin{pmatrix} 1 \\ \pm 1 \end{pmatrix} e^{-(\Gamma' + \Gamma_{11} \pm \Gamma_{12})t} \cos\left[(\omega_0 + J_{11} \pm J_{12})\, t\right]. \tag{3.53}$$

If we examine the situation with initial conditions $p_1(0) = p_0$ and $p_2(0) = 0$, this yields the solution:

$$p_{1,2}(t) = e^{-(\Gamma' + \Gamma_{11} + \Gamma_{22})t} \mathrm{Re}\left\{ \frac{1}{2} e^{\mathrm{i}(\omega_0 + J_{11})t} \left(\pm e^{-iJ_{12}t} + e^{\mathrm{i}J_{12}t} e^{-2J_{22}t} \right) \right\}. \tag{3.54}$$

It is thus possible to analytically calculate the time-evolution of the dipole moment if we know the values of the spin-exchange and dissipation rates in our particular application. For instance, it is possible to calculate and approximate these coefficients for some quasi-one-dimensional structures as shown in [46]. Using the Green's function for the **unstructured waveguide** in

[12] Which means that $g_{11} = g_{22}$.

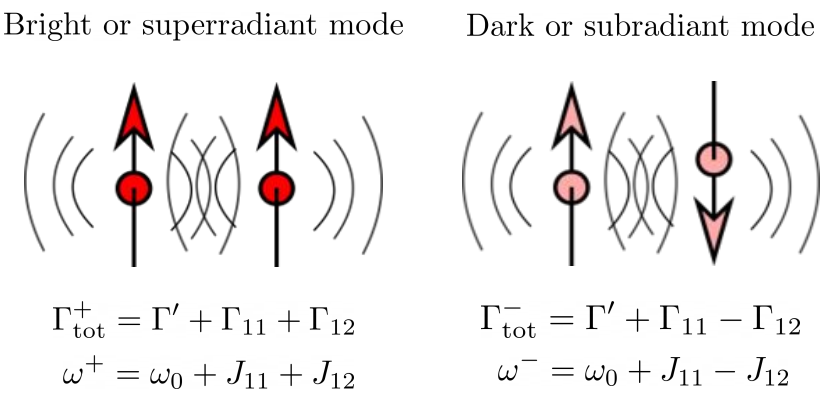

Figure 3.7.: In the case of two coupled dipoles we obtain the bright $\mathbf{p}_+$ and dark $\mathbf{p}_-$ eigenmodes. The bright mode has an enhanced decay rate Γ^+ and higher frequency ω^+, whereas the dark mode has a suppressed decay rate Γ^- and a lower frequency ω^-. Figure adapted from [30].

Equation 3.32 and accounting for the transverse mode size the spin-exchange and decay-rates may be written as:

$$J_{\text{wg},i,j} = -\frac{\Gamma_{\text{1D,wg}}}{2}\sin\left(k|x_i - x_j|\right), \tag{3.55}$$

$$\Gamma_{\text{wg},i,j} = -\frac{\Gamma_{\text{1D,wg}}}{2}\cos\left(k|x_i - x_j|\right), \tag{3.56}$$

where $\Gamma_{\text{1D,wg}} = \frac{1}{2}\Gamma_0 \frac{c}{v_g}\frac{\sigma_0}{A_k}$. As we can see Equation 3.56 is consistent with the expression obtained for Γ_{1D} with the TMM formalism. Interestingly, **the nature of the interaction will be different depending on the distance between the atoms**; for instance, for atoms at a distance $d = n\lambda/2$ where n is an integer, will exhibit a purely dissipative interaction. This is what is shown on the top plot in Figure 3.8. However, if we put the atoms at a distance $d = n\lambda/2 + \lambda/4$ the atom-atom interaction becomes that shown in the bottom plot in Figure 3.8, since there will be a non-zero contribution from the real part of the Green's function. The self-interaction is purely dissipative as before, but now we have $\Gamma_{12} = 0$. This means that there will be spin-exchanges but there will be a a overall decay with a rate $\Gamma' + \Gamma_{11}$.

It is shown in [46] that by calculating the eigenvalues of the Green's function matrix one can calculate the **normalized transmission for N atoms**:

$$\frac{t(\Delta_A)}{t_0(\Delta_A)} = \prod_{k=1}^{N} \frac{\Delta_A + i\Gamma'/2}{\Delta_A + J_{k,\text{1D}} + i(\Gamma' + \Gamma_{k,\text{1D}})/2} \tag{3.57}$$

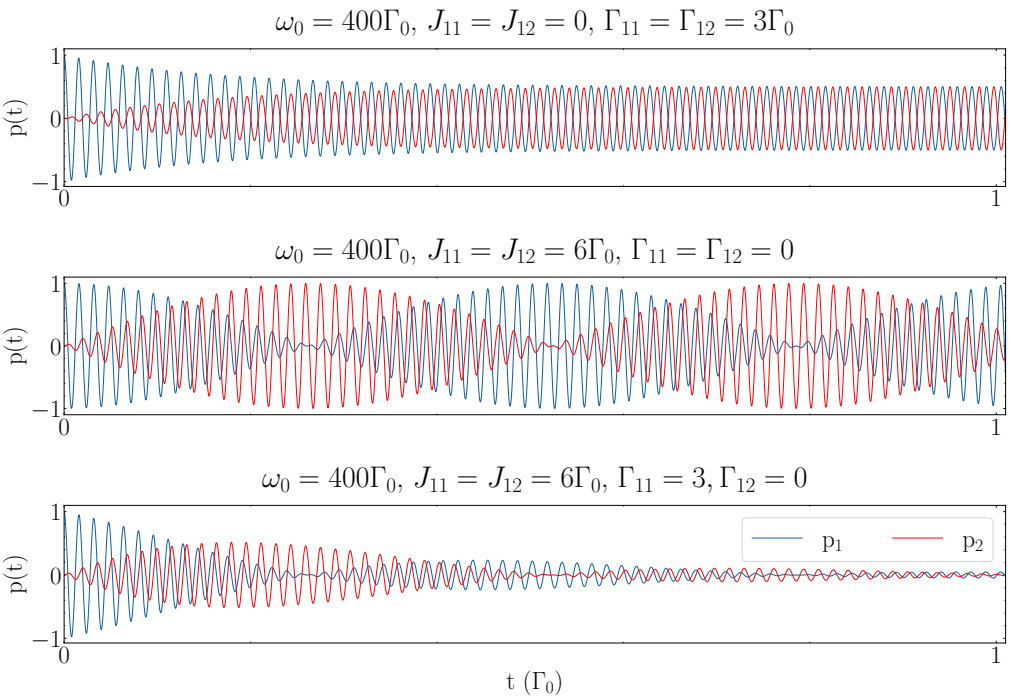

Figure 3.8.: Dynamics of two coupled dipoles. As initial conditions we only have p_1 excited. We plot three cases: on top, the purely dissipative coupling; in the middle, the purely dispersive coupling and on the bottom, the waveguide dispersive coupling. Figure courtesy of Jean-Baptiste Béguin [30].

where $J_{k,1D}$ and $\Gamma_{k,1D}/2$ are the real and imaginary part of the k-th eigenvalue. In Figure 3.9 we show the results for the particular case of one atom with different coupling strengths. In the dissipative regime, when $J = 0$, we see that we obtain a similar transmission profile as the one we got for the single atom in the TMM as in Figure 3.3. In some special cases we will find similar results as the one atom limit; for instance, in case the of N atoms with a spacing $d = n\lambda/2$:

$$\frac{t(\Delta_A)}{t_0(\Delta_A)} = \frac{\Delta_A + i\Gamma'/2}{\Delta_A + i(\Gamma' + N\Gamma_{1D})/2}\,. \tag{3.58}$$

We see that this transmission spectra looks very similar to the one in Equation 3.9, where in this case we have a **superatom** with total decay rate $\Gamma_{tot} = \Gamma' + N\Gamma_{1D,wg}$, corresponding to a bright mode, where the dipoles interfere constructively and enhance emission. In general, we expect to obtain similar results as in Figure 3.9 but where $\Gamma_{1D} \to N\Gamma_{1D}$, which will make the peaks wider and higher. For other configurations expressions become more cumbersome, check [46] for reference.

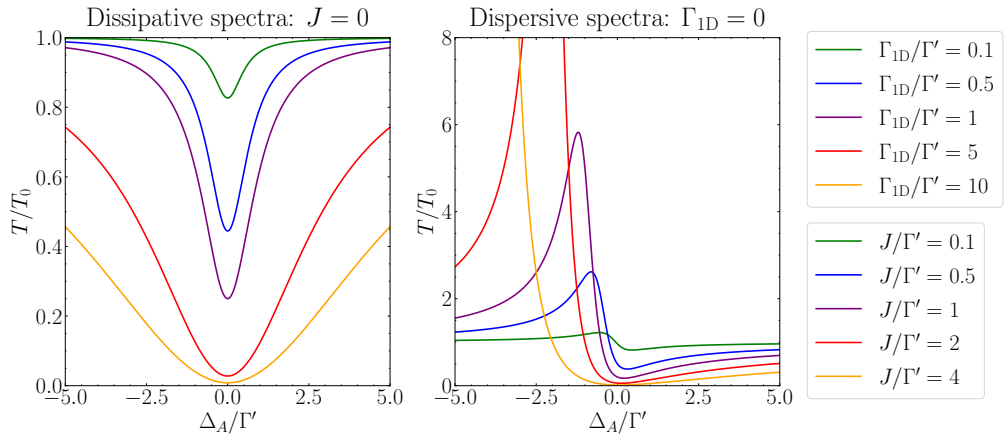

Figure 3.9.: Single atom normalized transmission spectra for the dissipative and dispersive regimes. On the left, dissipative regime ($J = 0$) for different coupling strengths normalized to the emission into radiation modes. On the right, the same for the dispersive regime ($\Gamma_{1D} = 0$).

Next, we can see what happens with the coupling coefficients in the case of **three-dimensional Fabry-Perot cavity**. If one takes into account the transverse size of the mode in the cavity and uses the expression in Equation 3.36 one can calculate the spin-exchange and decay rates [37]:

$$J_{\text{cav},i,j} \simeq -2g^2 \frac{\Delta_c}{\Delta_c^2 + \kappa^2/4} \cos(kx_i)\cos(kx_j) = J_{\text{1D,cav}} \cos(kx_i)\cos(kx_j)\,, \tag{3.59}$$

$$\Gamma_{\text{cav},i,j} \simeq 2g^2 \frac{\kappa}{\Delta_c^2 + \kappa^2/4} \cos(kx_i)\cos(kx_j) = \Gamma_{\text{1D,cav}} \cos(kx_i)\cos(kx_j)\,, \tag{3.60}$$

where $g = \sqrt{|\mathbf{d}|^2\omega/2\varepsilon_0\hbar AL}$ is the atom-cavity coupling rate defined in cavity Quantum Electrodynamics (QED) [47] [1]. Similar to conventional cavity QED it is also possible to define the **quantum cooperativity** as $C = g^2/\kappa\Gamma'$, which weighs the interaction strength with the losses of the system[13]. Interestingly, it has been shown [37] that the atom-cavity coupling rate is related to $\Gamma_{\text{1D,wg}}$ in a general waveguide: $\Gamma_{\text{1D,wg}} = 2Lg^2/v_g$. This means that it is possible to define an analogue to the quantum cooperativity in the dissipative regime $C = \Gamma_{1D}/\Gamma'$ and in the dispersive regime $C = J_{1D}/\Gamma'$, which will be the **main FOMs that we will try to optimize in Chapter 4**.

Using Equation 3.59 wee see that on resonance, when $\Delta_c = 0$, we have purely dissipative interaction, since $J_{\text{cav},i,j} = 0$. In contrast, far away from

[13] In free-space approaches the cooperativity was understood as a measure for the probability of interaction since it was always $C \leq 1$. With the recent developments in cavity QED and nanophotonics $C \gg 1$ has been achieved, and it is used as a parameter to characterize the efficacy of a nanophotonic system.

the resonance, when $\Delta_c \gg \kappa$, we can approximate to have purely dispersive interactions, since $\Gamma_{\text{cav},i,j} \propto 1/\Delta_c^2$. In the most general dispersive waveguide regime we see that the spin-exchange to decay ratio is proportional to the ratio of detuning to linewidth: $J_{\text{cav},i,j}/\Gamma_{\text{cav},i,j} = \Delta_c/\kappa$.

In the Fabry-Perot cavity the normalized transmission can also be calculated using Equation 3.57 [46]:

$$\frac{t(\Delta_A)}{t_0(\Delta_A)} = \frac{\Delta_A + i\Gamma'/2}{\Delta_A + \sum_i^N J_{\text{cav},i,i} + i(\Gamma' + \sum_i^N \Gamma_{\text{cav},i,i})/2}\,. \tag{3.61}$$

In contrast to the transmission for the waveguide, in the cavity there will always be a bright mode, no matter the position or separation between the different atoms. Similar to Dicke superradiance [8], the standing wave of the cavity mode means that there is no propagation phase and the atoms will emit light coherently. As we show in Figure 3.10 the transmission spectrum becomes symmetric for the dissipative coupling regime, when $\Delta_C = 0$.

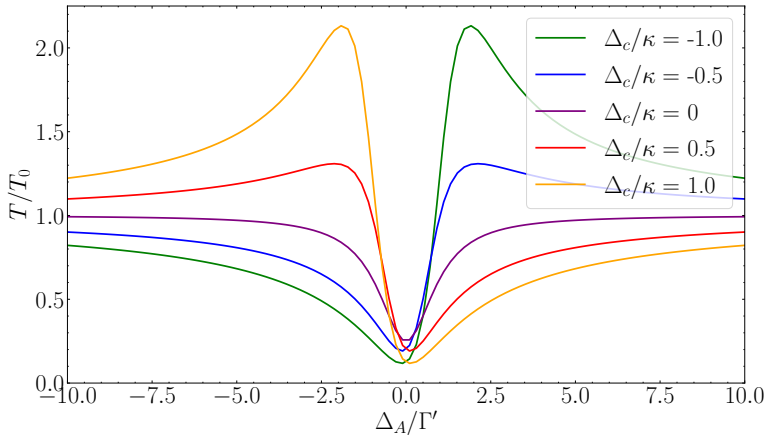

Figure 3.10.: Normalized transmission spectra for different atom detunings Δ_A with an atom at the antinode of the cavity mode. We have chosen $\Gamma_{\text{1D,cav}} = \Gamma'$ as in [37].

The last example of Green's function we studied in the previous section was the one-dimensional photonic crystal waveguide. For this structure it is possible to to approximate the spin-exchange and decay-rates **close to the band-edge** using the Green's function calculated previously in Equation 3.38:

$$J_{\text{pcw},i,j} \simeq -\frac{\Gamma_{\text{1D,pcw}}}{2} \sin\left(\left(k - \frac{\pi}{a}\right)|x_i - x_j|\right)) \cos\left(\frac{\pi}{a}x_i\right) \cos\left(\frac{\pi}{a}x_j\right), \tag{3.62}$$

$$\Gamma_{\text{pcw},i,j} \simeq \Gamma_{\text{1D,pcw}} \cos\left(\left(k - \frac{\pi}{a}\right)|x_i - x_j|\right) \cos\left(\frac{\pi}{a}x_i\right) \cos\left(\frac{\pi}{a}x_j\right), \tag{3.63}$$

where $\Gamma_{\text{1D,pcw}} = \Gamma_0 \frac{\sigma_0 c}{A_k v_g}$. We see that close to the band-gap $k \simeq \pi/a$ and therefore $J_{\text{pcw},i,j} \simeq 0$. This means that in the case of the one-dimensional photonic crystal **when the atom separation fulfills** $d \ll 2\pi/(k - \pi/a)$ **we expect just dissipative interactions** where:

$$\Gamma_{\text{pcw},i,j} \simeq \Gamma_{\text{1D,pcw}} \cos\left(\frac{\pi}{a} x_i\right) \cos\left(\frac{\pi}{a} x_j\right). \tag{3.64}$$

In this particular case, the Green's matrix becomes separable and consists of a bright mode and $N - 1$ dark modes [46]. For the bright mode, one can calculate the normalized transmission using Equation 3.57:

$$\frac{t(\Delta_A)}{t_0(\Delta_A)} = \frac{\Delta_A + i\Gamma'/2}{\Delta_A + i(\Gamma' + \Gamma_{\text{1D,pcw}} \sum_j \cos\left(\frac{\pi}{a} x_j\right))/2}. \tag{3.65}$$

Once more, we observe superradiant behavior in this case. However, in this case, the Bloch mode will be a standing wave near the band edge which leads to atoms in different positions to couple with the same phase, similar to the result we found for the Fabry-Perot cavity in Equation 3.61[14].

Finally it is worth mentioning that **in the band-gap of the photonic crystal** one obtains different couplings. Using the Green's function in the band-gap one can calculate that:

$$J_{\text{pcw},i,j} \simeq \frac{\Gamma_{\text{1D,pcw}}}{2} e^{-\kappa|x_i - x_j|} \cos\left(\frac{\pi}{a} x_i\right) \cos\left(\frac{\pi}{a} x_j\right), \tag{3.66}$$

$$\Gamma_{\text{pcw},i,j} = 0, \tag{3.67}$$

where κ is the decay constant for the evanescent fields in the gap. This means that the atom-atom dynamics in the band-gap will be **completely dispersive**, similar to what we obtained in the Fabry-Perot cavity far from resonance. As we will see in Chapter 4 this can be used to implement a **quantum simulation platform**.

For a complete description on how expand the Green's function formalism to account for a quantum description of light and matter please check the notes in Appendix D, where we show that the quantum coupling-rates are equivalent to the one calculated in this chapter.

[14] The drawback of cavity systems is that it is difficult to scale the system up since in cavities $\Gamma_{1D,cav} \propto 1/V_k$ [37]. In contrast, the photonic crystal gives an advantage because $\Gamma_{1D,pcw} \propto 1/v_g$, which is independent of system size.

4 Engineering interactions

"Eta jo naute baina ez naute menperatu.
Hotzetik epelera noan hontan.
Zugatik egingo dut azkenengo jauzi hau.
Alienatu ezin nazazuen."
— Unidad Alavesa*, Jo naute.*

In this chapter we will focus on making use of the available numerical methods to solve Maxwell's equations, as presented in Appendix C, to accurately describe the many exciting physics that arise when atoms are coupled to photonic crystal waveguides.

Using the knowledge acquired in previous chapters we simulate the coupling of an atom to photonic crystal structures using the Green's function formalism. For three different state-of-the art photonic crystal structures [48][12] we will numerically study:

- The **dispersion properties of the infinite structures**, which can be engineered for trapping atoms, making them emit light in preferred directions or enabling dispersive atom-atom interactions in band-gap regime.
- The resilience of the structures to **fabrication imperfections** and experimental constraints.
- A systematic computational approach to calculate the emission properties of atoms close to finite structures based on FDTD methods.
- The accuracy of the numerical methods with special detail to the convergence of the results.
- The possibility of improving the atom-photon and atom-atom cooperativities $\Gamma_{1D/2D}/\Gamma'$ and J/Γ', in different frequency regimes by modifying the design parameters of the structures.

Note on the material properties of the structures

All the structures that we will present in the following sections consist of **silicon nitride (Si_3N_4)** two-dimensional photonic crystal structures, as the one we introduced in Figure 1.2b. We use silicon nitride[1] mainly because of its **low optical loss** in the frequency range of Cs[2] transitions. For instance, in [50] they find an absorption length[3] characterized by $\mathrm{Im}\{n\} \leq 10^{-7}$ for 850 nm, whereas in [50] they find $\mathrm{Im}\{n\} \leq 10^{-5}$ for 935 nm. It is important to note that this number is subject to surface roughness, fabrication imperfections and measurement accuracy, but in the past in QUANTOP $\mathrm{Im}\{n\} \simeq 10^{-6}$ has been assumed. Additionally, there is a great deal of **available documentation for fabrication techniques** compatible with Si and silicon nitride has demonstrated to have **excellent mechanical properties**.

4.1 Double nanobeam waveguide

The double nanobeam structure developed by Hung et al. in [48] is a simple photonic crystal waveguide. In their paper their authors mainly investigate how it is possible to trap atoms close to the structure while achieving a strong light-atom coupling. We have used it to learn how we can describe photonic crystal structures numerically through electromagnetic simulation methods.

4.1.1 Dispersion properties: Trapping

Based on the structure in Figure 4.1 we first investigate what we expect from the behavior of the infinite system. In Figure 4.2 we show the band structure where we plot the modes with even symmetry in Z. For the calculated dispersion diagram, the D_1 line of Cs[4] is closely aligned to the edge of the Brillouin zone. As we saw in Chapter 3 this means that since the bands are flat at the band edge, the light will have low group velocity and therefore, we expect enhanced atom-light coupling.

[1] Stoichiometric Si_3N_4 made with Low-Pressure Chemical-Vapor-Deposition (LPCVD) [49].
[2] For more information on why we use Cs atoms please refer to Appendix A.
[3] For Si_3N_4 the absorption length is 0.73 m at $\lambda = 850$ nm. Therefore, in our distance regime we expect negligible absorption processes, since the absorption length is much larger. For comparison in a conventional SiO_2 fiber the absorption length is 10 km at λ=1 μm.
[4] For more information on the relevant transition frequencies of Cs please check Appendix A.

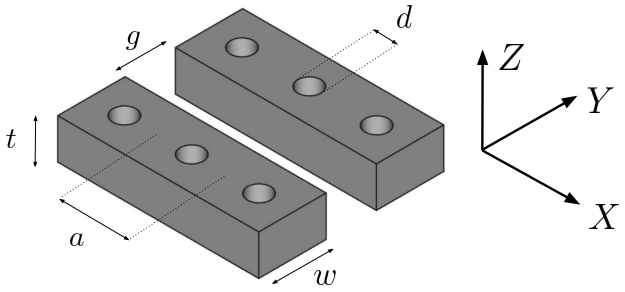

Figure 4.1.: 3 unit cells of the double nanobeam structure with lattice constant a. The structure is characterized by design parameters: $(a, w, t, d, g) = (335, 335, 200, 116, 250)$ nm.

Moreover, it is fundamental to understand where we position the atoms in the structure for stronger interaction. As a matter of fact, we will be looking to position the atoms in zones where the concentration of the modal field is biggest, as we learnt in Equation 3.8. Following the intensity pattern of the lowest band's eigenmode in Figure 4.2 we see that it is possible to put the atoms between the two nanobeams, at the mid-distance between two contiguous holes, where the modes of both nanobeams hybridize and produce local saddle points, which should result in a fairly high interaction strength [48].

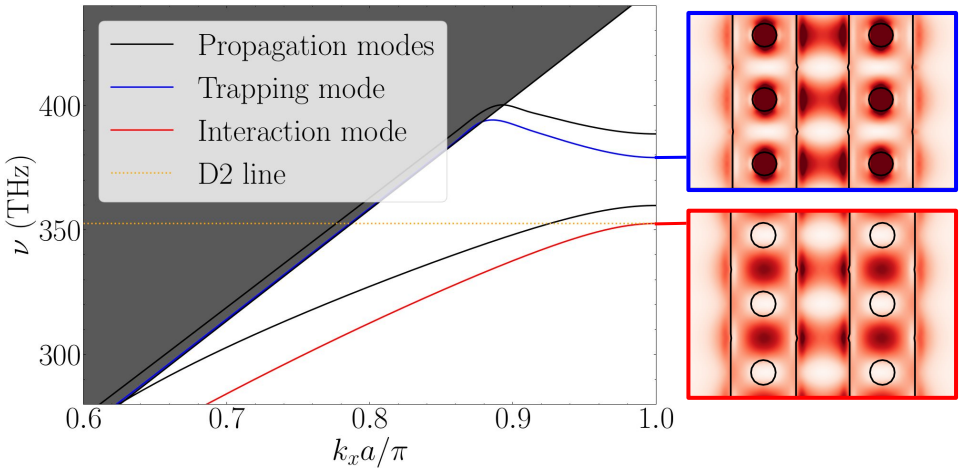

Figure 4.2.: Band diagram for the Z even modes in the double nanobeam structure. In blue we have the mode and mode intensity profile related to the trapping mode. In red we have the mode and mode intensity profile for the mode used for enhanced atom-light interaction.

At the same time, it is possible to trap the atoms at the intensity minimum of the trapping mode[5] using the trapping mode (blue) in Figure 4.2 as a blue-detuned **far-off resonance dipole-force trap** (FORT) at the magic wavelength $\lambda_T = 793$ nm [51]. This trapping scheme presents a major advantage compared to free-space approaches since it is possible to have two modes with different frequency for the same k[6], which is hard in free-space. For more information on the trapping, please refer to [48], where the authors also take into account the Casimir-Polder forces that we mention in Equation B.6, to create a stable atom-trap in the double nanobeam structure.

4.1.2 Convergence of FDTD calculations for one-dimensional photonic crystals

Now that we know that we satisfy the conditions for strong atom-photon coupling, we shall have a look at the emission of the atom. Hence, we now consider a finite structure[7] and run a FDTD calculation as explained in Appendix C. It is critical to make sure that FDTD results are sensible and do not vary too much with our choice of simulation parameters. Therefore, we run a **convergence test**.

It is extremely complicated to define a convergence method that works all the time, but since the first want to understand the spontaneous emission of the atoms we will converge the PF, as introduced in Equation 3.29. After careful trial and error we verify that there are 3[8] main simulation parameters that will affect the results: **the mesh accuracy, the simulation time and the frequency sampling**. The mesh accuracy describes how finely we discretize our simulation volume; in other words, our spatial resolution. The simulation time represents how long we run our simulation, which has a direct impact on the frequency resolution. Lastly, the frequency sampling refers to how many equally spaced frequency points we evaluate in our spectra. For more information on these simulation parameters and more please refer to Appendix C.

[5] Which is in the same position as the maximum for the interaction mode.
[6] And therefore with similar spatial variations.
[7] Similar to [48] we consider a 81 unit-cell waveguide.
[8] The thickness of the PML boundary conditions should also affect the results but after careful checks we make sure that using Lumerical's default thickness yields stable and accurate results. For reference on these boundary conditions check Appendix C.

To run any convergence test one conventionally defines a **cost function** that is converged by gradually varying the simulation parameters. Since we have to change the frequency sampling, or the number of frequency points, in each iteration it is particularly difficult to define a cost function that addresses the frequency points individually. Accordingly, we have decided to converge the numerical integral of the Purcell factor. This involves defining the **absolute residual** cost function as:

$$\Delta \mathrm{PF}_k = \Delta f \left| \sum_i^{\mathrm{N_{freq,k}}} \mathrm{PF}_i - \sum_j^{\mathrm{N_{freq,k-1}}} \mathrm{PF}_j \right|, \tag{4.1}$$

where k corresponds to the number of iteration in the convergence procedure, N_{freq} corresponds to the frequency sampling and Δf corresponds to the equal frequency spacing in our spectra. It is also possible to calculate the **relative residual**, where we just calculate the relative variation to the current integral value: $\delta \mathrm{PF} = \Delta \mathrm{PF} / \sum_i^{\mathrm{N_{freq,k}}} \mathrm{PF}_i$.

Once we have defined this cost function we run for the convergence test and gather all the results in Table 4.1. As is also depicted in Figure 4.4, when we increase the accuracy of the simulation the residual fluctuates around a plateau of values. However, the real time it takes to compute these simulations increases drastically when we increase the mesh accuracy. That is why we decided to move forward in our simulations with the parameters in the **fourth iteration**, where we expect our results to be around a 2% **relative error**, but where our simulations still take less than an hour to run.

Iteration	Mesh accuracy	Time factor	Fr sampling	Abs. residual	Rel. residual	Time [hh:mm:ss]
1	1	100	100	-	-	00:02:27
2	1	150	200	$3.56 \cdot 10^{-3}$	$4.14 \cdot 10^{-3}$	00:03:36
3	2	200	300	$8.15 \cdot 10^{-3}$	$9.59 \cdot 10^{-3}$	00:31:25
4	**2**	**250**	**400**	$\mathbf{2.03 \cdot 10^{-2}}$	$\mathbf{2.33 \cdot 10^{-2}}$	**00:42:58**
5	2	300	500	$1.76 \cdot 10^{-2}$	$2.06 \cdot 10^{-2}$	00:56:00
6	3	350	600	$1.52 \cdot 10^{-3}$	$1.78 \cdot 10^{-3}$	05:25:59
7	3	400	700	$1.25 \cdot 10^{-2}$	$1.44 \cdot 10^{-2}$	05:59:04

Table 4.1.: PF converge scheme results for the double nanobeam structure. We vary the simulation parameters to see the convergence of the residual for the PF. We **highlight** the iteration that gives converged enough results in useful computation time.

Next in this analysis is to **calculate how much of this emission goes into the guided modes of the structure**. As we defined in Chapter 3 it is possible to separate the total decay rate into its guided mode and radiation contributions: $\Gamma_{\text{tot}} = \Gamma_{1\text{D}} + \Gamma'$. This means that if we are able to calculate the emission into the radiation modes we can also deduce the emission into the guided modes.

Surprisingly, in the reference [48] we see that it is assumed that $\Gamma' \simeq \Gamma_0$. This is however an incomplete approach to the analysis of the system, since the emission into radiation modes will depend on many variables. This is why, inspired in the approach used in [52] we use **the box method** to calculate the emission into radiation modes by calculating the energy that flows through a box. As shown in Figure 4.3 in red, we create a box of dimensions (w, t, L) in our FDTD simulation and by measuring the power flowing through the faces of the box we can determine Γ'.

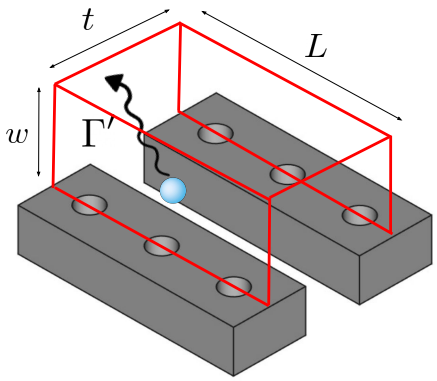

Figure 4.3.: Numerical approach to measure the emission into radiation modes Γ' for the double nanobeam structure with an atom (in blue). Results are converged increasing the size of the dimensions (w, t, L).

Again it is necessary to run a **convergence test**, since we want to be systematically sure that we capture all the energy emitted into the radiation modes without being exposed to evanescent fields close to the photonic crystal.

Fortunately, with the box method is it much more straightforward to define an adequate cost function. Since we have already run the previous convergence test we have already established how many frequency points we want to sample from our spectra in the FDTD simulation. This means that we can now define a **cost function that addresses each frequency point individually**.

Iteration	Width [a units]	Length [a units]	Thickness [a units]	Abs. residual	Rel. residual
1	0.5	5	0.25	-	-
2	1	10	0.5	$5.54 \cdot 10^{-2}$	$6.80 \cdot 10^{-2}$
3	2	20	1	$3.86 \cdot 10^{-2}$	$4.97 \cdot 10^{-2}$
4	4	30	2	$1.62 \cdot 10^{-2}$	$2.10 \cdot 10^{-2}$
5	8	40	4	$9.51 \cdot 10^{-3}$	$1.23 \cdot 10^{-2}$

Table 4.2.: Box method converge scheme results. We vary the size (w, L, t) of the box in Figure 4.14 to see the stability of the results for calculating Γ'.

Thus, we define the **absolute residual** cost function as the mean deviation for each point:

$$\frac{\Delta\Gamma'_k}{\Gamma_0} = \frac{|\overline{\Gamma'_k - \Gamma'_{k-1}}|}{\Gamma_0} \tag{4.2}$$

where k is the iteration of the convergence procedure. Similar to the previous convergence procedure we also define the **relative residual** as: $\delta\Gamma'_k/\Gamma_0 = (\Delta\Gamma'_k/\Gamma_0)/(\Gamma'_k/\Gamma_0)$.

To summarize, as shown in Figure 4.4, to calculate the FOMs in our system we have to run two convergence tests that should give us an estimate of the error we will have in our results. The results obtained for the box convergence method have also been gathered in Table 4.2. We see that as we increase the size of the box we capture more and more accurately the emission into the radiation modes without diverging towards evanescent field of the photonic crystal.

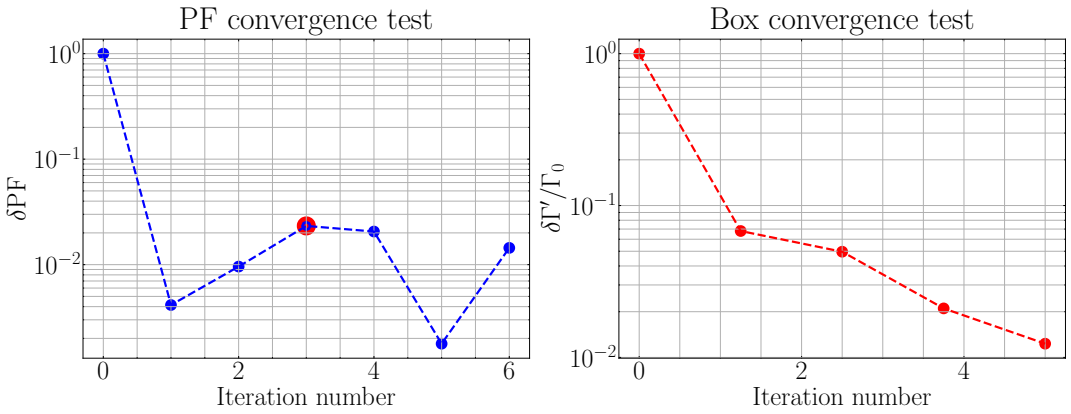

Figure 4.4.: Convergence test for the double nanobeam waveguide. On the left, relative residual δPF as a function of iteration for the PF convergence test. On the right, relative residual $\delta\Gamma'/\Gamma_0$ obtained with the box method.

4.1.3 Emission properties and cooperativity

Having determined an approximate error on our results, we can confidently calculate the FOMs of the system.

In Figure 4.5 we calculate the **spontaneous emission** rate of the atoms in the structure, by means of the PF. Similar to [48] we find that for a dipole polarized in the Y direction we mainly couple with the interaction band in Figure 4.2, while when the dipole is polarized in the X direction we couples more weakly with the trapping mode. This happens due to the weaker intensity Bloch mode at the atomic position, as we saw in the TMM formalism with 3.8.

Since the double nanobeam has a finite size the spectra show the **band-edge resonances** introduced in Section 2.3.1. As expected, these resonances become narrower as one approaches the band-edge. That is why for this simulation we have had to increase the frequency sampling, in order to be able to resolve the resonances better. As a matter of fact, for the broadband response we are not able to completely resolve the spectra, so on the left in Figure 4.5 we plot a short-impulse response close to the band edge, where we can discern the last local maxima completely resolved.

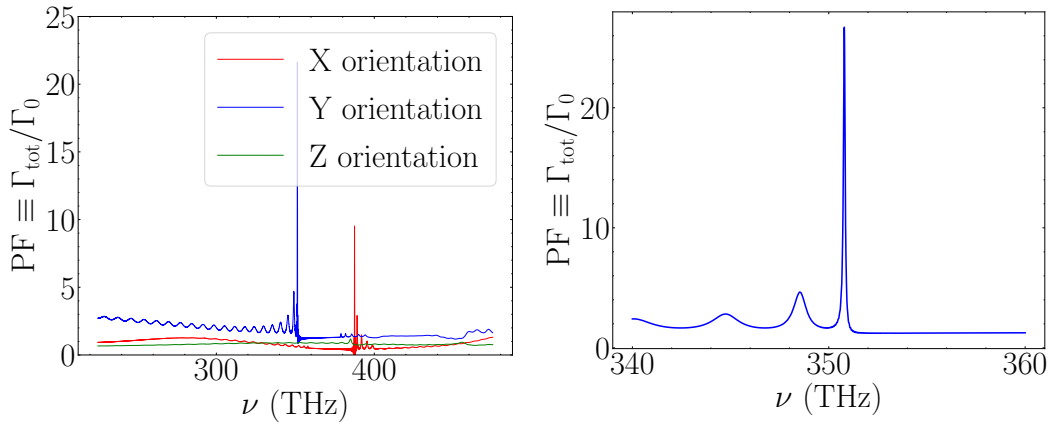

(a) PF for dipole orientations.

(b) Zoom on band-edge for Y orientation.

Figure 4.5.: PF for a dipole polarized along the cartesian axes in a 81 unit cell double nanobeam structure. On the left, broadband response and on the right, higher frequency resolution plot for a Y polarized dipole close to the band-edge frequency.

In Figure 4.6a we calculate the emission into the radiation modes of the system with the box method, where it is evident that the assumption that $\Gamma'(\nu) = \Gamma_0$ used in [48] is incorrect, since our calculation of Γ'/Γ_0 shows that we have both a strong **frequency and dipole polarization dependence**. As we commented in Section 3.1 we see that the photonic crystals allow for incredible leap in cooperativity in the range $10 < \Gamma_{1D}/\Gamma' \leq 20$, 2 orders of magnitude higher than the one in the fiber experiment at QUANTOP where the cooperativity was in the range $0.05 < \gamma_{1D}/\Gamma' < 0.1$.

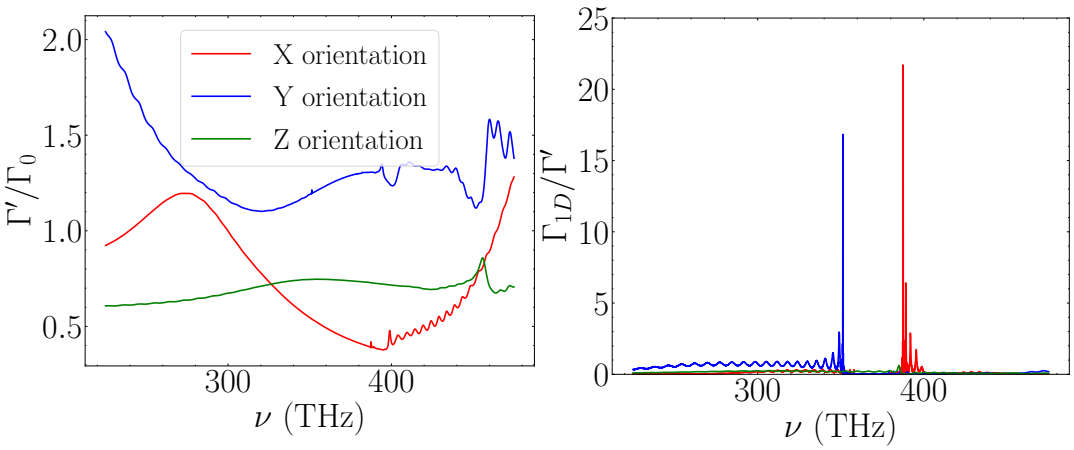

(a) Emission into radiation modes.

(b) Single atom quantum cooperativity.

Figure 4.6.: Spectra of the the FOMs calculated after convergence of the box method for the double nanobeam structure. In **(a)** we show the spectra for different dipole orientations of the power flowing through the box faces. In **(b)** we calculate the single-atom quantum cooperativity spectra using the results in **(a)**.

Interestingly, we note that for the X orientation of the dipole at some frequencies the emission into radiation modes halves the emission into free-space, which means that for certain parameters it is possible inhibit the losses of the system. This probably happens because the field pattern emitted by the dipole does not overlap as strongly with the radiation mode profile as the rest.

Using the result for the emission into the radiation modes in Figure 4.6b we compute the single atom dissipative quantum cooperativity as introduced in Section 3.2.2 when we studied atoms coupled to a Fabry-Perot cavity mode. Interestingly, for the X orientation the cooperativity is enhanced due the previously mentioned suppression of Γ'. This is substantial because it tells us that **it may be possible to engineer a structure to further suppress the emission into these modes and enhance the emission into the guided modes relative to free-space emission**.

4.2 Square lattice photonic crystal slab

In this section we move towards structures that we are most interested in and that are currently being fabricated in the lab, such as the square lattice photonic crystal slab shown in Figure 4.7. We follow the same design parameters[9] as Yu et al. in [12] in order to understand some of the interesting physics that can arise in this configuration.

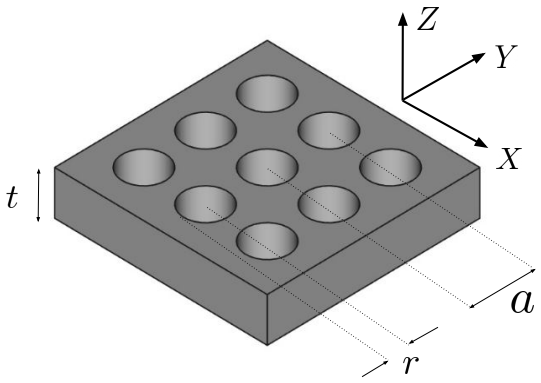

Figure 4.7.: Square lattice structure for three unit cells with design parameters: $(a, t, r) = (290, 200, 103)$ nm, where a is the lattice constant, t is the membrane thickness and r is the hole radius.

4.2.1 Dispersion properties: directional emission

In Figure 4.8a we show the band diagram related to the infinite structure photonic crystal slab. With this particular geometry, the Cs D_2 line lies on top of dielectric TE mode of the structure at the X point. In this high symmetry point the dielectric mode becomes very flat, allowing for very low group-velocities, and thus, for the possibility of strong light-atom interaction in the dispersive waveguide regime.

Another important advantage of this platform is that it allows for **directional emission**, which means that the atom will emit the photons in a preferred direction due to the dispersion properties of the photonic crystal. In Figure 4.8b we plot a two-dimensional version of the band-diagram, known as the **isofrequency diagram**. For a particular frequency, around $\nu = 390$ THz, the isofrequency curves become almost flat, which means that the group velocity's

[9] As we will see, the geometry was chosen to allow both Cs D_1 and D_2 lines to couple to a TE-like guided mode [12].

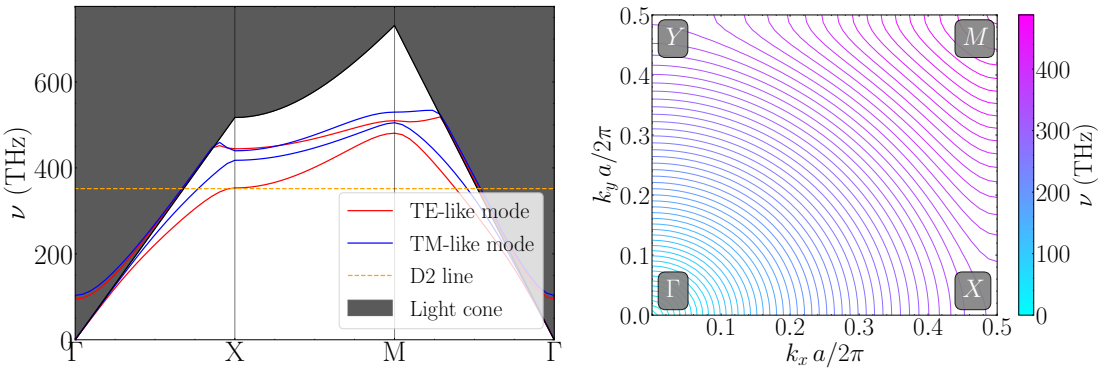

(a) Band diagram.

(b) Isofrequency diagram.

Figure 4.8.: Band diagrams for the square lattice photonic crystal slab. (a) Ordinary band diagram going through the edges of the Brillouin zone. (b) Isofrequency diagram where we plot the positive part of the first Brillouin zone.

direction is the same for many different wave-vector combinations[10]. This is known as a **self-collimation effect** that results in directional emission [53] [12] [32][54].

In Figure 4.9 we show this directional emission effect for different frequencies as done in [12][11]. For a dipole polarized in the Y direction and for $\nu = 320$ THz we find that there is no directional emission effect, as should be expected by checking the isofrequency diagram. As a matter of fact, we obtain the free-space dipole emission pattern that arises from the fields in Figure 3.4. If we increase the frequency up to $\nu = 390$ THz, we find that a Y polarized dipole emits in the M direction. Since we have a Y polarized dipole, we see how the radiation couples in an X-like pattern, due to the projection of the fields into the directions symmetric to M. Therefore, we try with a diagonally polarized dipole, so that we see how the emission only gets projected onto the parallel M direction.

In [12] the authors explain how it is possible to adjust the lattice constant to $a = 330$ nm to align the Cs D_2 line to the flat dispersion region. This would allow us to **create lattices of atoms connected through the guided modes**

[10] To understand this better, let's remember that when the atom emits in a frequency that corresponds to the linear regime of isofrequency curves, the group velocity $\mathbf{v_g} = \nabla_{\mathbf{k}}\omega$ will point in the same direction perpendicular to the band, for most (k_x, k_y) pairs, which in this case leads to the light field being directed in the M direction.

[11] Our results have also been obtained through a FDTD calculation using MEEP [55]. In this case we have not executed our usual convergence scheme procedure because we only wanted to include qualitative results that do, in principle, not require much numerical accuracy.

of the structure allowing for atom-atom interactions in the waveguide dispersive coupling regime[12] as shown in Figure 3.8.

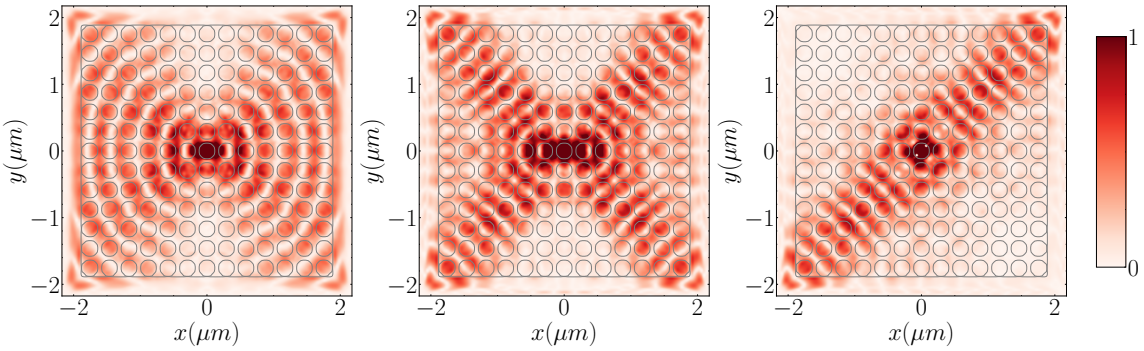

Figure 4.9.: Directional emission effects in the square lattice photonic crystal slab. On the left, a Y polarized dipole emits at $\nu = 320$ THz, where the radiation is nearly isotropic. In the middle, at $\nu = 390$ THz the Y polarized dipole emits along all projected M directions following the crystal symmetry, due to the self-collimation effect. On the right, the dipole is polarized along the $\hat{\mathbf{r}} = -\hat{\mathbf{x}} + \hat{\mathbf{y}}$ direction and so it only projects onto a single M direction.

4.2.2 Tolerances and tuning rates

The real photonic crystal slabs that are fabricated will be characterized and compared to the idealized results in the previous section are far from perfect. As a matter of fact, in Figure 4.10 we show a SEM image of cross section of a real photonic crystal slab[13] fabricated in the cleanroom.

One of the main **fabrication constraint** that arises in the when doing e-beam lithography, as shown in Figure 4.10 is that the holes in the structure are slightly slanted; in other words, their radius gets smaller as one goes down the hole. We would like to see how this affects our previous results of the idealized structure, to check for the robustness of the chip to fabrication imperfections. Using Figure 4.10 one can conclude that for this particular sample the sidewall angle is around $7.9°$, so we use this angle as a reference to understand the impact of this fabrication defect.

[12] We have carefully checked that we have non-zero contributions from both the real and imaginary parts of the Green's function in the plane.

[13] Note that this is not a square lattice of circular holes, but the hexagonal hole lattice that will be introduced in the next section. We use this image for illustration purposes.

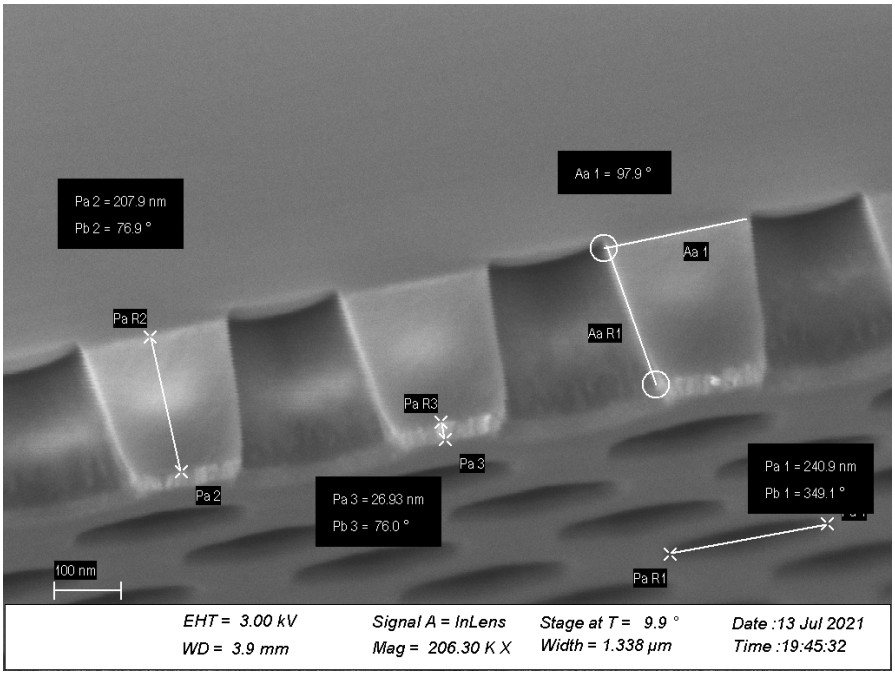

Figure 4.10.: SEM image of the cross section of a photonic crystal slab fabricated in the cleanroom. The sidewalls of the holes in the crystal have an angle of $7.9°$ due to the imperfect fabrication procedure. Figure courtesy of Anders Simonsen [30].

To examine the impact of the fabrication imperfection we calculate the frequency shift of the TE dielectric band at the X point[14]. In Figure 4.11a we show there is a non-negligible frequency decrease for the dielectric and air bands regardless of polarization.

After further inspection we have studied this shift more quantitatively by varying the slope angle, as shown in Figure 4.11b. There seems to be a quasi-linear dependence of the frequency shift with slope angle. We try a linear fit of the type $\Delta\nu = A\alpha + B$, and retrieve the coefficients $A = 1.13$ THz $/\,°$ and $B = 0.35$ THz. Since B should be zero there are two possibilities: either we have to add a systematic uncertainty to our calculations to justify our error in the parameter, or we have to try a more complex fit. Since we do not have any a priori knowledge of the uncertainties we try to fit the data to a custom fit of the type $\Delta\nu = A\sin(Bx + C) + Dx + E$. We will not add the fitted coefficients here since they are mostly irrelevant, but in Figure 4.11b we see that this fits the data much better.

[14] Due to time constraint we were only able to study the effect of the slanted walls in the infinite structure; nonetheless, we also expect to see a non-negligible effect on the finite structure atom-coupling rates calculated through FDTD calculations.

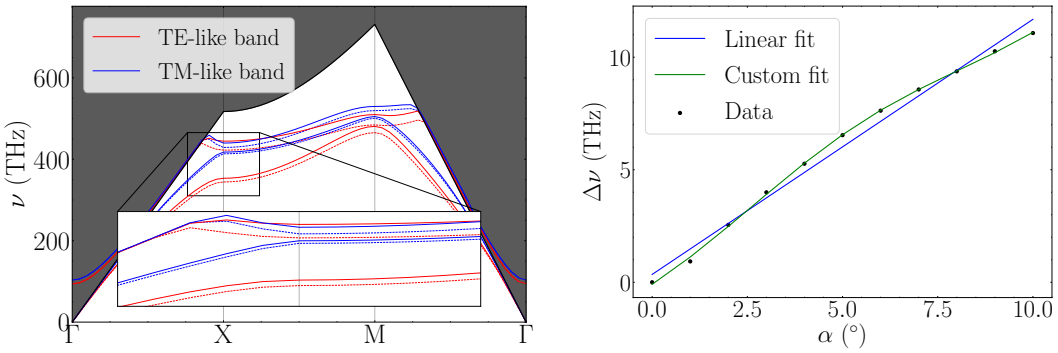

(a) Band structure accounting slopes. **(b)** Frequency shift for different slopes.

Figure 4.11.: Effect of the sidewall slope on the photonic crystal band structure. **(a)** The perfect structure modes (normal line) are pulled in frequency to imperfect modes (dashed line). **(b)** Frequency difference for the TE dielectric band at the X point for different slope angles α. We also add two fits from a linear and custom model.

4.3 Hexagonal lattice photonic crystal slab

In this section we switch to another photonic crystal slab with a different geometry. As we can see in Figure 4.12a, we will study an hexagonal lattice photonic crystal slab with hexagonal holes as designed by Yu et al. in [12][15]. This structure is particularly interesting because one can employ it to **exploit coherent atom-atom dynamics mediated by photons in the band-gap regime while also allowing for slow-group velocities at the K point, resulting in strong atom-light interaction**.

4.3.1 Dispersion properties: TE band-gap

In Figure 4.3 we calculate the band diagram of the infinite crystal slab where we display the dielectric and air bands for both TE and TM polarizations. For this particular geometry we have a TE band gap which covers the D_1 and D_2 transitions of Cs. This means that when we place an the atom in a hole, **we will excite the band-gap modes**, which are evanescent in the photonic crystal plane. Additionally, we also observe that the TE dielectric band is quite flat at the K point, which may be used to enhance the strength of the interaction.

[15] This geometry has been proven to be the optimal geometric design for maximizing the TE band-gap width using Topology Optimization techniques [56].

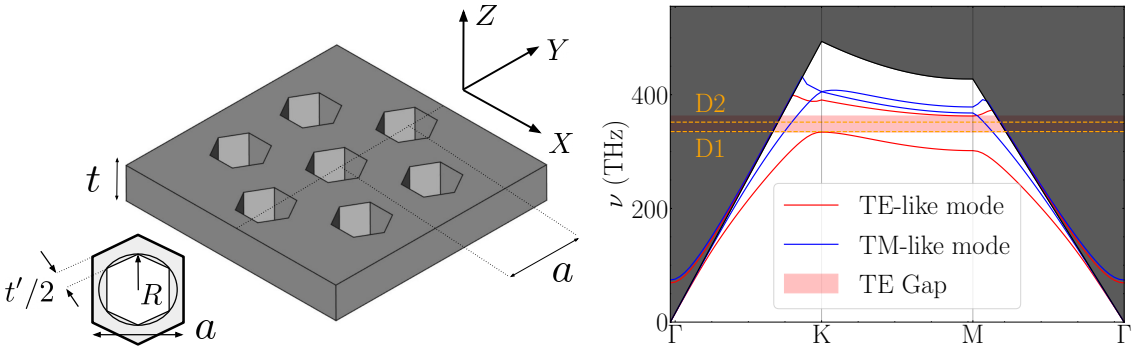

(a) Hexagonal lattice slab. **(b)** Band diagram.

Figure 4.12.: Structure and band diagram for the hexagonal photonic crystal slab. **(a)** 2 unit cells of a photonic crystal slab with design parameters $(a, t, t') = (405, 200, 180)$ nm, where a is the lattice constant, t is the thickness and t' corresponds to a tether length. It is possible to relate t' and a with the radius of the radius R of the circumscribed circle. **(b)** Band diagram of the structure with the TE and TM-like dielectric and air bands.

4.3.2 Convergence of FDTD calculations for a two-dimensional photonic crystal

Similar to the double nanobeam waveguide we will consider a finite photonic crystal slab which corresponds to the structure shown in Figure 4.13. We have a slab of Si_3N_4 where we have punched 314 hexagonal holes in an hexagonal supercell[16], similar to what is done in [12]. Since the number of holes in the X and Y directions will be different we expect to see different slightly different band-edge resonances and supermode modulation in the results that will follow.

Using this finite structure we will once again make sure that the results arising from our FDTD calculations are converged and within acceptable error ranges. That is why we proceed with a similar **convergence scheme** as the one developed to study the double nanobeam structure, which will this time be adapted to the two-dimensional case.

First, we converge the **PF calculation** similar to what we did in the one-dimensional case. The main results are summarized in Table 4.3 and plotted on the left plot in Figure 4.14. We check that as we increase the number of iterations the residual goes down. We have then selected the results that refer

[16] We leave some homogeneous dielectric between the holes close to the boundaries of the structure to avoid FDTD simulation errors.

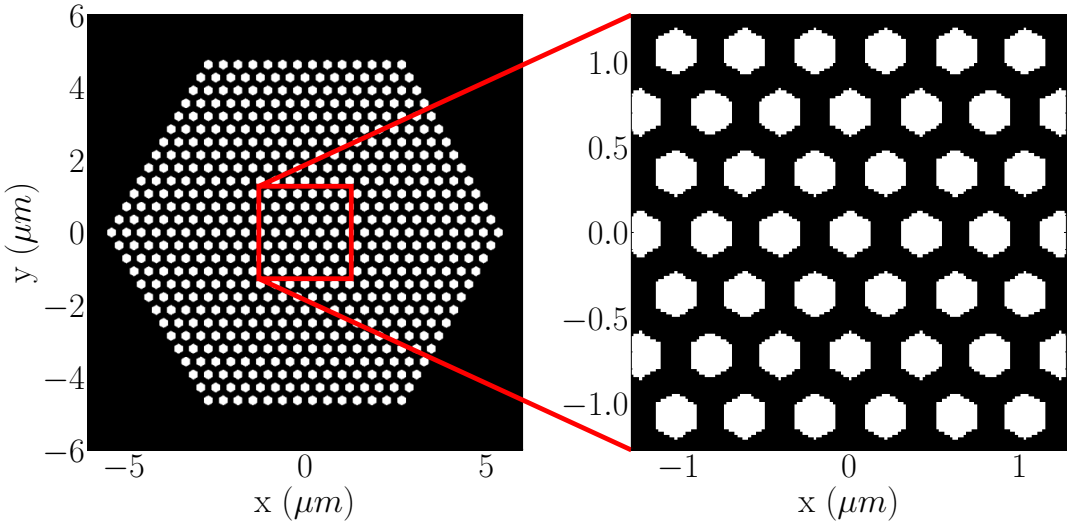

Figure 4.13.: Index profile of the photonic crystal slab structure for $z = 0$. In black we have SiN and in white we have air.

to **iteration 4** to proceed in the next sections, since the simulations will not take a long time to execute, around 5 min, but should still yield **results correct within 0.4% of error**.

Iteration	Mesh accuracy	Time factor	Fr sampling	Abs. residual	Rel. residual	Time [hh:mm:ss]
1	1	50	100	-	-	00:00:14
2	1	100	200	$3.77 \cdot 10^{-2}$	$2.23 \cdot 10^{-2}$	00:00:46
3	2	150	300	$8.20 \cdot 10^{-2}$	$5.10 \cdot 10^{-2}$	00:03:11
4	**2**	**200**	**400**	$\mathbf{6.58 \cdot 10^{-3}}$	$\mathbf{4.07 \cdot 10^{-3}}$	**00:04:21**
5	2	250	500	$1.56 \cdot 10^{-4}$	$9.65 \cdot 10^{-5}$	00:09:38
6	3	300	600	$2.95 \cdot 10^{-3}$	$1.83 \cdot 10^{-3}$	00:34:40
7	3	350	700	$3.03 \cdot 10^{-5}$	$1.88 \cdot 10^{-5}$	00:41:35

Table 4.3.: Purcell Factor convergence scheme results for the hexagonal photonic crystal slab. We vary the simulation parameters to see the convergence of the residual for the Purcell factor. We **highlight** the iteration that gives converged enough results in useful computation time.

The next step in the convergence procedure is to calculate the emission into the radiation modes Γ' using the box method. We determine the right dimensions of the ***hat-like* box** that surrounds the photonic crystal slab in Figure 4.15. Varying the dimensions (h, L, w) of this box we converge the spectra of Γ', as summarized in Table 4.4. We conclude that within 7 iterations **we can converge the results up to around** 0.5% **of error**.

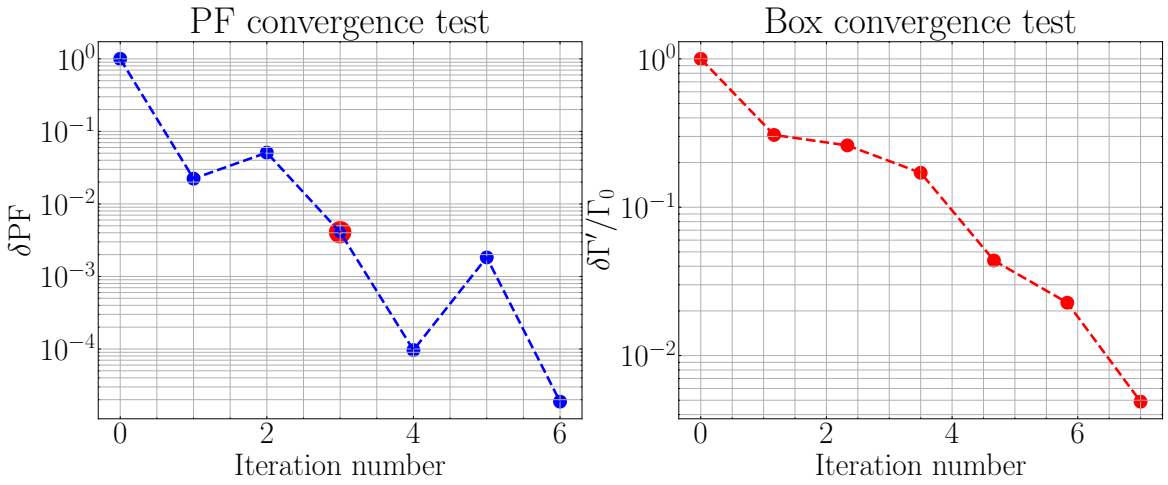

Figure 4.14.: Results for convergence test for the hexagonal photonic crystal slab. On the left, relative residual δPF as a function of iteration for the PF convergence test. On the right, relative residual $\delta\Gamma'/\Gamma_0$ obtained with the box method.

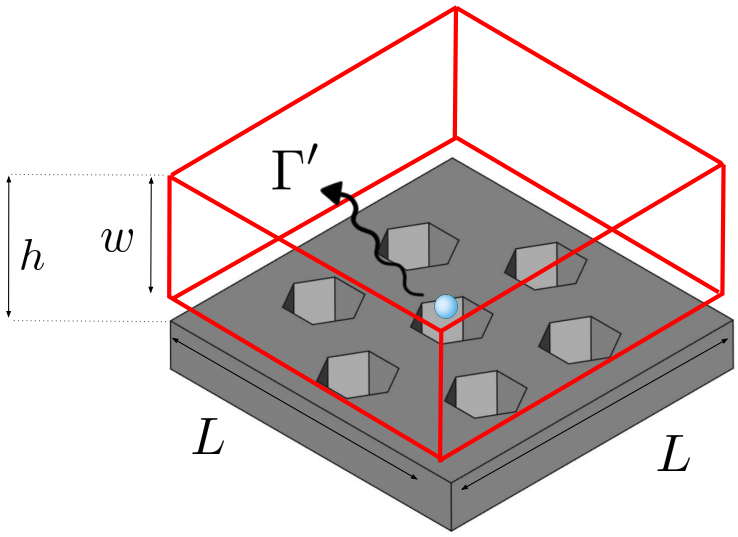

Figure 4.15.: Numerical approach to measure the emission into radiation modes Γ' for the hexagonal lattice slab structure with an atom (in blue). Results are converged increasing the size of the dimensions (h, w, L).

Iteration	Length [a units]	Height [a units]	Width [a units]	Abs. residual	Rel. residual
1	2	0.2	0.1	-	-
2	4	0.4	0.2	$1.37 \cdot 10^{-1}$	$3.01 \cdot 10^{-1}$
3	8	0.6	0.4	$1.57 \cdot 10^{-1}$	$2.61 \cdot 10^{-1}$
4	11	1	0.5	$1.02 \cdot 10^{-1}$	$1.70 \cdot 10^{-1}$
5	12	1.5	0.6	$2.57 \cdot 10^{-2}$	$4.37 \cdot 10^{-2}$
6	13	1.75	0.8	$1.37 \cdot 10^{-2}$	$2.27 \cdot 10^{-2}$
7	13.5	2	1	$2.95 \cdot 10^{-3}$	$4.89 \cdot 10^{-3}$

Table 4.4.: Box method convergence scheme results. We vary the size of the box in Figure 4.14 to see the stability of the results for calculating Γ'.

4.3.3 Dispersive interactions in the band-gap

Using the converged FDTD simulation parameters we calculate the PF in Figure 4.16 for the three dipole orientations, which agrees with the results found in [12]. As expected the atom couples to the TE bands when it is in-plane polarized and to the TM polarized when it is Z polarized. Likewise, for in-plane polarization which corresponds to the Green function components G_{xx} and G_{yy}, we obtain the same results due to the rotational symmetry of the hexagonal structure[17].

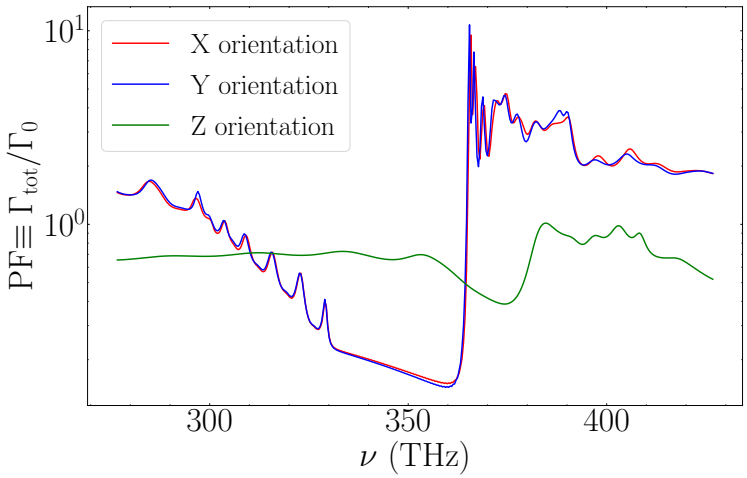

Figure 4.16.: PF spectrum for the hexagonal lattice photonic crystal slab for the three possible cartesian dipole orientations.

[17] This is not entirely true in our results, but should be true in the infinite structure limit. In Figure 4.13 we showed the finite structure with different amount of unit-cells in the X and Y directions, and that is why we see that the blue and red curve in Figure 4.16 don't exactly lie on top of each other.

For the Z orientation of the dipole the PF does not vary too much, but for the in-plane polarization we see a strong coupling to the air band after around 370 THz. Interestingly, we also perceive the effect of the **TE band-gap**, which results in the suppression of emission of around 8dB of spontaneous emission, similar to what is observed in [12]. Once more, as a consequence of the the finite boundaries of the structure we spot narrow resonances in the spectrum that get narrower close to the band-edge.

With the converged boxed dimensions calculated in Table 4.2 we compute the converged spectra for the normalized emission into the radiation modes in Figure 4.17a. We observe that for in-plane polarization of the dipole the radiation modes are **suppressed in the band-gap** but increase once the frequency crosses to the TE dielectric band. Once again, we see the modulation by the band-edge resonances, which become extremely narrow close to the band-edge. We use this spectra to compute the single-atom dissipative quantum cooperativity Γ_{2D}/Γ' spectra for the different dipole orientations. As expected, in the band-gap regime Γ' will become dominant and Γ_{2D} will be negligible, while at both bands next to the band-gap we can achieve a dissipative cooperativity on the order of 10.

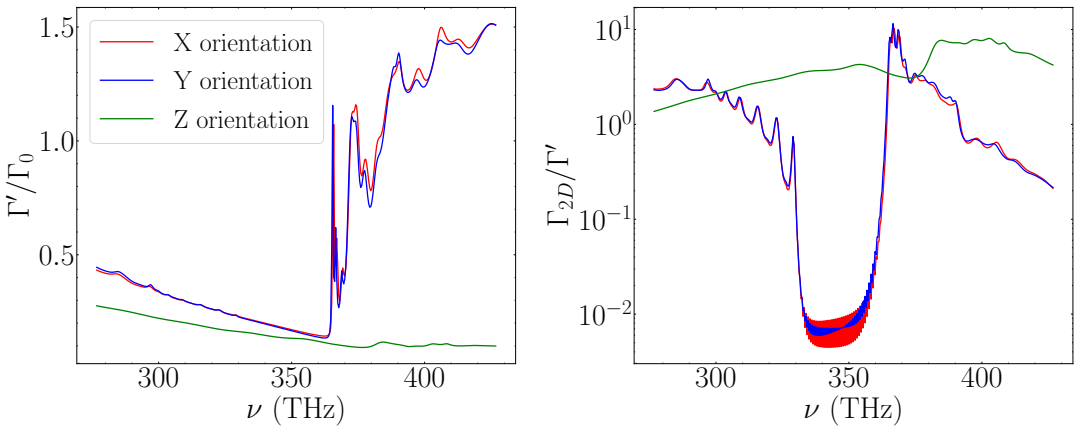

(a) Emission into radiation modes.

(b) Single atom cooperativity.

Figure 4.17.: Spectra of the the FOMs calculated after convergence of the box method for the hexagonal photonic crystal slab. In **(a)** we show the spectra for different dipole orientations of the power flowing through the box faces. In **(b)** we calculate the single-atom cooperativity spectra using the results in **(a)**.

The strong suppression of emission in the band-gap allows us to work with evanescent fields of light while also expecting fairly ($\leq 0.5\Gamma_0$) low emission into the radiation modes. Remember that in the band-gap the modes will be

evanescent waves emitted by the atom that decay exponentially as distance grows far from the emitter. As we saw in Figure 3.8 and in Equation 3.66 and Equation 3.67 it is possible to use these fields to harness **coherent interactions** between atoms. Following Appendix A and taking into account the hyperfine energy transitions with Zeeman splitting we may calculate the spin-exchange rate between Cs atoms as:

$$J_{ijqq'} = \frac{\mu_0 \omega_{qq'}^2}{\hbar} \left| \langle F || \hat{\mathbf{d}} || F' \rangle \right|^2 \hat{\mathbf{e}}_q \cdot \mathrm{Re}\{\mathbf{G}(\mathbf{r}_i, \mathbf{r}_j, \omega_{qq'})\} \cdot \hat{\mathbf{e}}_{q'}^* \,, \tag{4.3}$$

where q, q' correspond to the Δm_F for the back and forth transition between the energy levels, i, j correspond to atom position indices, F, F' correspond to the hyperfine numbers, $\hat{\mathbf{d}}$ is the dipole operator and $\hat{\mathbf{e}}$ corresponds to the polarization of light. In our case, we mainly will work with the $|F = 4, m_f = 4\rangle$ to $|F = 5, m_f = 5\rangle$ transition that, as explained in Appendix A, can act as a **closed transition for σ^+ polarized light, and thus as a two-level system**. In Figure 4.18 we evaluate the real part of the Green's function for the circularly polarized transition. There is, as expected, an evanescent field modulated by the supermodes of the finite photonic crystal structure with circular rotation symmetry, similar to what is found in [12].

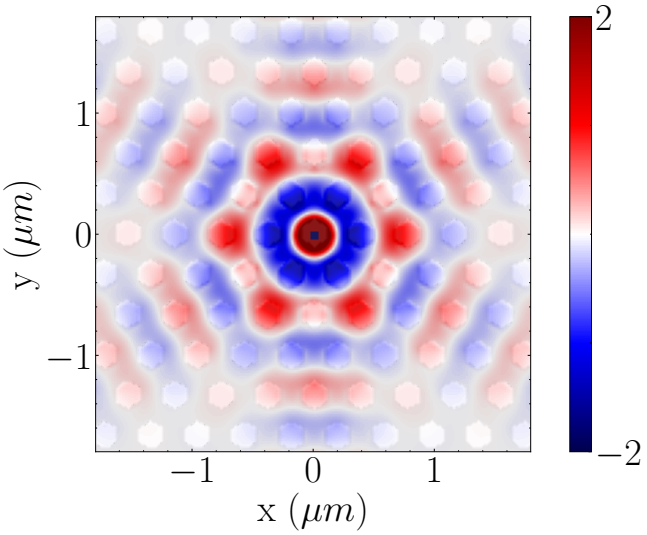

Figure 4.18.: Real part of the Green's function in the band-gap regime at the Cs D_2 line. The colorscale has been saturated to avoid the divergence of the real part of the Green's function at the atom position.

With these coherent spin-exchange interactions it is possible to generate Hamiltonians of the form:

$$\hat{H}_I = \sum_{i,j} = J_{i,j} \sigma_{pq}^i \sigma_{qp}^j \,, \tag{4.4}$$

where $\sigma^i_{pq} = |g_p\rangle^i \langle q|^i$ and g_p and q are the ground and excited states respectively. As suggested in [12] **the geometrical pattern of the spin-exchange rate can be used to engineer the form of the interaction Hamiltonian**. As is currently being done in the LAQS experiment it is possible to use optical tweezers to address individual atoms and arrange them in superlattices, where one can get the desired interaction Hamiltonian[18].

This interaction Hamiltonian may then be chosen to map a given physical problem and by studying its dynamics and measuring its quantum states one can achieve a **quantum simulation platform** [57]. Note that it is also possible to build quantum simulator platforms using tunable and long-range interactions. This is possible, for instance, using the dissipative interactions available in this crystal or in the square photonic crystal slab at the edge of the Brillouin zone. For more information on quantum simulators based on these interactions refer to [58] [59].

4.3.4 Tolerances and tuning rates

Similar to the circular photonic crystal slab we have also calculated the effect of having slanted sidewalls in the hexagonal photonic crystal structure, based on the SEM image in Figure 4.10. Once more, we see a general downward shift of the frequency for the bands when the slopes are added. Therefore, in Figure 4.19 we compute the absolute value of the frequency shift of the dielectric band at the K point for a sweep of the slope angle and we try a linear and a custom fit. The linear fit does not seem to fit the data well but it may prove of use as a first order approximation for the underlying scaling laws. We find the coefficients: $A = 0.4$ THz/° and $B = 1.82$ THz. For a better fit, we try a custom power law fit $\Delta\nu = A\,\alpha^B$. We find that this function fits the data much better with the fitted coefficients $A = 1.62$ THz and $B = 0.57$.

Another experimental constraint that we have addressed in this platform is that there will always be some uncertainty on the atom position even when trapped with optical tweezers [29]. In consequence, we shall test the **effect that displacing the atom from the center of the hole** has on the spontaneous emission rate.

[18] For more information on this please refer to [12].

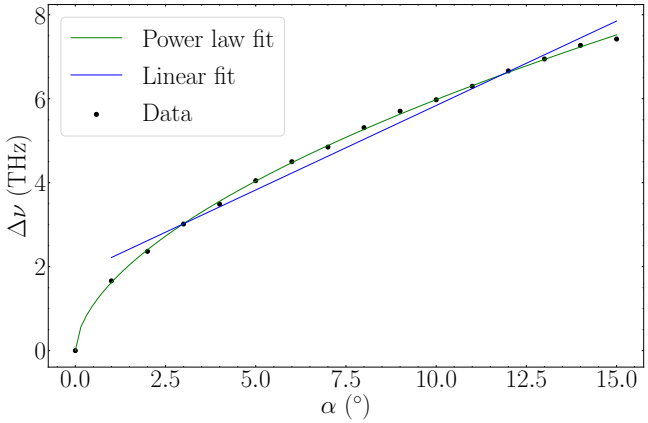

Figure 4.19.: Scaling of the absolute value of the frequency shift of the dielectric TE band as a function of the slope of the hexagonal hole sidewalls. On top of the data we add a linear and a power law fit.

In Figure 4.20 We have moved the atom in the three cartesian directions by 100 nm steps and studied the effect on the PF. In general and as expected, the band-edges are not shifted in frequency but the displacement of the atom from the position of maximum of the guided mode fields weakens the coupling. Interestingly, when we move it 200 nm in the X direction we will no longer be inside the hole, resulting in weaker coupling to the TM mode and higher coupling to the TE mode. Anyhow, since this just gives us an overall qualitative understanding, we have used this data points to calculate the **tuning rates of the coupling**. In the case of coherent atom-atom interactions we will assess how the atom displacement shifts the global minimum of the Purcell factor[19]. With a linear fit[20] of the three data points we find that the results in Table 4.5. Note that we expect similar results for the tuning of the maxima.

	Δ PF$_{\text{min},\Delta x}$	Δ PF$_{\text{min},\Delta y}$	Δ PF$_{\text{min},\Delta z}$
X orientation	0.09	0.12	0.33
Y orientation	0.22	0.11	0.38
Z orientation	0.03	0.03	0.24

Table 4.5.: Tuning rates of the minimum global value of the PF when the atom is displaced in either o the cartesian directions. The units of the tuning rates are $\Gamma_0/100$ nm.

[19] For a more complete assessment one should do more simulations for a broader range of distances and and study how the spin-exchange coefficient J_{ij} varies with atom displacement.

[20] We have not included the last data point in the case of the Δx displacement for the X orientated dipole, since it is we have the previously mentioned unexpected stronger suppression.

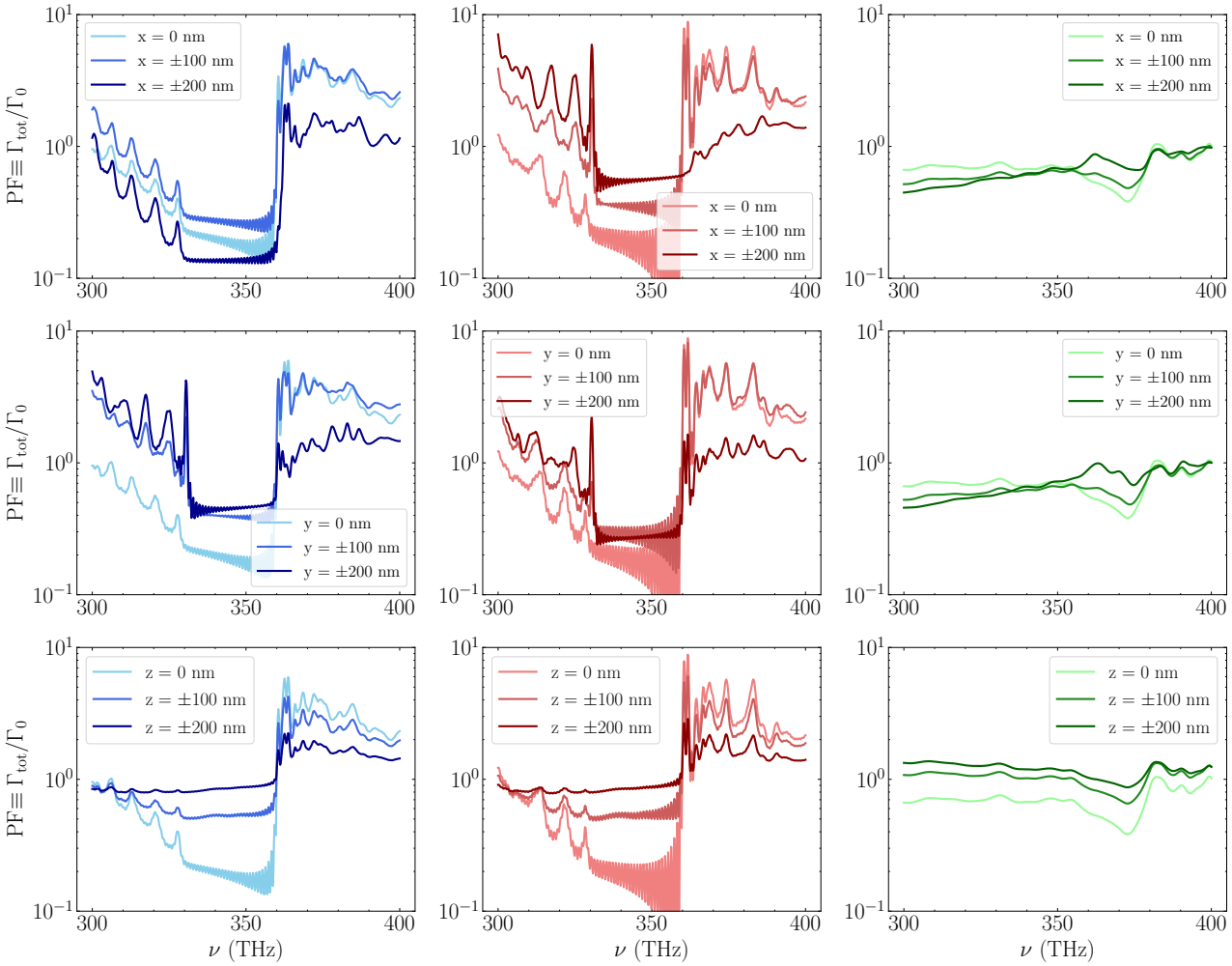

Figure 4.20.: Change in the Purcell factor spectrum when the atoms are displaced inside of the unit cell for three different distances: 0 nm, ±100 nm and ±200 nm. The very narrow resonances are due to low time simulation and hence numerical uncertainty.

4.4 Different atoms, new possibilities

Now that we are able to calculate the FOMs for an arbitrary photonic crystal slab structure with the methods presented in the previous sections we want to extend this formalism to other frequency ranges to see if this may lead to improved results. We will focus on studying the hexagonal photonic crystal structure and the coherent interaction regime in the band-gap.

Changing frequency ranges means that we have to change the transition frequency of the atoms. In our case, we have decided to try out a small sample size of atoms that have already been used in experimental setups, where

proper trapping and cooling is possible, and therefore it should be possible to integrate them[21] to the LAQS platform. The list of atoms we will try is: **Rb, He*, Sr and the aforestudied Cs**. In the case of Rubidium we will work with ^{85}Rb an its D_2 line[22] at 780.24 nm [60], in the case of metastable Helium *He we choose the $2\,^3S_1 \rightarrow 2\,^3P_2$ transition at 1083 nm [61] and for Strontium we choose ^{87}Sr and the $5\,^3P_2 \rightarrow 4\,^1D_2$ transition at 1.8 μm [62][23].

4.4.1 Maximizing the bang-gap width

As a starting point, we will try to numerically **maximize the band-gap** of the structures. Using the workflow defined in Figure 4.21 this involves modifying three parameters: the lattice constant a, the radius of the hexagon's circumscribed circle R (see Figure 2.4.1) and the thickness of the slab t. We try to maximize the band-gap of the structures because we expect this should confine the fields more tightly and results in fewer losses to the radiation modes, so we expect higher J_{ij}/Γ' dispersive quantum cooperativity.

To maximize the band-gap of the structures we use MEEPs MPB frequency-domain solver [55]. First we calculate the frequencies for the dielectric and air TE bands at all k points at the edge of the Brillouin zone. Then, we compute size of the band-gap Δ by subtracting the minimum of the lower band to the maximum of the higher band, and we maximize that quantity. In other words, we minimize a cost function:

$$f(t,a,R) = -\left[\min\{\omega_2(t,a,R)\} - \max\{\omega_1(t,a,R)\}\right] = -\Delta\,, \tag{4.5}$$

where $\omega_1(t,a,R)$ and $\omega_2(t,a,R)$ correspond to the the dielectric and air band respectively. We then use the `scipy.optimize.minimize` [63] minimizer library and the Nelder-Mead [64] algorithm to find the parameters that yield the maximum band-gap.

Once we have maximized the band-gap size we can use the fact that Maxwell's equations are **scale-invariant to align the relevant transition frequency**

[21] With more or less technical efforts.

[22] Corresponding to the transition $5S_{1/2} \rightarrow 5P_{3/2}$. This is similar to the D_2 line in Cs as explained in Appendix A.

[23] In this reference they use ^{88}Sr but isotope shifts from mass effects will be on the order of GHz so we will not take them into account.

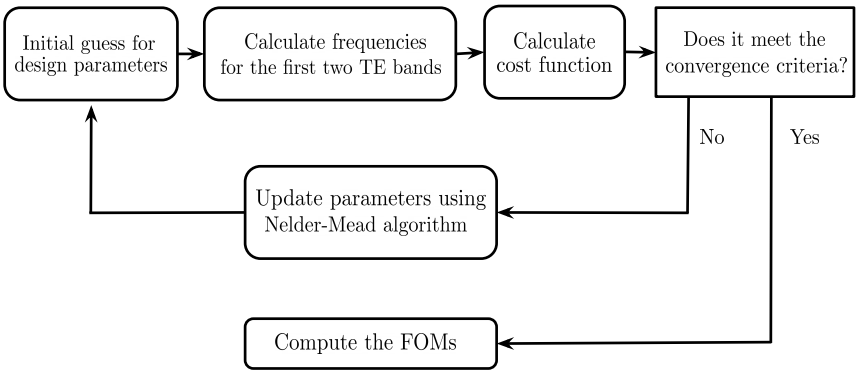

Figure 4.21.: Flow chart for the the optimization scheme. Using the relevant cost function we follow this procedure for each of the different atoms to retrieve the optimized parameters and then calculate the FOMs.

$\omega_{\text{trans.}}$ **to the mid gap frequency** $(\max\{\omega_1\} + \min\{\omega_2\})/2$, allowing for the highest confinement possible. This gives us a photonic crystal design for each of the atoms where we can now compute the FOMs, which are summarized in Table 4.6. We see that in general, aligning the transition frequency up with the midgap frequency does not yield the expected extra suppression of the radiation modes. In fact, due to the larger thickness of the membrane and thin film effects the atoms couple more with the radiation modes. In that sense, in neighboring holes we find lower values for J/Γ' than in our reference simulation. If we think about it this makes sense because we obtain a more confined field close to the atom, which also results in an unforeseen lower spin-exchange coupling to neighboring unit-cells. We also noted the values for the dissipation rate couplings, but in this case they are also lower than the reference.

4.4.2 Fixing the slab thickness

Now, we go a step further by taking into account some **fabrication constraints**. As a matter of fact, it is not possible to fabricate a photonic crystal slab with arbitrary dimensions in the cleanroom. For instance, the thickness is limited by the internal stresses, as too thick a layer will shatter. It is possible to make the membrane thinner, but this may be undesirable because the modes propagating through the structure will become more evanescent and may see surface roughness more. It is safest to stay in the range (200 ± 50) nm, where

Atom	Ref. Caesium [Cs]	Opt. Caesium [Cs]	Rubidium [Rb]	Met. Helium [He^*]	Strontium [Sr]
ν **[THz]**	351.73	351.73	384.23	276.82	166.50
t **[nm]**	200.00	530.11	485.27	673.56	1119.50
a **[nm]**	405.00	403.73	369.58	512.98	852.60
R **[nm]**	138.56	151.17	138.38	192.07	319.24
Δ **[THz]**	28.26	63.58	69.45	50.03	30.10
PF_{max}	10.73	8.69	6.29	5.32	4.87
PF_{min}	0.15	0.37	0.34	0.35	0.37
$\Gamma'_{min}[\Gamma_0]$	0.14	0.28	0.26	0.26	0.25
$\Gamma'(\nu)[\Gamma_0]$	0.16	0.42	0.32	0.32	0.32
$\Gamma_{2D,\,max}[\Gamma']$	12.17	5.82	3.25	5.52	9.67
$J_{2D}(\mathbf{r}_1,\nu)[\Gamma_{tot}]$	-1.23	-0.56	-0.55	-0.49	-0.25
$J_{2D}(\mathbf{r}_2,\nu)[\Gamma_{tot}]$	0.98	0.21	0.20	0.28	0.12
$J_{2D}(\mathbf{r}_3,\nu)[\Gamma_{tot}]$	-0.30	-0.06	-0.05	-0.08	-0.04

Table 4.6.: FOMs for a freely optimized hexagonal photonic crystal slab where the design parameters (t, a, R) have been chosen to have a maximal band-gap Δ while aligning the relevant transition frequency ν to the midgap frequency. Note that $\mathbf{r}_i$, for $i = 1, 2, 3$ refers to the position of the i^{th} nearest neighbor.

there is also low Fabry-Perot reflectivity. That is why in the next section we will work with a **fixed membrane thickness**[24] of 200 nm.

Since we fix the membrane thickness it is no longer possible to conformally modify the design parameters to maximize the band-gap anymore. Therefore, we use the thickness constraint and adjust the other two parameters to fix the transition frequency of the atom at the midgap frequency. For this we create a cost-function $f(t, a, R)$ that will be minimized:

$$f(t,a,R) = \begin{cases} \left|\omega_{\text{trans.}} - \dfrac{\min\{\omega_2\} - \max\{\omega_1\}}{2}\right| & \text{if} \quad \min\{\omega_2\} - \max\{\omega_1\} > 0, \\ \Omega & \text{else} \end{cases} \tag{4.6}$$

where Ω corresponds to a penalty term. We have fixed this penalty at an arbitrary unit 10, that exceeded the values of the function by an order of magnitude, so that the minimizer is able to see that we just want a solution that has a positive band-gap size. Once more we make use of `scipy.optimize.minimize` [63] minimizer library and the Nelder-Mead [64] algorithm to calculate the geometrical parameters that set the transition frequency at the midgap fre-

[24] There are other fabrications constraint that we will take into account in the simulation. For instance, the aspect-ratio (the ratio between a hole's depth and its diameter) must not be extreme. Although the e-beam writer can go down to 10 nm hole sizes, we will limit the hole radius at 50 nm, so that etching process remains manageable.

Atom	Ref. Caesium [Cs]	Opt. Caesium [Cs]	Rubidium [Rb]	Met. Helium [He^*]	Strontium [Sr]
ν **[THz]**	351.73	351.73	384.23	276.82	166.55
t **[nm]**	200.00	200.00	200.00	200.00	200.00
a **[nm]**	405	383.65	353.51	488.20	941.55
R **[nm]**	103.56	115.62	113.88	120.30	271.80
$\mathrm{PF}_{\mathrm{max}}$	10.73	12.49	14.94	6.42	5.77
$\mathrm{PF}_{\mathrm{min}}$	0.15	0.17	0.15	0.19	0.30
$\Gamma'_{\mathrm{min}}[\Gamma_0]$	0.14	0.16	0.14	0.12	0.30
$\Gamma'(\nu)[\Gamma_0]$	0.16	0.19	0.18	0.23	0.31
$\Gamma_{\mathrm{2D,\,max}}[\Gamma']$	12.17	26.04	28.81	33.97	13.37
$J_{\mathrm{2D}}(\mathbf{r}_1,\nu)[\Gamma_{\mathrm{tot}}]$	-1.23	-1.24	-0.55	-1.60	-0.62
$J_{\mathrm{2D}}(\mathbf{r}_2,\nu)[\Gamma_{\mathrm{tot}}]$	0.98	0.97	0.20	1.84	0.77
$J_{\mathrm{2D}}(\mathbf{r}_3,\nu)[\Gamma_{\mathrm{tot}}]$	-0.30	-0.29	-0.05	0.70	-0.32

Table 4.7.: FOMs for an hexagonal photonic crystal slab under thickness constraint, where we optimize to position the transition frequency at the midgap frequency of the photonic crystal. Note that $\mathbf{r}_i$, for $i = 1, 2, 3$ refers to the position of the i^{th} nearest neighbor.

quency. These results are gathered in Table 4.7[25] alongside the FOMs derived from the standard calculation, as we did when we optimized for the maximum band-gap.

From Table 4.7 we can learn several promising results. First of all, we learn that several FOMs may be improved by using different atoms. For instance, in general, even though not aligned with the transition frequency, the maximum value of the dissipative quantum cooperativity $\Gamma_{\mathrm{2D}}/\Gamma'$ is up-to almost three times higher with the optimized Cs, Rb and He^* atoms. As shown in Figure 4.4.2 this happens because the emission into the radiation modes experiences some local minima that align with band-edge resonances at the dielectric air band. It is also worth noting that even if in general the dispersive quantum cooperativity J_{2D}/Γ' is lower than for the reference Cs platform, we find that for the second nearest neighbor we can improve its value by 30% for the He^* atom. Specially promising is the fact that although the FOMs are slightly lower for the Sr atom, since we would be working with much bigger spatial dimensions this could in principle facilitate the fabrication process. There might exist the possibility to purchase this crystals from a company[26] which would result in very few fabrication imperfections.

[25] Since Sr has a smaller frequency we have run the simulations using a pulse of 50 THz bandwidth, which allows us to capture the results of the band-gap and the band-edges.
[26] For example, this could be the MEMS technology company NORCADA [65].

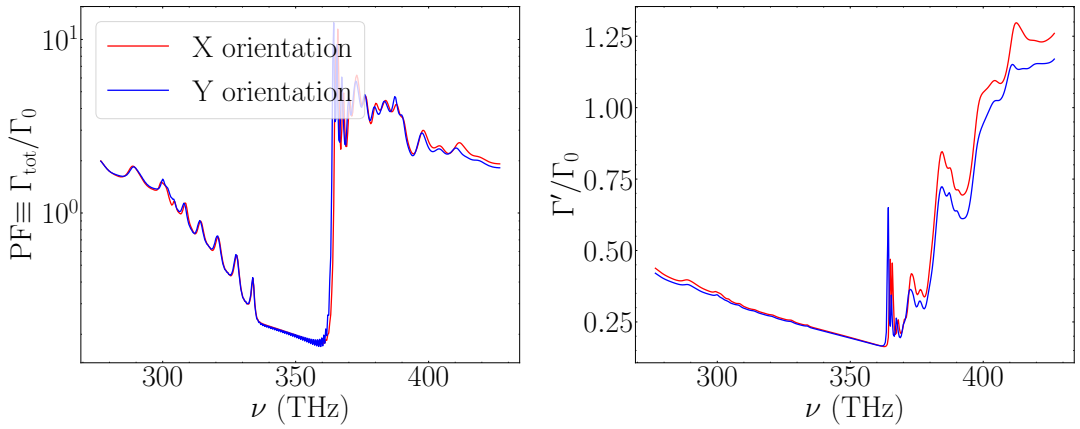

(a) Purcell Factor.

(b) Emission into radiation modes.

Figure 4.22.: Spectra of the FOMs for the optimized structure for Cs. **(a)** PF spectra for different dipole orientations. **(b)** Emission into radiation modes using the converged box method.

As we have seen in Figure 4.22b the change of dimensions has allowed some local minima from the radiation modes that had a higher value in Figure 4.17a which have resulted in an increase of the FOMs. It has been suggested in [32] that certain designs of the dielectric environment may lead to Fabry-Perot resonances and local polarization effects that could counteract the emission into radiative modes. If we find such phenomena it may lead to much better results than those in Table 4.7.

4.5 Back to Caesium: Improving the current design

From the learnings in the previous section we want to go back to more realistic objectives that line up with the current experimental timeline. That being the case, we will try to improve even further the design of the photonic crystal for the Cs atom. Accordingly, we will try to scan the design parameters space and see where we can expect the best results for the dissipative quantum-cooperativity, while being aligned to the Cs D_2 transition.

In Figure 4.5[27] we try a range of lattice constants and hole factors (the ratio of the hole radius to the lattice constant), and show the corresponding PF, dissipative cooperativity and detuning from the D_2 line.

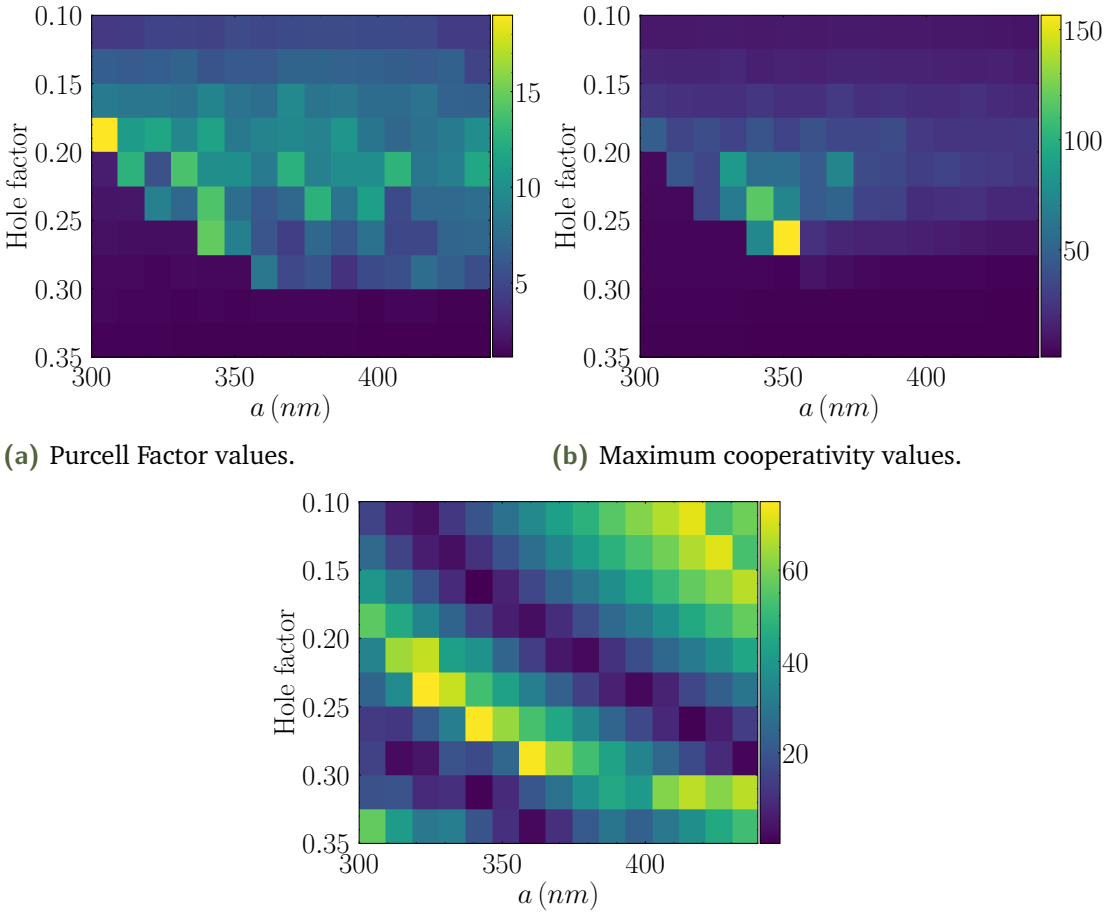

(a) Purcell Factor values.

(b) Maximum cooperativity values.

(c) Absolute value of detuning (THz).

Figure 4.23.: Parameter sweep for the Cs design optimization. We calculate the main FOMs (PF, C and absolute value of the detuning from the D_2 line) for a range of values of the hole factor and the lattice constant a.

Although it is possible to obtain a cooperativity as high as 150, this maximum cooperativity peak is more than 60 THz away from the D_2 line, at 415 THz. Ideally, we would need an atom with a transition frequency at 415 THz to achieve such a high cooperativity and study the tuning of this frequency with a slight variation of refractive index and thickness. Another possibility would be, forgetting our constraint of the membrane thickness, to use the design parameters from Figure 4.5 and conformally vary them together with the thickness to align this maximum to the D_2 line.

[27] Note that in this plot there are many cells that show almost null PF and cooperativity. This happens because our broadband source had a bandwidth of 150 THz, and for certain designs the maxima go so high in frequency and we do not measure them anymore.

In the range of our fabrication constraint it is possible to improve the cooperativity found in Table 4.7 by taking $a = 342.86$ nm and a hole radius $R = 61.58$ nm to find $C = 26$ at 351.53 THz, 0.2 THz away from the D_2 line. Therefore, by using these design parameters we can expect to **double the dissipative quantum cooperativity found with the design in [12]**, similar to what we found in the preceding section, although now aligned with the transition frequency.

Interestingly, if we search for the detuning from D_2 line for Rb[28] we find that we can achieve $C = 45$ at 384.24 THz, 0.01 THz away from the transition frequency, with $a = 364.29$ nm and $R = 100$ nm. With this configuration we can expect to **enhance the dissipative cooperativity up to almost 4 times compared to the reference in [12]**.

Last but not least, there are other ways to increase the single atom spin-exchange and dissipation cooperativities. In fact, it is possible to create a local defect in the photonic crystal structure, which can act as an effective cavity. This cavity may then be engineered as in [66] to suppress further the emission rate into the radiation modes and therefore enhance the spin-exchange cooperativity for the atom. This cavity could also be engineered to enhance the emission into propagating modes in the structure while suppressing the emission into radiation modes, to enhance the dissipative cooperativity. One could then imagine a series of defects in the photonic crystal structure connected by optical channels[29]. This, however limits the flexibility of using photonic crystal structures holistically, and therefore in our optimization approach we have avoided optimizing local defects and have tried to optimize the whole photonic crystal structure.

[28] Using the same transition frequency as in Table 4.6 and Table 4.7.
[29] One may even create superlattices of defects inside the photonic crystal structure to work with a subsystem of atoms with different emission properties.

5 Conclusion and outlook

" Nothing behind me, everything ahead of me, as is ever so on the road."

— Jack Kerouac, *On the road.*

Nanophotonic devices offer rich possibilities to modify the propagation of light at sub-wavelength length scales. In this thesis we have learnt how the properties of novel nanophotonic devices, such as photonic crystal waveguides, may be designed to engineer atom-photon and atom-atom interactions. First, we have discovered what the key ingredients for strong atom-light coupling are, and how we can take advantage of them to design photonic crystal structures. Next, we have studied how atoms couple to each other through the modes of the nanostructures and how it is possible to engineer their coupling coefficients by modifying the dielectric environment.

Most of all, with this work we have **demonstrated a general numerical approach to calculate the main FOMs in strong atom-atom interactions mediated by photons**. Using this framework, which is **available online [31]**, it is now possible to evaluate the performance of different device designs by using FOMs such as the quantum cooperativity, which takes into account the strength of the interaction relative to the losses of the system into the radiation modes. It is now also possible to use this framework to engineer interaction Hamiltonians between several atoms by calculating the coupling coefficients introduced in the Green's function formalism. This will be then used in the future to find nanophotonic designs that match a custom Hamiltonian[1], so that its dynamics can be studied by running a quantum simulation experiment.

The simulation framework may also be used to **optimize the design of the photonic crystal waveguides and achieve stronger interactions while minimizing the loss mechanisms**. In the last sections of Chapter 4 we have

[1] This Hamiltonian will mapped onto a a Hamiltonian from the life-sciences.

studied the FOMs for different frequency regimes and different design parameters. The results suggest possible improvements to the designs that if verified by experimental work, would yield a two-fold improvement on the dissipative quantum cooperativity Γ_{2D}/Γ' in comparison to current-state of the art designs [12]. In order to find the best design possible one ought to expand the parameter search in Section 4.5 to achieve a higher cooperativity while being close to the Cs D_2 line. An alternative in an ideal scenario would be to, either find an atomic transition that matches the highest cooperativity peak, or if one had a perfect fabrication process, to directly use the optimized parameters and conformally vary them using the scale invariance of Maxwell's equations. In the future, it would be even possible to take the design optimization one step further by inverse designing the unit cells of the photonic crystal with state-of-the-art techniques, such as the Topology Optimization framework [56]. Although the results for the very high cooperativity peaks are promising, further numerical studies would be necessary to study the tuning rates and tolerances for these novel designs.

As mentioned previously, there exists the possibility to enhance the quantum cooperativities by finding a **physical mechanism that suppresses the emission into radiation modes**. Perhaps, one could use the TMM to find a frequency range for which the in-plane modes have high transmittance[2] but there is high reflection in the out-of plane direction, which would mean that all the light would stay inside the crystal. Using the TMM one would model the in-plane directions using a finite 1D photonic crystal and the out-of plane direction as as a Fabry-Perot film. Actually, if there was no thickness constraint one may effectively eliminate most of the emission into the radiation modes by studying the reflection of a Fabry-Perot film as a function of the membrane thickness[3]. Finally, one should try to obtain the design parameters for an omnidirectional mirror[4] in the out-of-plane direction [32], to make sure that all the field stays in the photonic crystal slab.

It is likewise important to talk about the **limitations** of this thesis. First and foremost, and as hinted in Appendix C simulations are still simulations, and although they can be used to grasp many physical processes our approach still

[2] Or null transmittance if we want to work with dispersive interaction in the band-gap.
[3] In this case one would take the dielectric constant of the film as a variable, which would come from the ratio of air-dielectric in the structure, and therefore determined by the hole radius: $n_{\text{eff}} = (L_{\text{hole}}/L_{\text{total}})n_{\text{air}} + (L_{\text{Si}_3\text{Ni}_4}/L_{\text{total}})n_{\text{Si}_3\text{Ni}_4}$, where $L_{\text{total}} = L_{\text{hole}} + L_{\text{Si}_3\text{Ni}_4}$.
[4] A mirror for every possible incidence angle at the interfaces.

ignores the inherent quantum nature of atoms, not to mention most of the fabrication imperfection. It was also not easy to construct a sensible numerical framework to extract all the FOMs from our system of interest. In fact, we had many difficulties setting up a coherent convergence scheme to be sure that the calculation of the emission into the radiation modes would be correct. One could improve this procedure by having an alternative way of calculating Γ' and comparing it to the box-method results, as is done in [52]. For instance, this could be done by computing the Green's function for the guided modes $\mathbf{G}_{1D}$[5] and subtracting it to the one calculated using our FDTD method. Then, we would just obtain $\mathbf{G}' = \mathbf{G} - \mathbf{G}_{1D}$ and we would use Equation 3.25 to calculate the decay rate into the radiation modes.

Lastly, the completion of this MSc. thesis opens up many **different research questions that require further exploration**. Novel designs may be useful to improve on atom-trapping close to nanostructures, by using the guided fields of the structures and the Casimir-Polder forces, as suggested in [48]. To get a guided field into the photonic structure one should also design couplers to efficiently couple outside light into the structure. On another note, specially relevant for our σ^+ polarized atomic transition[6] is the prospect of exploring the possibilities of chiral emission in the nanophotonic waveguides, as explained in [12], so that it is possible to engineer light polarization dependent emission. Finally, since the ultimate goal is to address quantum simulation problems, as introduced previously, it will be necessary to engineer the coupling coefficients for each atom so that we are able to construct a desired Hamiltonian. In this sense, the numerical studies carried out in this thesis should prove very useful for future experiments in LAQS and to continue theoretical research in many exciting fronts.

[5] This could be done using a frequency-domain solver and calculating the eigenmodes of the infinite structure. Then one just needs to extend this periodically to the finite structure.
[6] See Appendix A.

Bibliography

1. Chang, D. E., Douglas, J. S., González-Tudela, A., Hung, C.-L. & Kimble, H. J. Colloquium: Quantum matter built from nanoscopic lattices of atoms and photons. *Rev. Mod. Phys.* **90,** 031002 (3 Aug. 2018).
2. Kimble, H. J. The quantum internet. *Nature* **453,** 1023–1030 (June 2008).
3. Gerry, C. & Knight, P. *Introductory Quantum Optics* (Cambridge University Press, 2004).
4. Van Enk, S. J. & Kimble, H. J. Strongly focused light beams interacting with single atoms in free space. *Phys. Rev. A* **63,** 023809 (2 Jan. 2001).
5. Haroche, S. & Raimond, J. *Exploring the quantum: Atoms, cavities and photons* (Oxford University Press, Oxford, 2006).
6. Reiserer, A. & Rempe, G. Cavity-based quantum networks with single atoms and optical photons. *Rev. Mod. Phys.* **87,** 1379–1418 (4 Dec. 2015).
7. Hammerer, K., Sørensen, A. S. & Polzik, E. S. Quantum interface between light and atomic ensembles. *Rev. Mod. Phys.* **82,** 1041–1093 (2 Apr. 2010).
8. Dicke, R. H. Coherence in Spontaneous Radiation Processes. *Phys. Rev.* **93,** 99–110 (1 Jan. 1954).
9. Pritchard, J. D., Maxwell, D., Gauguet, A., Weatherill, K. J., Jones, M. P. A. & Adams, C. S. Cooperative Atom-Light Interaction in a Blockaded Rydberg Ensemble. *Phys. Rev. Lett.* **105,** 193603 (19 Nov. 2010).
10. Dudin, Y. O. & Kuzmich, A. Strongly Interacting Rydberg Excitations of a Cold Atomic Gas. *Science* **336,** 887–889. eprint: https://www.science.org/doi/pdf/10.1126/science.1217901 (2012).

11. Peyronel, T., Firstenberg, O., Liang, Q.-Y., Hofferberth, S., Gorshkov, A., Pohl, T., Lukin, M. & Vuletic, V. Quantum nonlinear optics with single photons enabled by strongly interacting atoms. *Nature* **488,** 57–60 (July 2012).

12. Yu, S.-P., Muniz, J. A., Hung, C.-L. & Kimble, H. J. Two-dimensional photonic crystals for engineering atom–light interactions. *Proceedings of the National Academy of Sciences* **116,** 12743–12751. eprint: https://www.pnas.org/content/116/26/12743.full.pdf (2019).

13. Hood, J. D., Goban, A., Asenjo-Garcia, A., Lu, M., Yu, S.-P., Chang, D. E. & Kimble, H. J. Atom–atom interactions around the band edge of a photonic crystal waveguide. *Proceedings of the National Academy of Sciences* **113,** 10507–10512 (2016).

14. Furusawa, A., Sørensen, J. L., Braunstein, S. L., Fuchs, C. A., Kimble, H. J. & Polzik, E. S. Unconditional Quantum Teleportation. *Science* **282,** 706–709. eprint: https://www.science.org/doi/pdf/10.1126/science.282.5389.706 (1998).

15. Gisin, N. & Thew, R. Quantum communication. *Nature Photonics* **1,** 165–171 (Mar. 2007).

16. Northup, T. E. & Blatt, R. Quantum information transfer using photons. *Nature Photonics* **8,** 356–363 (Apr. 2014).

17. Thompson, J. D., Tiecke, T. G., de Leon, N. P., Feist, J., Akimov, A. V., Gullans, M., Zibrov, A. S., Vuletić, V. & Lukin, M. D. Coupling a Single Trapped Atom to a Nanoscale Optical Cavity. *Science* **340,** 1202–1205. eprint: https://www.science.org/doi/pdf/10.1126/science.1237125 (2013).

18. Dawkins, S. T., Mitsch, R., Reitz, D., Vetsch, E. & Rauschenbeutel, A. Dispersive Optical Interface Based on Nanofiber-Trapped Atoms. *Phys. Rev. Lett.* **107,** 243601 (24 Dec. 2011).

19. Goban, A., Choi, K. S., Alton, D. J., Ding, D., Lacroûte, C., Pototschnig, M., Thiele, T., Stern, N. P. & Kimble, H. J. Demonstration of a State-Insensitive, Compensated Nanofiber Trap. *Phys. Rev. Lett.* **109,** 033603 (3 July 2012).

20. Sorensen, H. L., Polzik, E. S. & Appel, J. Heater Self-Calibration Technique for Shape Prediction of Fiber Tapers. *Journal of Lightwave Technology* **32,** 1886–1891 (May 2014).

21. Appel, J., Windpassinger, P. J., Oblak, D., Hoff, U. B., Kjærgaard, N. & Polzik, E. S. Mesoscopic atomic entanglement for precision measurements beyond the standard quantum limit. *Proceedings of the National Academy of Sciences* **106,** 10960–10965. eprint: https://www.pnas.org/doi/pdf/10.1073/pnas.0901550106 (2009).

22. Christensen, S., Béguin, J.-B., Sørensen, H., Bookjans, E., Oblak, D., Müller, J., Appel, J. & Polzik, E. Toward quantum state tomography of a single polariton state of an atomic ensemble. *New Journal of Physics* **15** (Jan. 2013).

23. Wasilewski, W., Jensen, K., Krauter, H., Renema, J. J., Balabas, M. V. & Polzik, E. S. Quantum Noise Limited and Entanglement-Assisted Magnetometry. *Phys. Rev. Lett.* **104,** 133601 (13 Mar. 2010).

24. Louchet-Chauvet, A., Appel, J., Renema, J. J., Oblak, D., Kjaergaard, N. & Polzik, E. S. Entanglement-assisted atomic clock beyond the projection noise limit. *New Journal of Physics* **12,** 065032 (June 2010).

25. Béguin, J.-B., Burgers, A. P., Luan, X., Qin, Z., Yu, S. P. & Kimble, H. J. Advanced apparatus for the integration of nanophotonics and cold atoms. *Optica* **7,** 1–2 (Jan. 2020).

26. Béguin, J.-B., Laurat, J., Luan, X., Burgers, A. P., Qin, Z. & Kimble, H. J. Reduced volume and reflection for bright optical tweezers with radial Laguerre–Gauss beams. *Proceedings of the National Academy of Sciences* **117,** 26109–26117. eprint: https://www.pnas.org/doi/pdf/10.1073/pnas.2014017117 (2020).

27. Luan, X., Béguin, J.-B., Burgers, A. P., Qin, Z., Yu, S.-P. & Kimble, H. J. *The integration of photonic crystal waveguides with atom arrays in optical tweezers* 2020.

28. Béguin, J.-B., Qin, Z., Luan, X. & Kimble, H. J. Coupling of light and mechanics in a photonic crystal waveguide. *Proceedings of the National Academy of Sciences* **117,** 29422–29430. eprint: https://www.pnas.org/doi/pdf/10.1073/pnas.2014851117 (2020).

29. Ashkin, A. Optical trapping and manipulation of neutral particles using lasers. *Proceedings of the National Academy of Sciences* **94,** 4853–4860. eprint: https://www.pnas.org/doi/pdf/10.1073/pnas.94.10.4853 (1997).

30. Quantum for Life: https://quantumforlife.ku.dk/ (2022).

31. Martinez de Aguirre, B. *Dispersion engineering of atom-photonic crystal waveguide interfaces.* https://github.com/bmdaj/Dispersion_engineering_of_atom-photonic_crystal_waveguide_interfaces. (2022).

32. Joannopoulos, J. D., Johnson, S. G., Winn, J. N. & Meade, R. D. *Photonic Crystals: Molding the Flow of Light (Second Edition)* (Princeton University Press, 2008).

33. Markoö, P. & Soukoulis, C. M. *Wave Propagation: From Electrons to Photonic Crystals and Left-Handed Materials* (Princeton University Press, 2008).

34. Jackson, J. D. *Classical electrodynamics* 3rd ed. (Wiley, New York, NY, 1999).

35. Kittel, C. *Introduction to Solid State Physics* 8th ed. (Wiley, 2004).

36. Rayleigh, L. On the Propagation of Waves through a Stratified Medium, with Special Reference to the Question of Reflection. *Proceedings of the Royal Society of London. Series A, Containing Papers of a Mathematical and Physical Character* **86,** 207–226 (1912).

37. Luan, X. *Towards atom assembly on nanophotonic structures with optical tweezers.* PhD thesis (California Institute of Technology, 2017).

38. Hood, J. *Atom-light interactions in a photonic crystal waveguide.* PhD thesis (California Institute of Technology, 2016).

39. Chang, D. E., Jiang, L., Gorshkov, A. V. & Kimble, H. J. Cavity QED with atomic mirrors. *New Journal of Physics* **14,** 063003 (June 2012).

40. Chang, D. E., Sørensen, A. S., Demler, E. A. & Lukin, M. D. A single-photon transistor using nanoscale surface plasmons. *Nature Physics* **3,** 807–812 (Aug. 2007).

41. Novotny, L. & Hecht, B. *Principles of Nano-Optics* 2nd ed. (Cambridge University Press, 2012).

42. Gruner, T. & Welsch, D.-G. *Quantum optical input–output relations for dispersive and lossy multi-slab dielectric plates* (1995).

43. Sakoda, K. & Ohtaka, K. Optical response of three-dimensional photonic lattices: Solutions of inhomogeneous Maxwell's equations and their applications. *Phys. Rev. B* **54,** 5732–5741 (8 Aug. 1996).

44. Tai, C. *Dyadic Green Functions in Electromagnetic Theory.* (IEEE Series on Electromagnetic Waves, 1994).

45. Barton, G. *Elements of Green's Functions and Propagation.* (Clarendon Press, 1989).

46. Asenjo-Garcia, A., Hood, J. D., Chang, D. E. & Kimble, H. J. Atom-light interactions in quasi-one-dimensional nanostructures: A Green's-function perspective. *Phys. Rev. A* **95,** 033818 (3 Mar. 2017).

47. Reiserer, A. & Rempe, G. Cavity-based quantum networks with single atoms and optical photons. *Reviews of Modern Physics* **87,** 1379–1418 (Dec. 2015).

48. Hung, C.-L., Meenehan, S. M., Chang, D. E., Painter, O. & Kimble, H. J. Trapped atoms in one-dimensional photonic crystals. *New Journal of Physics* **15,** 083026 (Aug. 2013).

49. Wilson, D. J., Regal, C. A., Papp, S. B. & Kimble, H. J. Cavity Optomechanics with Stoichiometric SiN Films. *Physical Review Letters* **103** (Nov. 2009).

50. Barclay, P. E., Srinivasan, K., Painter, O., Lev, B. & Mabuchi, H. Integration of fiber-coupled high-Q SiNx microdisks with atom chips. *Applied Physics Letters* **89,** 131108 (Sept. 2006).

51. Ye, J., Kimble, H. J. & Katori, H. Quantum State Engineering and Precision Metrology Using State-Insensitive Light Traps. *Science* **320,** 1734–1738 (June 2008).

52. Javadi, A., Mahmoodian, S., Söllner, I. & Lodahl, P. Numerical modeling of the coupling efficiency of single quantum emitters in photonic-crystal waveguides. *J. Opt. Soc. Am. B* **35,** 514–522 (Mar. 2018).

53. Witzens, J., Loncar, M. & Scherer, A. Self-collimation in planar photonic crystals. *IEEE Journal of Selected Topics in Quantum Electronics* **8,** 1246–1257 (2002).

54. Muniz, J. A. *Nanoscopic atomic lattices with light-mediated interactions.* PhD thesis (California Institute of Technology, 2017).

55. Oskooi, A. F., Roundy, D., Ibanescu, M., Bermel, P., Joannopoulos, J. & Johnson, S. G. Meep: A flexible free-software package for electromagnetic simulations by the FDTD method. *Computer Physics Communications* **181,** 687–702 (2010).

56. Sigmund, O. & Hougaard, K. Geometric Properties of Optimal Photonic Crystals. *Phys. Rev. Lett.* **100,** 153904 (15 Apr. 2008).

57. González-Tudela, A., Hung, C.-L., Chang, D. E., Cirac, J. I. & Kimble, H. J. Subwavelength vacuum lattices and atom–atom interactions in two-dimensional photonic crystals. *Nature Photonics* **9,** 320–325 (Apr. 2015).

58. Hung, C.-L., González-Tudela, A., Cirac, J. I. & Kimble, H. J. Quantum spin dynamics with pairwise-tunable, long-range interactions. *Proceedings of the National Academy of Sciences* **113,** E4946–E4955. eprint: https://www.pnas.org/doi/pdf/10.1073/pnas.1603777113 (2016).

59. Douglas, J. S., Habibian, H., Hung, C.-L., Gorshkov, A. V., Kimble, H. J. & Chang, D. E. Quantum many-body models with cold atoms coupled to photonic crystals. *Nature Photonics* **9,** 326–331 (Apr. 2015).

60. Steck, D. A. *Rubidium 85 D Line Data*. https://steck.us/alkalidata/rubidium85numbers.pdf. Accessed: 2022-05-03.

61. Pan, T., Chen, T., Sun, D., Han, Y., Xue, X., Zhao, R. & Lan, J. Metastable helium Faraday filter for helium lidar to measure the density of the thermosphere. *Opt. Express* **29,** 4431–4441 (Feb. 2021).

62. Traverso, A., Chakraborty, R., Escobar, Y., Mickelson, P., Nagel, S., Yan, M. & Killian, T. Inelastic and elastic collision rates for triplet states of ultracold strontium. *Physical Review A* **79,** 060702 (June 2009).

63. Virtanen, P., Gommers, R., Oliphant, T. E., *et al.* SciPy 1.0: Fundamental Algorithms for Scientific Computing in Python. *Nature Methods* **17,** 261–272 (2020).

64. Nelder, J. A. & Mead, R. A Simplex Method for Function Minimization. *Comput. J.* **7,** 308–313 (1965).

65. NORCADA. *MEMS and photonic products*. https://www.norcada.com/. Accessed: 2022-05-07.

66. Yu, S.-P. *Nano-Photonic Platform for Atom-Light Interaction*. PhD thesis (California Institute of Technology, 2017).

67. Roca, I. *Experimental implementation of a Top Hat beam shaper*. MSc thesis (University of Copenhagen, 2022).

68. Dideriksen, K. B. *A room-temperature single-photon source in built-in memory*. PhD thesis (University of Copenhagen, 2021).

69. Steck, D. A. *Cesium D line data*. https://steck.us/alkalidata/cesiumnumbers.1.6.pdf. Accessed: 2022-05-02.

70. Foot, C. J. *Atomic Physics* 1st ed. (Oxford University Press Inc., New York, 2005).

71. Happer, W. Optical Pumping. *Rev. Mod. Phys.* **44,** 169–249 (2 Apr. 1972).

72. Buhmann, S. & Welsch, D. Dispersion forces in macroscopic quantum electrodynamics. *Progress in Quantum Electronics* **31,** 51–130 (2007).

73. Huttner, B. & Barnett, S. Quantization of the electromagnetic field in dielectrics. *Physical Review A* **46,** 4306–4322 (Nov. 1992).

74. Casimir, H. B. G. On the Attraction Between Two Perfectly Conducting Plates. *Indag. Math.* **10,** 261–263 (1948).

75. Gonzalez-Tudela, A., Rodríguez, F. J., Quiroga, L. & Tejedor, C. Dissipative dynamics of a solid-state qubit coupled to surface plasmons: From non-Markov to Markov regimes. *Physical Review B* **82** (Sept. 2010).

76. Van Loo, A. F., Fedorov, A., Lalumiè re, K., Sanders, B. C., Blais, A. & Wallraff, A. Photon-Mediated Interactions Between Distant Artificial Atoms. *Science* **342,** 1494–1496 (Dec. 2013).

77. Lumerical Inc.®. *Lumerical FDTD Reference Manual.* (2022).

78. Taflove, A. & Hagness, S. C. *Computational electrodynamics: the finite-difference time-domain method* 3rd ed. (Artech House, Norwood, 2005).

79. Johnson, S., Oskooi, A. & Taflove, A. *Advances in FDTD Computational Electrodynamics: Photonics and Nanotechnology* (Artech House, 2013).

80. Ashcroft, N. W. & Mermin, N. D. *Solid State Physics* (Holt-Saunders, 1976).

81. Conway, J., Burgiel, H. & Goodman-Strauss, C. *The Symmetries of Things* (Taylor & Francis, 2008).

A Real atoms

" When it comes to atoms, language can be used only as in poetry. The poet, too, is not nearly so concerned with describing facts as with creating images."

— Niels Bohr

In all previous theoretical and computational considerations we have idealized our atoms as being a classical monochromatic dipole point source. This is an acceptable first approximation when the wavelength of the source is much bigger than the radius of the atom; however, atoms in the real world are more complex than our simplified two-level system. In this appendix we study this in the case of our atom of interest: ^{133}**Cs**. Not only do we work with Cs atoms because they have been used in QUANTOP throughout the years [18] [19] [20] [21] [22] [23] [24] and there is excellent experience and documentation available, but also because the atoms have a **simple electronic configuration** ([Xe]6s^1) and a **heavy mass**, which facilitates laser cooling and trapping experiments.

A.1 Electronic structure of the Caesium atom

Alkali metals are defined by their electronic configuration, with one valence electron on their most outer s orbital. In particular, the electronic configuration of a caesium atom is [Xe]6s^1. Taking this into account we can calculate the **fine structure** of caesium from the coupling between the orbital angular momentum **L** of the valence electron and its spin angular momentum **S**. This yields a total angular momentum quantum number $\mathbf{J} = \mathbf{L} \oplus \mathbf{S}$, which can take values $|L - S| \leq J \leq L + S$. For instance, for the ground state of Cs

we have $L = 0$ and $S = 1/2$, so $J = 1/2$ and for the excited state we have $L = 1$ and $S = 1/2$, so $J = 1/2$ or $J = 3/2$. These levels are related to the $6P_{1/2}$ and $6P_{3/2}$ states. The transitions from ground state correspond to the lines D_1 ($6S_{1/2} \rightarrow 6P_{1/2}$), with $\lambda \simeq 852.357$ nm or $\nu \simeq 351.726$ THz, and D_2 ($6S_{1/2} \rightarrow 6P_{3/2}$), with $\lambda \simeq 894.593$ nm or $\nu \simeq 335.116$ THz.

One can go one step further by calculating the **hyperfine structure** of Cs. This structure arises from the coupling between **J** and the total nuclear angular momentum **I**. Similarly as before, we have $\mathbf{F} = \mathbf{J} \oplus \mathbf{I}$ and $|J - I| \leq F \leq J + I$. For instance, for the ground state of caesium we have $J = 1/2$ and $I = 7/2$, so $F = 3$ or $F = 4$. Applying the same principle for the D_1 line, $F = 3, 4$ and for the D_2 line $F = 2, 3, 4, 5$.

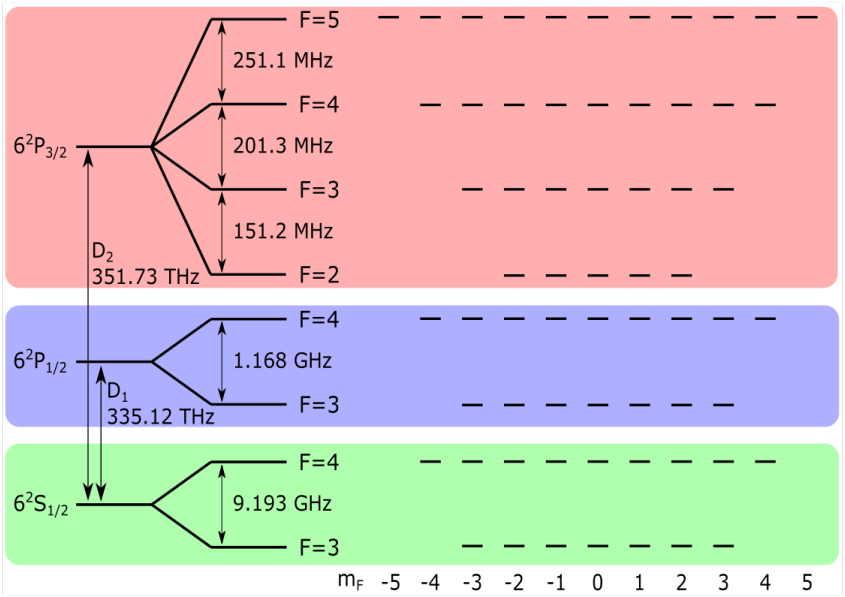

Figure A.1.: Hyperfine electronic structure of Cs for the experimentally interesting D1 and D2 lines. Next to the lines we see the effect of the hyperfine splitting. Note that energy levels are not at scale. Figure courtesy of Isaac Roca and adapted from [67] [68].

Additionally, if there is an external field the hyperfine levels can split into sublevels. For example, if there is a DC magnetic field along the Z axis B_z, each of the hyperfine levels splits into $2F + 1$ sublevels $|F, m_F\rangle$. This is known as **Zeeman spliting** and the energy shift is approximately [69]:

$$\Delta E_{|F,m_F\rangle} = \mu_B g_F m_F B_z \,, \tag{A.1}$$

where μ_B is the Bohr magneton, g_F is the hyperfine Landé g factor [69]. This is important in our analysis because this magnetic shifts can happen even without an external magnetic field, as a result of vector light shifts of an optical field. This is known as the **AC Stark shift**.

A.2 Selection rules and effective two-level system

It is important to note that despite the complexity of real atoms the two level system can still be useful in some cases. For instance, when we have lasers with a linewidth narrow enough to address hyperfine levels we can experimentally approximate a two-level system.

For a two-level system we need to have a ground and excited state and be able to transition from one to another. First, we prepare the ground state $J = 1/2,\ F = 4,\ m_F = 4$ by using a **pump laser**. At room temperature atoms are equally distributed in all the Zeeman sublevels for $F = 3$ and $F = 4$. The probe laser will then make transitions happen, obeying the **selection rules**, which are a consequence of the conservation of energy and momentum [70]:

$$\begin{aligned}
\Delta L &= \pm 1\,, \\
\Delta S &= 0\,, \\
\Delta J &= 0, \pm 1\,, \\
\Delta F &= 0, \pm 1\,, \\
\Delta m_F &= 0, \pm 1\,.
\end{aligned}$$

Using these rules, we will use a pump laser with σ^+ polarized light, which has a Δm_F=1 and $\Delta F = 0$, as show in orange in Figure A.2. The state will then decay by spontaneous emission with $\Delta m_F = 0, \pm 1$, so that in the long run we reach the state with $m_F = 4$ because it is not possible to drive it to another state using the pump laser. This is known as **dark state**. Following the selection rules it is still possible that atoms decay to the hyperfine levels with $F = 3$, so we use a **repump laser** to bring the atomic population back to the $F = 4$ state, as shown in red in Figure A.2. Once we have pumped and repumped our atoms, we can use the σ^+ polarized **probe laser** in blue in Figure A.2, to drive

the **closed transition** $J = 1/2, F = 4, m_F = 4 \rightarrow J = 3/2, F = 5, m_F = 5$ [71], which will act as an effective two-level system. Since this closed transition is not perfect and there is possibility of decay to other sublevels, once again the pump and repump laser come in handy to keep the closed transition going.

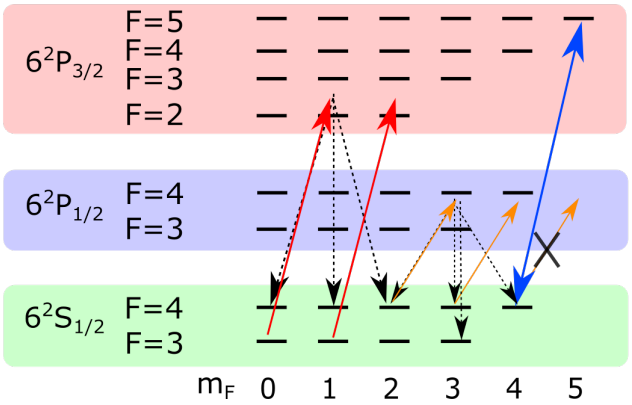

Figure A.2.: Optical pumping and probing scheme. The pump (orange) and the repump lasers (red) bring the atom to the ground state and then we drive the close transition using the probe laser (blue). Figure courtesy of Isaac Roca [67].

A.3 Strength of transitions

As we saw in Chapter 3 the interaction of atoms and light can be written in terms of the dipole moment. Therefore, for the fine and hyperfine structures we can evaluate the transition strength as a function of the dipole moment elements $\langle F m_F | \hat{\mathbf{d}} | F' m'_F \rangle$. Using the **Wigner-Eckart theorem** and expressing the the matrix elements in terms of **Clebsch-Gordan coefficients** one can calculate that [69] [37] [1]:

$$\langle F m_F | \hat{d}_q | F' m'_F \rangle = \langle F || \hat{\mathbf{d}} || F' \rangle C_{m_F, q} \tag{A.2}$$

$$= \langle F || \hat{\mathbf{d}} || F' \rangle (-1)^{F'-1+m_F} \sqrt{2F+1} \begin{pmatrix} F' & 1 & F \\ m'_F & q & -m_F \end{pmatrix}, \tag{A.3}$$

where q refers to the components of $\mathbf{r}$ in the spherical basis: $\hat{\mathbf{e}}_{\pm 1} = \mp \frac{1}{\sqrt{2}}(\hat{x} \pm i\hat{y})$ and $\hat{\mathbf{e}}_0 = \hat{z}$. Then, we can write $\hat{\mathbf{d}} = \sum_q \hat{d}_q \hat{\mathbf{e}}^*_q$. Returning to the aforementioned

[1] The double bar notation in the dipole operator indicate matrix reduction as in [69] and the matrix corresponds to a Wigner 3-j symbol [69].

selection rules, $\hat{\mathbf{e}}_{\pm 1}$ corresponds to $\sigma_{\pm}$ light whereas $\hat{\mathbf{e}}_0$ corresponds to Π polarized light. The reduced matrix element for F can be written as [69]:

$$\langle F||\hat{\mathbf{d}}||F'\rangle = \langle J||\hat{\mathbf{d}}||J'\rangle(-1)^{F'+J+1+I}\sqrt{(2F'+1)(2J+1)}\begin{pmatrix} J & J' & 1 \\ F' & F & 1 \end{pmatrix}, \quad \text{(A.4)}$$

where the matrix represents a Wigner 6-j symbol [69]. Experimentally, it is possible measure the decay in free space of the J' state. For the Cs D1 and D2 line the values have been measured to be [69]:

$$\langle J = 1/2||\hat{\mathbf{d}}||J' = 1/2\rangle = 3.1822 e a_0\,, \quad \text{(A.5)}$$

$$\langle J = 1/2||\hat{\mathbf{d}}||J' = 3/2\rangle = 4.4786 e a_0\,, \quad \text{(A.6)}$$

where then we can use Equation A.3 and Equation A.4 to determine the transition strengths for hyperfine transitions.

A.4 Coupling rates

With the basic understanding on how to calculate the the dipole transitions for the hyperfine structure of Cs it is possible to recalculate the coupling rates in Equation B.20 and Equation B.21 to account hyperfine structure dipole operators as is done in [46] and in [37]. Defining the hyperfine structure Green function matrix element as $g_{ijqq'} = J_{ijqq'} + i\Gamma_{ijqq'}/2$ the spin-exchange and dissipation rates are:

$$J_{ijqq'} = \frac{\mu_0\omega_{qq'}^2}{\hbar}\left|\langle F||\hat{\mathbf{d}}||F'\rangle\right|^2 \hat{\mathbf{e}}_q \cdot \mathrm{Re}\{\mathbf{G}(\mathbf{r}_i, \mathbf{r}_j, \omega_{qq'})\} \cdot \hat{\mathbf{e}}_{q'}^*\,, \quad \text{(A.7)}$$

$$\Gamma_{ijqq'} = \frac{2\mu_0\omega_{qq'}^2}{\hbar}\left|\langle F||\hat{\mathbf{d}}||F'\rangle\right|^2 \hat{\mathbf{e}}_q \cdot \mathrm{Im}\{\mathbf{G}(\mathbf{r}_i, \mathbf{r}_j, \omega_{qq'})\} \cdot \hat{\mathbf{e}}_{q'}^*\,. \quad \text{(A.8)}$$

B Quantum atom-light interactions

" You must take your opponent into a deep dark forest where 2+2=5, and the path leading out is only wide enough for one."

— Mikhail Tal

It is possible to expand the Green's function framework introduced in Chapter 3 to account for fully quantized interactions. In this chapter, we explain how this can be done and how in some limits the results are analogue to the classical case. For a further in depth review with applications to photonic nanostructures please refer to [46].

B.1 QED in dielectric media

It is possible to expand the previous Green's function formalism to a framework where the atom-light interactions are fully quantized. In this picture one can write the Hamiltonian of the system as:

$$\hat{H} = \hat{H}_{\mathrm{F}} + \hat{H}_{\mathrm{A}} + \hat{H}_{\mathrm{int}} \tag{B.1}$$

where $\hat{H}_{\mathrm{F}}$ is the field Hamiltonian, $\hat{H}_{\mathrm{A}}$ is the atom's Hamiltonian and $\hat{H}_{\mathrm{int}}$ is the Hamiltonian that describes the interaction of the field and the atom. Many textbooks, such as [3] cover the description and quantization of this Hamiltonian in free space and describe the **Jaynes-Cummings model of atom-light interaction** [3]. However, things are more complex in the presence of dielectric media since losses affect the commutation relation of operators. We follow the approach by Welsch et al. [72] [42] [38] that use the Green's function for the quantization of the field with dielectric media.

To describe the **field Hamiltonian** we need to understand the field as a set of harmonic oscillators that represent material polarization, as well as a reservoir of oscillators where the system can dissipate energy to. It is shown in [73] that the Hamiltonian can be solved for bosonic operators $\hat{\mathbf{f}}^\dagger(\mathbf{r},\omega)$ and $\hat{\mathbf{f}}(\mathbf{r},\omega)$:

$$\hat{H} = \int \mathrm{d}^3\mathbf{r}^3 \int_0^\infty \mathrm{d}\omega\, \hbar\omega\, \hat{\mathbf{f}}^\dagger(\mathbf{r},\omega)\hat{\mathbf{f}}(\mathbf{r},\omega)\,. \tag{B.2}$$

which obey the commutation relations:

$$[\hat{f}_k(\mathbf{r},\omega), \hat{f}^\dagger_{k'}(\mathbf{r}',\omega')] = \delta_{kk'}\delta(\mathbf{r}-\mathbf{r}')\delta(\omega-\omega')\,, \tag{B.3}$$

$$[\hat{f}_k(\mathbf{r},\omega), \hat{f}_{k'}(\mathbf{r}',\omega')] = 0\,. \tag{B.4}$$

It can also be shown [73] that it is possible relate the bosonic operators to other field variables. In particular, the electric field can be expressed as:

$$\hat{\mathbf{E}}(\mathbf{r},\omega) = i\frac{\omega^2}{c^2}\sqrt{\frac{\hbar}{\pi\varepsilon_0}}\int d\mathbf{r}'^3\sqrt{\varepsilon_I(\mathbf{r}',\omega)}\mathbf{G}(\mathbf{r},\mathbf{r}',\omega)\hat{\mathbf{f}}(\mathbf{r}',\omega) + \mathrm{H.C}\,. \tag{B.5}$$

Interestingly, using the properties of the electric field with the Green's function formalism one can calculate the vacuum fluctuations of the electric field which are related to the imaginary part of the Green's function as:

$$\langle 0|\,\Delta\mathbf{E}(\mathbf{r},\omega)\Delta\mathbf{E}^\dagger(\mathbf{r}',\omega')\,|0\rangle = \frac{\hbar\omega^2}{\pi\varepsilon_0 c^2}\mathrm{Im}\{\mathbf{G}(\mathbf{r},\mathbf{r}',\omega)\}\delta(\omega-\omega')\,, \tag{B.6}$$

which can be obtained by using the Green's function identities as in [72]. These vacuum fluctuations are strictly related with **Casimir-Polder forces** [74] [72] and are specially relevant in our research are; for instance, for trapping atoms close to nanostructures [48].

B.2 Atom-light interactions with Green's functions

As we saw previously, in our system one can treat atoms as dipoles, which in quantum mechanics can be expressed as two-level systems with a ground-state

$|g\rangle$ and an excited state $|e\rangle$, which are separated by an energy shift $\hbar\omega_A$, as introduced in Appendix A. This means the **single atom Hamiltonian** is:

$$\hat{H}_{\mathrm{A}} = \hbar\omega_A \frac{1}{2}\left(|e\rangle\langle e| - |g\rangle\langle g|\right) = \frac{\hbar\omega_A}{2}\hat{\sigma}_Z\,. \tag{B.7}$$

In our nanophotonical structures the atom will interact with the electromagnetic field. The interaction between a dipole and the field can be expressed as [3]:

$$\hat{H}_{\mathrm{int}} = -\hat{\mathbf{E}}(\mathbf{r},t)\cdot\hat{\mathbf{d}}(t)\,, \tag{B.8}$$

where $\hat{\mathbf{d}}(t) = e\hat{\mathbf{r}}(t)$ is the dipole operator of the atom. This dipole operator may be projected into two states using a unitary transformation:

$$\hat{\mathbf{d}}(t) = \left(|g\rangle\langle g| + |e\rangle\langle e|\right)\hat{\mathbf{d}}(t)\left(|g\rangle\langle g| + |e\rangle\langle e|\right) = \mathbf{d}\hat{\sigma}(t) + \mathbf{d}^*\hat{\sigma}^\dagger(t) \tag{B.9}$$

where we have introduced the Pauli spin operators $\sigma = |g\rangle\langle e|$ and $\sigma^\dagger = |g\rangle\langle e|$, and the dipole matrix elements $\mathbf{d} = \langle g|\,\hat{\mathbf{d}}\,|e\rangle$ and $\mathbf{d}^* = \langle e|\,\hat{\mathbf{d}}\,|g\rangle$[1].

Using the previously defined Green's function formalism for field quantization, we can incorporate the atom and atom-field interactions to get the total Hamiltonian for N identical atoms:

$$\hat{H} = \int \mathrm{d}^3\mathbf{r}^3 \int_0^\infty \mathrm{d}\omega\,\hbar\omega\,\hat{\mathbf{f}}^\dagger(\mathbf{r},\omega)\hat{\mathbf{f}}(\mathbf{r},\omega) + \sum_{j=1}^{N}\frac{\hbar\omega_A}{2}\hat{\sigma}_Z - \sum_{j=1}^{N}\hat{\mathbf{E}}(\mathbf{r}_j,t)\cdot\left(\mathbf{d}\hat{\sigma}(t) + \mathbf{d}^*\hat{\sigma}^\dagger(t)\right)\,. \tag{B.10}$$

Note that the electric field in this expression can be expressed in terms of the Green's functions and the bosonic operators of the field by using Equation B.6. To understand the time-evolution of different operators in the system we can use **Heisenberg's equation of motion**:

$$\dot{\hat{O}}(t) = \frac{1}{i\hbar}[\hat{O}(t),\hat{H}]\,. \tag{B.11}$$

Using the identity $\hat{\sigma} = 2\sigma^\dagger\hat{\sigma} - 1$ and the following commutation relations for Pauli spin operators:

$$[\hat{\sigma}^\dagger,\hat{\sigma}] = \hat{\sigma}^z \qquad [\hat{\sigma}^z,\hat{\sigma}] = -2\hat{\sigma} \qquad [\hat{\sigma}^z,\hat{\sigma}^\dagger] = 2\hat{\sigma}^\dagger\,, \tag{B.12}$$

[1] Note that due to the odd parity of the dipole operator the rest of matrix elements equal zero: $\langle e|\,\hat{\mathbf{d}}\,|e\rangle = \langle g|\,\hat{\mathbf{d}}\,|g\rangle = 0$.

we can get the time evolution of the Pauli matrices:

$$\dot{\hat{\sigma}}_j = -i\omega_A\hat{\sigma} + \frac{1}{\hbar}\hat{\sigma}_j^z\hat{\mathbf{E}}(\mathbf{r}_j,t)\cdot\mathbf{d}_j \tag{B.13}$$

$$\dot{\hat{\sigma}}_j^z = \frac{2i}{\hbar}\hat{\sigma}^\dagger\hat{\mathbf{E}}(\mathbf{r}_j,t)\cdot\mathbf{d}_j + \text{H.C.} \tag{B.14}$$

It can be proven that solving for the time evolution of the bosonic field operators and using the properties of the Green's functions one can also solve for the time evolution of the electric field operator [38], which gives:

$$\dot{\hat{\mathbf{E}}}(\mathbf{r},\omega,t) = i\omega\hat{\mathbf{E}}(\mathbf{r},\omega,t) + \sum_{j=1}^{N} i\frac{\mu_0\omega^2}{\pi}\text{Im}\{\mathbf{G}(\mathbf{r},\mathbf{r}_j,\omega)\}\cdot\hat{\mathbf{d}}_j(t) \tag{B.15}$$

Equation B.13, Equation B.14 and Equation B.15 form a set of nonlinear coupled equations that can be solved self-consistently. First of all, one needs to solve for the electric field[2] and then substitute it into the above system. It is possible to further simplify our system of coupled differential equations by performing the very well-known **Markov approximation**, where one performs the frequency integral by supposing the time integral only contributes over a small correlation time [75] and supposes that scale of atomic operators is much longer than the correlation length [38]. Applying the approximation gives the expression for the electric field as [37]:

$$\hat{\mathbf{E}}(\mathbf{r},t) = \hat{\mathbf{E}}_0(\mathbf{r},t) + \mu_0\omega_A^2\sum_{j=1}^{N}\mathbf{G}(\mathbf{r},\mathbf{r}_j,\omega_A)\cdot\mathbf{d}_j\hat{\sigma}_j(t)\,. \tag{B.16}$$

If one takes a closer look at this equation, we will see that it has a very similar form to electric field resulting from the emission of a classical dipole in Equation 3.43, but that in this case we are in the time domain.

As was our objective, we can now substitute this expression for the electric field in. Equation B.13 and Equation B.14, to obtain the **time evolution of the atomic operators as a function of the Green's function**:

$$\dot{\sigma}_j = -i\omega_A\hat{\sigma}_k - i\hat{\sigma}_k^Z\sum_{j=1}^{N}\hat{\sigma}_j\frac{\mu_0\omega^2}{\hbar}\mathbf{d}_k^*\mathbf{G}(\mathbf{r}_k,\mathbf{r}_j,\omega_A)\mathbf{d}_j - i\hat{\Omega}_k\hat{\sigma}_k^Z \tag{B.17}$$

$$\dot{\sigma}_k^Z = 2i\frac{\mu_0\omega^2}{\hbar}\sum_j\left[\mathbf{d}_k^*\mathbf{G}(\mathbf{r}_k,\mathbf{r}_j,\omega_A)\mathbf{d}_j\hat{\sigma}_k^\dagger\hat{\sigma}_j - \text{H.C.}\right] + 2i(\hat{\Omega}_k\hat{\sigma}_k^\dagger - \text{H.C.})\,. \tag{B.18}$$

[2]The total electric field $\mathbf{E}(\mathbf{r},t) = \int_0^\infty d\omega\mathbf{E}(\mathbf{r},\omega)$ can be obtained by integrating over the total frequency space.

where we have introduced the electric free-field operator $\hat{\Omega}_k = \mathbf{d}_k \cdot \hat{\mathbf{E}}_0(\mathbf{r}_k, \omega)/\hbar$.

In the low saturation limit[3], where atoms are well approximated by classical dipoles, we can take $\langle \hat{\sigma}_z \rangle \simeq -1$, since most atoms will be in the ground state [37]. Let us define, as we did for the classical case, the complex coupling rate:

$$g_{ij} = J_{ij} + \frac{i}{2}\Gamma_{ij} = \frac{\mu_0 \omega_A^2}{\hbar} \mathbf{d}_i^* \cdot \mathbf{G}(\mathbf{r}_i, \mathbf{r}_j, \omega_A) \cdot \mathbf{d}_j \tag{B.19}$$

and the spin-exchange and dissipation rates as:

$$\Gamma_{ij} = \frac{2\mu_0 \omega_A^2}{\hbar} \mathrm{Im}\{\mathbf{d}_i^* \cdot \mathbf{G}(\mathbf{r}_i, \mathbf{r}_j, \omega_A) \cdot \mathbf{d}_j\} \tag{B.20}$$

$$J_{ij} = \frac{\mu_0 \omega_A^2}{\hbar} \mathrm{Re}\{\mathbf{d}_i^* \cdot \mathbf{G}(\mathbf{r}_i, \mathbf{r}_j, \omega_A) \cdot \mathbf{d}_j\}\,. \tag{B.21}$$

This makes Equation B.17 take the form of the classical system of radiatively coupled dipoles in Equation 3.45. The difference is, however, that in this case we take into account the dipole moment of the atoms[4]. The quantum equivalent in this case is:

$$\dot{\hat{\sigma}}_k = i(\omega_A + J_{kk})\hat{\sigma}_k - \frac{1}{2}\Gamma_{kk}\hat{\sigma}_k + i\sum_{j \neq k} \hat{\sigma}_j \left(J_{kj} + \frac{i}{2}\Gamma_{kj}\right) + i\hat{\Omega}_k \tag{B.22}$$

As we saw in the classical case, for a single atom J_{kk} corresponds to a frequency shift, whereas Γ_{kk} corresponds to the decay rate. When one wants to describe the interactions between two atoms both J_{kj} and Γ_{kj} are needed.

[3] The system of equations can be solved beyond the low saturation limit by using the quantum regression theorem [40] [76].

[4] For a more in-depth analysis of the dipole moments of real atoms and their effect on the Green's function formalism , please refer to Appendix A

C Computational photonics

"... Nature isn't classical, dammit, and if you want to make a simulation of nature, you'd better make it quantum mechanical, and by golly it's a wonderful problem, because it does not look so easy."

— Richard Feynman,
1st *Physics of Computation Conference.*

Throughout this thesis we want to understand the behavior of optical systems that inherently have a quantum nature. It is however, still possible to extract some knowledge about this quantum properties even from classical simulations. Indeed, as we have described in the previous chapters, in most of the cases the FOM one would like to calculate stem from the Green's function, which is the electric field response for a classical dipole point-source. We can therefore gain a deep understanding about our system by solving Maxwell's equations using numerical methods. This is in turn, would allows us to optimize the design of the waveguides, that could be fabricated and manufactured thereafter.

In this section we will introduce two of the main approaches to **solving Maxwell's equations numerically**: frequency-domain simulation and time-domain simulations. The theory behind comes mainly from [32] but also from from what was learnt by using MEEP [55], Lumerical's FDTD solver [77] and all the related documentation.

C.1 Frequency-domain simulations

It is possible to solve Maxwell's equations in different ways, but one of the most fundamental insights that we want to calculate are the eigenvalues and

eigenstates of a periodic system, such as a photonic crystal. This is possible by using a **frequency domain eigensolver**. It involves solving Equation 2.14:

$$\left[(i\mathbf{k}+\nabla)\times\frac{1}{\varepsilon(\mathbf{r})}(i\mathbf{k}+\nabla)\times\right]\mathbf{u}_{\mathbf{k}}(\mathbf{r})=\left(\frac{\omega(\mathbf{k})}{c}\right)^{2}\mathbf{u}_{\mathbf{k}}(\mathbf{r})\,, \tag{C.1}$$

which as we saw previously is an eigenvalue problem. Remember that $\mathbf{u}_k(\mathbf{r})$ are the periodic Bloch states for the magnetic field[1] $\mathbf{H}_{\mathbf{k}}=\mathrm{e}^{\mathrm{i}\mathbf{k}\cdot\mathbf{r}}\mathbf{u}_k(\mathbf{r})$. In addition to this, the eigenstates of the system have to fulfill the transversality condition $(\mathbf{ik}+\nabla)\cdot\mathbf{u}_{\mathbf{k}}=0$. If one calculates the solution of Equation C.1 as a function of $\mathbf{k}$ one can calculate the band structures of periodic systems, as was done in this thesis[2]. This is usually done by discretizing the problem by means of a function expansion[3] which will give us a **generalized eigenproblem** of the form $Ax=\omega^2Bx$ where we want to solve for x and ω and A and B are matrices defined by the discretization.

It is very numerically costly to solve this problem completely using linear-algebra packages and since we usually only need the lowest energy eigenvalues and eigenvectors the go-to approach is using **iterative methods**. An iterative method starts from a random guess for the eigenvector and applies an iterative approach to converge towards the true eigenvector. For instance, one can use the variational theorem to prove that for a eigenproblem of the type $Ax=\omega^2Bx$ the minimum eigenvalue ω_0 is [32]:

$$\omega_0^2=\min_x\left\{\frac{x^\dagger Ax}{x^\dagger Bx}\right\} \tag{C.2}$$

where $x^\dagger$ is the adjoint of the vector x. This is also known as **Rayleigh quotient minimization** [32]. Then, one just uses a numerical minimizer to find the smallest eigenvalue and subsequently calculates the second lowest eigenvalue that is orthogonal to x.

Additionally, it is worth noting that the previous method may also be applied when we study a non-periodic system. For an aperiodic system one needs to apply the **supercell approximation**: with periodic boundary conditions we surround the localized dielectric with a large simulation volume in the

[1] It is unwise to use the electric field formulation in Equation 2.10 for numerical calculations since one has to manually enforce the transversality condition of the field.
[2] In particular, we used the MPB free-source python library [55]
[3] Usually the planewave basis is employed since it automatically ensures the transversality condition is fulfilled.

aperiodic direction so that in the periodic limit the images of the dielectric do not see each other. This is possible because in this limit the fields will be exponentially localized and we do not risk any interference between localized structures.

Apart from calculating the eigenvalues and eigenvectors of a system in the frequency domain one can also calculate the response of a monochromatic source $\mathbf{J}(\mathbf{r})e^{i\omega t}$ in linear media. We can formulate Maxwell's equations as in Eq. 2.10 where now we have to add the contribution for a current source:

$$\left[(\nabla \times \nabla \times) - \left(\frac{\omega}{c}\right)^2 \varepsilon(\mathbf{r})\right] \mathbf{E}(\mathbf{r}) = i\omega\mu_0 \mathbf{J}(\mathbf{r})\,, \tag{C.3}$$

which is a linear equation that can be discretized to form a linear system of equations that take the matrix form $Ax = b$. This method is usually employed for calculations with open boundaries. These open boundaries can be mimicked with **perfectly matched layers (PML)** as boundaries of the simulation volume. These layers act as a perfect absorbing material so that the electromagnetic fields that reach them do not reflect back.

C.2 Finite-difference time-domain method

If we think about replicating electromagnetism experiments in a computer, the approach that comes the closest may be to simulate the full time-dependent Maxwell equations. Time domain solutions can give rise to nonlinear phenomena, in contrast to frequency domain methods, and can also be applied to solve frequency domain problems.

The most widespread method for time-domain simulations is the **finite-difference time domain** method, or **FDTD**. This implies that the fields will be discretized in space and time, so that derivatives may also be approximated numerically. The time-evolution of the field usually relies on the **leap-frog** scheme, where the calculation of the electric and magnetic field are off-set by a time-step Δt:

$$\frac{\partial u(t)_i}{\partial t} = \frac{u(t)_{i+1/2} - u(t)_{i-1/2}}{\Delta t} + \mathcal{O}(\Delta t^2)\,, \tag{C.4}$$

where u_i is a field component at time-index i. The spatial configuration of the fields relies on what is known as the **Yee grid** where the different field

components have different locations on a grid-cell. This cell also relies on a spacing Δx between different field components so that the same scheme of time-derivatives in Equation C.4 may also be applied in the spatial domain. For more information on the Yee grid please refer to [78] and [79].

One of the strong suits of FDTD lies in that it is possible to compute the response of a particular system for many frequencies by a single computation. This is done by taking the Fourier transform of a single short pulse. Since Maxwell's equation are linear it is possible to calculate the frequency response of a field by taking it's Fourier transform. As a matter of fact, many FDTD solvers take advantage of very efficient ways of calculating this transforms, such as the **Fast Fourier Transform (FFT)**. Of course, there are some drawbacks: using Fourier's method means that to resolve a spectrum very precisely requires a long run-time. Additionally, one needs to overcome the transient response of a system by turning on the source smoothly and waiting until the steady-state is reached. Finally, these methods require high temporal resolution for high spatial resolution, so that numerical stability is preserved [32].

C.3 Computational photonics for LAQS

With a general understanding on how the frequency- and time-domain solvers work we shall explain how we have run the simulations in this thesis. We have used the LAKS PC in the LAQS laboratory, which has 64 AMD Ryzen Threadripper 3970X 32-Core Processor CPUs[4] with a mean of 3 GHz of clock-speed. With this configuration we have scripted and run all the code that can be found in this thesis' `Github` [31].

All the band-diagrams and eigenmode profiles in this thesis have been calculated using MEEP's **MPB frequency domain eigensolver** [55]. The usual workflow for setting up these simulations involves defining the unit-cell dimensions, the lattice vectors, the dielectric structure, the k points[5] and the number of bands. One also has to define the mesh resolution, which tells us in how many grid points we discretize the unit-cell of our photonic crystal. Then, we run the simulation and retrieve the frequency for each one of the bands in each

[4] This has allowed us to parallelize our simulation and run on multiple cores, which we have defaulted to 8 cores.

[5] For more information on these please refer to Appendix D.

of the k points and reconstruct the band-diagram. To calculate the fields one just has to use the built-in `get_efield` functions in Meep and call the solver to retrieve the field value in each point of the discretized simulation domain, which is defined by the previously mentioned mesh resolution parameter.

To perform **FDTD simulations** we have used both Meep [55] and Lumerical [77]. We started using Meep to get familiarized with FDTD simulations and then transitioned to Lumerical after finding lower simulation times for similar setups. As an example, I will try to explain the **workflow** of running a photonic crystal slab simulation as is explained in the `phc_example.ipynb` Jupyter Notebook in the `Github` [31]. In this example we have defined the following parameters of the FDTD simulation:

- **Simulation domain**: We define the discretization of the simulation volume as well as the dimensions of it.

  The discretization of the simulation volume is defined by the **mesh accuracy**, which can have a value from 1 to 5. The mesh accuracy setting of 2 which corresponds to 10 mesh points per wavelength[6] is considered reasonable for the FDTD method, and mesh accuracy 4 or 5 which corresponds to 18 or 22 mesh points per wavelength is considered high accuracy [77]. Additionally, we use Lumerical's Conformal-Mesh Technology (CMT) [77] which effectively discretizes the simulation domain and gives better accuracy at the boundaries between simulation objects and reduces simulation time[7].

  Next, we define the time the simulation is going to run for, in units of the time it takes for light in vacuum to cross the simulation volume. We call this **time factor**, as we saw in Chapter 4.

  Finally, we define the boundary conditions that will be applied. In this case, we use PML boundary conditions so that we consider an isolated finite photonic crystal structure, similar to what one should encounter in the lab.

[6] This is true when using the auto non-uniform mesh [77].

[7] We apply the CMT 1 configuration which should only handle materials. Due to the $1/(\Delta x)^4$ dependence of the simulation time on the mesh size, where Δx is the discretization length, results can often be achieved in roughly 1/10 the time [77].

- **Dielectric function**: We define the value of the dielectric function of the photonic crystal for the discretized volumes in the simulation. This involves defining a Si_3N_4 plate with finite thickness and punching holes on it. For reference, please see the structure defined in Figure 4.13, where Si_3N_4 is shown in black and air is shown in white. Note that in our analysis we have modelled the dielectric function of Si_3N_4 as a real constant with $\varepsilon = 2$ and we have not accounted for the dispersion of the material, assuming a frequency independent dielectric function. For a more complete analysis these points should be added to the simulation.

- **Sources**: We add the sources to the simulation.

  To model the atom we use a broadband dipole source with the a frequency span centered at the transition frequency and with a bandwidth according to the spectral results we want to calculate. In our case, for a Cs atom emitting into a photonic crystal slab we may choose a bandwidth of around 150 THz.

  We also specify the **sampling resolution**, as we saw in Chapter 4, which tells us in how many points we evaluate the spectral functions[8].

  Finally, we position this dipole at a particular spatial point in the photonic crystal simulation domain.

- **Monitors**: We set the surfaces where we want to measure fields or record power flux. For instance, in the case of the photonic crystal slab we measure the power and field at the dipole position to calculate the Purcell Factor and we measure the power flowing through the boxes in Fig. 4.15 to determine the radiation power.

- **Running**: We have to run the simulation file with all the previous specifications defined in it.

- **Results**[9]: Once the simulation is finished we can retrieve the FOMs from the monitor information. For instance, the **Purcell Factor** is equivalent to

[8] The sampling resolution should not be confused by the frequency resolution that is determined by the Fourier transform and the time signal of the source.

[9] To calculate the dispersive quantum cooperativity we have to measure the real part of the Green's function in the middle plane of the slab and normalize it to the total emission rate.

dividing the power emitted by a dipole source in the environment by the power emitted by the dipole in a homogeneous environment. This is so because the emission rate is proportional to the Local Density of Optical States (LDOS), and the LDOS is proportional to the power emitted by the source [77]. As a matter of fact, the LDOS can be calculated as [79] [55]:

$$\mathrm{LDOS}_l(\mathbf{r},\omega) = -\frac{2\varepsilon(\mathbf{r})\mathrm{Re}\{\mathbf{E}_l(\mathbf{r},\omega)\mathbf{p}^*(\omega)\}}{\pi|\mathbf{p}(\omega)|^2}\,, \tag{C.5}$$

where l is the dipole orientation, $\mathbf{E}_l(\mathbf{r},\omega)$ is the electric field which is calculated using the Green's function and $\mathbf{p}(\omega)$ is the dipole moment of the source. As we can see the this is proportional to the power radiated by a dipole, as shown in Equation 3.21.

Finally, we calculate the emission into the radiation modes by summing the contributions of all surfaces in Figure 4.15 and normalizing by dividing by the power emitted by the dipole in the homogeneous environment. Then, we can directly calculate the emission into the guided modes $\Gamma_{2D} = \Gamma_{tot} - \Gamma'$. With all this information it becomes straightforward to calculate the dissipative cooperativity: Γ_{2D}/Γ'.

A similar approach can be followed to solve the problem for the one-dimensional waveguide in Chapter 4.

D

More on solid state electromagnetism

" Entzuten duzue? Melodia bat da, aire bat, arnas bat, burdin artetik ihes eta jostari. Sentimendu bat, ahoz aho, ura harri artean bezala iritsi gara, belaunaldiz belaunaldi berri bihurtu den kantu bat gara inoiz eta inork ixildu ez duena."

— Jon Maia, *Kantu bat gara.*

Crystal lattices are one of the main pillars of solid-state physics. These are usually first introduced in undergraduate courses to study the electrical properties of materials. This involves a quantum mechanical description of electrons, which means solving the Schrödinger equation in periodic energy potentials. In our case, we want to do something similar, but instead, we want to solve Maxwell's equations to study the propagation of electromagnetic fields in periodic dielectric structures. Therefore, we can transfer much the knowledge from solid-state physics to our particular problem of photonic crystals. For these explanations we will follow [32] but we will also complement with information from classic solid-state physics textbooks as [80].

D.1 Reciprocal lattice and Brillouin zone

A crystal structure is defined as a structure whose components are arranged periodically. These components may be periodic on a lattice so that the function $f(\mathbf{r})$ that defines a lattice fulfills $f(\mathbf{r}) = f(\mathbf{R} + \mathbf{r})$, where $\mathbf{R}$ are known as the **lattice vectors**.

Let's take the Fourier transform of our function:

$$f(\mathbf{r}) = \int d^3\mathbf{q}\, g(\mathbf{q}) \mathrm{e}^{i\mathbf{q}\cdot\mathbf{r}}\,. \tag{D.1}$$

where $g(\mathbf{q})$ is the coefficient for a plane wave with wave vector $\mathbf{q}$. If we apply the periodicity condition to the Fourier transform we find that $g(\mathbf{q}) = g(\mathbf{q})\,\mathrm{e}^{i\mathbf{q}\cdot\mathbf{R}}$. The only non-trivial solutions to this are those that fulfill $\mathrm{e}^{i\mathbf{q}\cdot\mathbf{R}} = 1$, or equivalently $\mathbf{q}\cdot\mathbf{R} = 2\pi N$, with $N \in \mathbb{Z}$, for all $\mathbf{R}$. The vectors $\mathbf{q}$ that satisfy this relationship are known as **reciprocal lattice vectors** and are denoted with the symbol $\mathbf{G}$. These also form a lattice and the periodic function that defines the lattice may also be expanded in terms of the lattice:

$$f(\mathbf{r}) = \sum_{\mathbf{G}} f_{\mathbf{G}} \mathrm{e}^{i\mathbf{G}\cdot\mathbf{r}}\,. \tag{D.2}$$

Every lattice vector can be written in terms of the **primitive lattice vectors** which are the smallest vectors that connect lattice points between each other. This means that we can write $\mathbf{R} = l\mathbf{a}_1 + m\mathbf{a}_2 + n\mathbf{a}_3$ where $\mathbf{a}_{1,2,3}$ are the primitive lattice vectors. This principle also applies to the reciprocal lattice where we can write $\mathbf{G} = l\mathbf{b}_1 + m\mathbf{b}_2 + n\mathbf{b}_3$ where $\mathbf{b}_{1,2,3}$ are the primitive reciprocal lattice vectors. Taking into account that $\mathbf{G}\cdot\mathbf{R} = 2\pi N$, this means that $\mathbf{a}_i \cdot \mathbf{b}_j = 2\pi\delta_{i,j}$. This allows us to relate the primitive reciprocal lattice vectors to the primitive lattice vectors [35]:

$$\mathbf{b_1} = \frac{2\pi\mathbf{a}_2 \times \mathbf{a}_3}{\mathbf{a}_1 \cdot (\mathbf{a}_2 \times \mathbf{a}_3)}\,, \quad \mathbf{b_2} = \frac{2\pi\mathbf{a}_3 \times \mathbf{a}_1}{\mathbf{a}_1 \cdot (\mathbf{a}_2 \times \mathbf{a}_3)}\,, \quad \mathbf{b_3} = \frac{2\pi\mathbf{a}_1 \times \mathbf{a}_2}{\mathbf{a}_1 \cdot (\mathbf{a}_2 \times \mathbf{a}_3)}\,. \tag{D.3}$$

In Chapter 2 we saw that according that in a photonic crystal lattice the field distribution is modulated by the Bloch state, which is periodic as $\mathbf{u_k}(\mathbf{r}) = \mathbf{u_k}(\mathbf{r}+\mathbf{R})$. Now we have seen that the spatial periodicity means that we also have a reciprocal lattice that is periodical. This means that there will also be a periodicity in k space, as in $\mathbf{u_k}(\mathbf{r}) = \mathbf{u_{k+G}}(\mathbf{r})$. There is therefore a finite zone in the reciprocal lattice that gets repeated over and over again, known as the **Brillouin zone**[1]. It is possible to use the point symmetries in the lattice to further restrict this area, giving the **irreducible Brillouin zone**.

[1] It is possible to geometrically calculate the Brillouin zone by finding the zone that is closer to one lattice point than to its nearest neighbors [32].

D.2 Two-dimensional lattices

The photonic crystals slabs that are fabricated for our experimental setup are based on two lattice structures: the square and hexagonal lattices. Let's see what the lattice vectors and Brillouin zone are for each of them.

We can define the square lattice by using vectors that define a square; for instance: $\mathbf{a}_1 = a\hat{\mathbf{x}}$ and $\mathbf{a}_2 = a\hat{\mathbf{y}}$ as in Figure D.1. If we calculate the reciprocal lattice vectors using Equation D.3 we see that the reciprocal lattice is also a square lattice with lattice vectors $\mathbf{b}_1 = (2\pi/a)\hat{\mathbf{x}}$ and $\mathbf{b}_2 = (2\pi/a)\hat{\mathbf{y}}$. The Brillouin zone can be determined selecting a crystal point in the reciprocal lattice and drawing bisectors to every lattice vector [32]. The section that gets enclosed by these lines close to the crystal point corresponds to the Brillouin zone, marked in orange in Equation D.3.

The square lattice has a symmetry group in IUC notation as p4m [81], which means that due to rotation symmetries we can divide the Brillouin zone in 8 equivalent irreducible Brillouin zones. This is shown in yellow in Figure D.1 together with the 3 critical points at the edge of the irreducible zone: $\Gamma = (0, 0)$, $M = (0.5, 0.5)$ and $X = (0.5, 0.0)$, in lattice vector units.

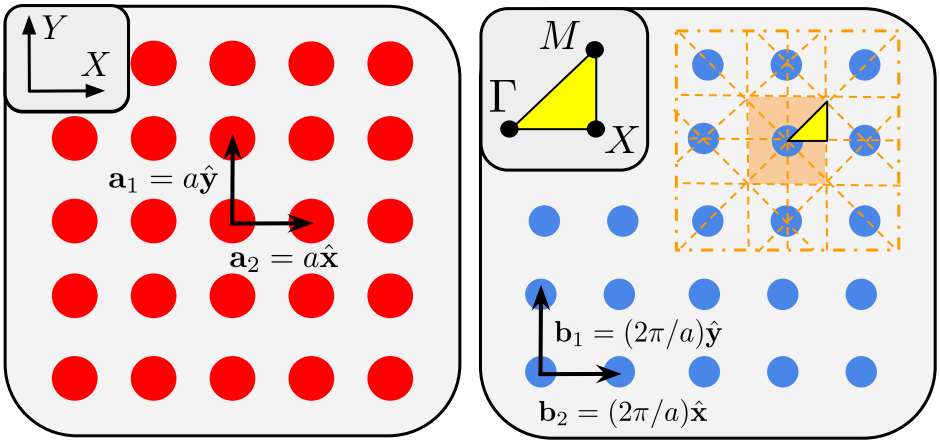

Figure D.1.: Two-dimensional square lattice structure. On the left, real-space lattice structure and on the right the reciprocal lattice structure. In orange the Brillouin zone and in yellow the irreducible Brillouin zone with the most important symmetry points.

Regarding the hexagonal lattice we proceed in similar fashion. The lattice vectors in this case are $\mathbf{a}_1 = a(\hat{\mathbf{x}} + \hat{\mathbf{y}}\sqrt{3})/2$ and $\mathbf{a}_2 = a(\hat{\mathbf{x}} - \hat{\mathbf{y}}\sqrt{3})/2$. Applying Equation D.3 we see that the reciprocal lattice is also an hexagonal lattice where the lattice vectors are rotated $90°$, with $\mathbf{b}_1 = (2\pi/a)(\hat{\mathbf{x}} + \hat{\mathbf{y}}/\sqrt{3})$ and $\mathbf{b}_2 = (2\pi/a)(\hat{\mathbf{x}} - \hat{\mathbf{y}}/\sqrt{3})$. In this case the Brillouin can also be calculated using bisectors, and yields an hexagon, as colored in orange in Figure D.2.

Additionally, the hexagonal lattice has a symmetry group in IUC notation as p6m [81], which means that due to rotation symmetries we can divide the Brillouin zone in 8 equivalent irreducible Brillouin zones. This is shown in yellow in Figure D.2 together with the 3 critical points at the edge of the irreducible zone: $\Gamma = (0, 0)$, $K = (2/3, 1/3)$ and $M = (0.5, 0.5)$, in lattice vector units.

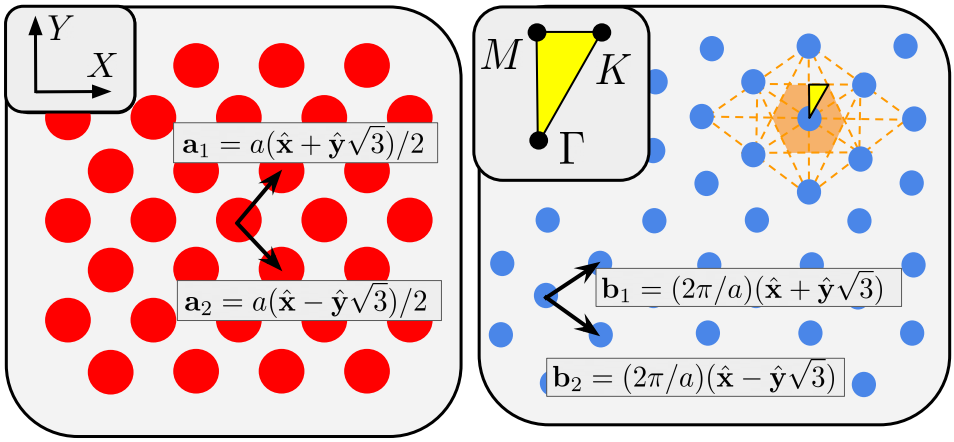

Figure D.2.: Two-dimensional hexagonal lattice structure. On the left, real-space lattice structure and on the right the reciprocal lattice structure. In orange the Brillouin zone and in yellow the irreducible Brillouin zone with the most important symmetry points.